LEIBNIZ-INSTITUT FÜR ATMOSPHÄREN PHYSIK IAP

Habilitationsschrift

am Leibniz-Institut für Atmosphärenphysik in Kühlungsborn

Energetics of turbulent momentum diffusion and gravity wave breakdown in general circulation models of the atmosphere

von

Erich Becker

Abstract: The present study proposes new parameterizations of momentum diffusion, frictional heating (dissipation), and gravity wave-mean flow interaction for global modeling of the atmospheric general circulation. Particular emphasis is spent on the direct thermodynamic effects associated with gravity wave breakdown such as energy deposition and the dissipation of wave kinetic energy. The new formulations are specified in order to meet the following axiomatic constraints: the stress tensor is symmetric; the energy conservation law is fulfilled for arbitrary fluid volumes of the resolved flow; the frictional heating is positive definite; and surface friction does not affect the energy budget of the atmosphere.

The new friction and dissipation forms are tested against the corresponding conventional methods, using an idealized but nevertheless considerably realistic general circulation model for the boreal winter climate. It is found that the neglect of frictional heating, which is common to climate and weather forecast models, leads to an artificial net thermal forcing of about 2 Wm^{-2}. With the new model definition this shortcoming is reduced by two orders of magnitude. Moreover, the long-term global mean of the simulated frictional heating yields approximately 1.9 Wm^{-2}. This value is in agreement with the residuum in the conventional case, as well as with previous estimates of Oort and Lorenz for the net dissipation owing to synoptic and planetary waves.

The well-known analysis of filtering out turbulent motions is extended for gravity waves. This leads to a new perspective of the planetary-scale heat budget of the upper mesosphere/lower thermosphere. It is shown that the dissipation of gravity wave kinetic energy, the local adiabatic conversion of mean enthalpy into gravity wave kinetic energy, and the wave entropy flux cannot be neglected. A corresponding gravity wave parameterization based on Lindzen's saturation theory is proposed which allows to compute these terms in addition to the conventional terms like momentum flux, pressure flux, and diffusion coefficient. An upper bound of 2 is derived for the effective Prandtl number that scales the combined entropy flux owing to turbulence and gravity waves. Corresponding model simulations predict dissipation rates up to 8 Kd^{-1} in summer, once the tropospheric gravity wave source is adjusted to drive a realistic summer-to-winter-pole residual circulation in the upper mesosphere. It is found that the dissipation is overcompensated by the adiabatic conversion term such that the residuum of both cools the upper mesosphere/lower thermosphere.

Postal address:
Schloss-Str. 6
18225 Kühlungsborn
Germany

IAP Kühlungsborn
November 2003
IAP Nr. 07/2003
ISSN 1615-8083

Energetics of turbulent momentum diffusion and gravity wave breakdown in general circulation models of the atmosphere

Habilitationsschrift

zur

Erlangung des akademischen Grades

doctor rerum naturalium habilitatus / habilitata (Dr. rer. nat. habil.)

der Mathematisch-Naturwissenschaftlichen Fakultät

der Universität Rostock

vorgelegt von

Erich Becker, geb. am 7. November 1961 in Marburg

aus Kühlungsborn

Rostock, 15. Januar 2003

Gutachter:

Prof. Dr. Gerhard Schmitz
Leibniz-Institut für Atmosphärenphysik, Kühlungsborn

Prof. Dr. Joseph Egger
Meteorologisches Institut der Universität München

Prof. Dr. Robert Sausen
DLR-Institut für Physik der Atmosphäre, Oberpfaffenhofen

Probevorlesung:

3. November 2003

Contents

Chapter 1

Introduction

The dynamics of large-scale atmospheric flow are inevitably linked to small-scale turbulent motions. The general reason for this linkage is that atmospheric waves transfer kinetic energy to smaller scales. The downscaling of kinetic energy is maintained by the pressure gradient force at large scales and turbulent friction at small scales. However, in numerical models of the atmospheric circulation we cannot simulate all relevant small-scale motions explicitly by application of elementary hydrodynamics. Rather, depending on the available numerical resolution, we have to use more or less approximate model equations where the relevant subscale motions are represented as functions of the resolved flow by some kind of parameterization.

The idea pursued in the present study is that any parameterization of subscale motions should satisfy certain hydrodynamic constraints. Among these, the energy conservation constraint applied to the resolved flow is evidently of particular importance. Strictly speaking, for any given subscale process the energy constraint ultimately determines the thermodynamic effects in terms of the momentum flux tensor and the sensible heat flux. This idea will be applied to two specific problems of dynamic meteorology: first, the role of turbulent frictional heating in the global energy budget of the general circulation of the troposphere and, second, the local heat budget of the upper mesosphere/lower thermosphere (height region between about 70 and 105 km, hereafter MLT). At first sight both problems appear quite distinct. However, the dynamics of the MLT is controlled from below, namely by the breakdown of internal gravity waves (hereafter IGWs) which are generated in the troposphere and lower stratosphere. Furthermore, the breakdown of IGWs is not conceivable without the action of small-scale turbulence (Lindzen, 1981). Therefore, a suitable representation of turbulent friction and frictional heating from the planetary boundary layer up to the mesopause appears worthwhile for global modeling of the atmospheric circulation. To set the basis for the more complicated problem of nonconservative gravity wave propagation, we shall first deal with the representation of

turbulent friction and frictional heating.

In the following sections we discuss the importance of small-scale turbulence and internal gravity waves for the different atmospheric layers. Afterwards, the specific problems of existing methods to represent these subscale motions in atmospheric circulation models are considered, and the goals of this study are outlined.

1.1 Role of turbulent dissipation in the general circulation of the troposphere

The energetics of the general circulation of the troposphere is known as the Lorenz energy cycle (e.g., Oort, 1964; Lorenz, 1967; James, 1994, section 5.3). It can be described as follows. Available potential energy (Lorenz, 1955) is generated by differential diabatic heating owing to radiation, latent heating, and surface sensible heat flux. On the climatological time scale, this generation is balanced by adiabatic conversion of available potential into kinetic energy due to the action of baroclinic waves and Rossby waves. The horizontal scales of these wave systems reach from 500 km for synoptic baroclinic waves to more than 10000 km for planetary Rossby waves. In turn, kinetic energy is removed from the flow by turbulent friction, and it is ultimately converted into heat by frictional heating (other equivalent terms are dissipation, dissipative heating, or frictional dissipation). Existing estimates based on observational data yield a value of about 2 Wm^{-2} for the net generation of large-scale available potential energy (Oort, 1964). In the long-term average, this generation must be balanced by the subsequent conversion processes. Therefore, the dissipation owing to synoptic and planetary waves is on average about 2 Wm^{-2}. This value means that an amount of kinetic energy equivalent to that typically contained in the entire atmosphere ($\sim 1.6 \times 10^6$ Jm^{-2}) is dissipated within about 9 days (e.g., Pichler, 1986, chapter 9).

Differential diabatic heating decreases the entropy of the atmosphere. This decrease must be balanced by irreversible processes such as heat conduction and frictional heating. The latter processes are therefore essential to the entropy budget of the atmosphere. Also the energy budget depends crucially on the energy conversion processes associated with turbulent friction. On the climatological global scale, the net thermal forcing – that is, the sum of diabatic heating owing to radiation, condensation, and surface sensible heat flux – must be zero. Therefore, the net diabatic heating of the atmosphere is due to frictional heating, and this heating is positive (Lorenz, 1967, chapter V). Consequently, an atmospheric circulation model without this heating, but with realistic dynamics otherwise, requires an artificial net thermal forcing of about 2 Wm^{-2} by definition. Such a forcing is of the same order of magnitude as the net radiative forcing associated with enhanced

greenhouse gas concentrations (IPCC, 1994).

These arguments are simplified by presuming that there is no additional conversion of available potential energy into kinetic energy at mesoscales (horizontal scale between about 5 and 500 km). However, it has been noted in several studies that this is not the case. The dissipation of kinetic energy generated by mesoscale convective circulation systems may indeed be important in the global energy and entropy budgets (Renno and Ingersol, 1996; Pauluis and Held, 2002). Moreover, frictional heating may substantially affect the dynamics of tropical cyclones (Bister and Emanuel, 1998). Direct numerical simulations of deep convection also reveal the possibility of an inverse cascade of turbulent kinetic energy in the mesoscales (Vallis et al., 1997). Thus the value of 2 Wm^{-2} represents a lower bound only for the net dissipation in the atmosphere.

1.2 Role of gravity waves and turbulent dissipation in the general circulation of the middle atmosphere

We now consider the heat budget of the middle atmosphere (height region between about 15 and 100 km) with particular emphasis on the energetics associated with the breakdown of internal gravity waves (IGWs). This represents another example for the mutual dependence of atmospheric waves and small-scale turbulence, and, in particular, for the subscale generation of kinetic energy by adiabatic conversion.

The transformed Eulerian mean equations (e.g., Andrews et al., 1987, chapter 3) provide a suitable picture for the zonally averaged circulation of the middle atmosphere. In this framework, the waves *drive* a mean meridional circulation, the so-called *residual circulation* (see Figs. 8d and 20d). The wave driving is defined by the quasi-geostrophic balance between the Coriolis force associated with the residual meridional wind and the mean zonal drag generated by wave-mean flow interactions. The latter is known as the *Eliassen-Palm flux divergence*. To a first approximation, the residual circulation is thermally balanced by radiative heating/cooling.[1] It describes approximately the averaged trajectories of air parcels, whereas the corresponding Eulerian mean meridional circulation (see Figs. 8c and 20c) describes the averaged mass flux. Out of the deep tropics, no residual circulation can exist without an appropriate zonal wave drag (Holton et al., 1995; Becker and Schmitz, 1999).

In the stratosphere (height region between about 15 and 50 km) the residual circulation is primarily driven by planetary Rossby waves (e.g., Rosenlof and Holton, 1993). These waves are generated in the troposphere by the major mountain ranges and land-sea

[1] In the upper mesosphere, also chemical heating rates become important.

heating contrasts. Since the Rossby wave generation is particularly strong in the boreal winter hemisphere, there exists a pronounced north-south asymmetry with regard to the extratropical winter climate of the stratosphere (e.g., Yulaeva et al., 1994). In particular, the stratospheric polar night jet is much stronger, colder, and more stable in austral winter than in boreal winter. Also tropical upwelling is considered to be induced by extratropical planetary waves (Becker and Schmitz, 1999). Almost no residual circulation exists in the summer stratosphere since prevailing easterlies suppress the propagation of quasi-stationary Rossby waves.

In the mesosphere, and particularly in the MLT, the wave drag due to planetary waves diminishes, and IGWs drive a strong summer-to-winter-pole residual circulation. IGWs are generated in the troposphere, for instance by convection or flow over topography, and around the tropopause level by shear instability of the jet streams. Propagating upward into the mesosphere, IGWs become statically unstable mainly as a result of decreasing density.[2] In the theory of Lindzen (1981) it is assumed that, above this level, turbulent diffusion sets in such as to keep the wave at marginal static instability until a critical level is encountered. By this mechanism, known as gravity wave saturation, the nonconservative propagation of IGWs is tied up with the accompanying small-scale turbulence.

The adiabatic cooling and heating rates associated with the IGW-driven upper branch of the residual circulation are strong enough to account for a reversal of the summer-to-winter-pole temperature gradient. This is the usual explanation for the peculiar thermal structure of the MLT. Indeed, the high-latitude summer mesopause is the coldest place of the terrestrial atmosphere with observed temperatures as low as $\sim$ 130 K (e.g., Lübken et al., 1999), which is about 100 degrees below the radiatively determined state (see for instance Fig. 20a). However, the dynamics of the MLT is complicated by several other processes. First, the breakdown of atmospheric tides accounts for wave-mean flow interactions at low latitudes. Second, planetary wave activity in the underlying atmospheric layers can efficiently modulate the propagation and breakdown of IGWs on both the intraseasonal scale, for example during sudden warming events (Holton, 1983), and on the climatological scale as well (Becker and Schmitz, 2003). Third, the direct heating rates associated with IGW breakdown – such as energy deposition, turbulent dissipation, and turbulent diffusion – are believed to give important contributions to the heat budget of the MLT. While corresponding model estimates appear to be less certain, it is important to mention state-of-the-art rocket-borne in-situ measurements of Lübken (1992; 1997a,b). These experiments indicate that in the summer MLT the local frictional heating amounts on average to 10-20 Kd^{-1}. Such values are comparable to the radiative heating. If they

[2]Also the dependence of the vertical wave number on the mean wind controls the static stability of IGWs.

are in fact representative, our present understanding of the heat budget of the MLT needs to be revised.

1.3 Problems with existing parameterizations of turbulent friction and gravity wave breaking

Given the aforementioned importance of turbulent friction and dissipation, it appears necessary that general circulation models of the atmosphere account for these processes in a physically consistent manner. However, this is not the case yet as outlined below.

In the troposphere, the large-scale adiabatic conversion of the available potential energy into kinetic energy is concentrated at scales of about 3000-6000 km. Due to the dynamics of planetary and synoptic waves, kinetic energy is transferred to larger scales while enstrophy and an additional amount of kinetic energy are transferred to smaller scales (e.g., Salmon, 1998, chapter 4). Of course, the upscaling of kinetic energy in the planetary regime is ultimately balanced by downscaling due to the action of turbulent friction in the boundary layer. On the other hand, the downscaling in the synoptic regime is balanced by some turbulent friction that is independent from the vertical wind shear (Pedlosky, 1987, section 4.14). Therefore, a parameterization of turbulent friction in the free atmosphere must be scale-selective of the horizontal motion. In general circulation models of the atmosphere (hereafter GCMs), this is achieved by empirically adding some scale-selective damping terms to the equations of motion. An explicit horizontal momentum diffusion, i.e. an even power of the horizontal Nabla operator applied to the horizontal wind vector, is most common and works sufficiently well (Smagorinsky, 1963). Order and magnitude of this scheme are adapted to the spatial resolution of a particular GCM in order to suppress truncation errors and to achieve a realistic climatology. The effects of different orders and magnitudes of horizontal momentum diffusion have been analysed for instance by Barnes and Young (1992), Laursen and Eliassen (1989), or Alekseev et al. (1996). It is, however, a first principle of fluid mechanics that friction must be formulated as the divergence of a symmetric stress tensor. Otherwise the Eulerian law of angular momentum conservation for finite fluid volumes is not fulfilled (e.g., Serrin, 1959, section 7; Szabó, 1977, chapter IB; Lindzen, 1990, section 6.2). Since the Reynolds stress tensor is symmetric by definition, the symmetry constraint applies to molecular friction and turbulent friction as well. It has been noted in Becker (2001) that existing horizontal momentum diffusion schemes are generally not derived from a symmetric stress tensor. Particularly the conventional explicit diffusion corresponds to a nonsymmetric stress tensor.

Another problem of conventional friction parameterizations is concerned with the laws

of thermodynamics. Friction changes the total energy of a finite fluid volume via the boundary stress. To satisfy the energy conservation law, one must generally include the frictional heating in the thermodynamic equation of motion (e.g., Serrin, 1959; Lindzen, 1990). It is furthermore evident that turbulent friction describes an irreversible process. Hence, in addition to the symmetry of the stress tensor, we have to require that the frictional heating must not be negative.

In present-day GCMs the frictional heating is usually ignored, presumably because, in the troposphere, it is very small against other contributions to the heat budget such as radiative or latent heating. On the other hand, the dissipation never averages out; it accumulates both in space and time. As noted above, this heating is essential if a precise energy budget is needed, for example in climate change simulations. Moreover, the dissipation may become very strong in the mesosphere.

An attempt to include frictional heating in GCMs can be found in Hamilton (1996) or Kiehl et al. (1996, Sections 3b and 4d). With this method no knowledge of the stress tensor is required. Rather, one assumes that, locally, the rate of change of kinetic energy due to friction enters the thermodynamic equation of motion with negative sign. This assumption may be interpreted as the local counterpart of the fact that, in the global mean, the frictional loss of kinetic energy balances the frictional heating (e.g., Pichler, 1986, chapter 9; Smagorinsky, 1993; section 4.1). However, assuming local equivalence implies that there is no turbulent stress at all acting at the resolved scales. Also does the local frictional heating rate have arbitrary sign. Therefore, the simple ansatz proposed by Hamilton or Kiehl et al. is not consistent with the hydrodynamic formulation. This notion contrasts with comments of Fiedler (2000) concerning the model description of the NCAR community climate model.

As long as IGWs are negligible, the unresolved motion of an atmospheric circulation model may approximately be parameterized by diffusion of momentum and heat, where the particular turbulence model is hidden behind the definitions of the diffusion and surface coefficients. This approach is appropriate in the troposphere and to some extent in the stratosphere only. Indeed, IGWs become important even in the lower stratosphere (e.g., Sausen et al., 1993), and they control the general circulation of the mesosphere. These wave disturbances are nondiffusive, and, at present, they cannot be resolved reasonably in GCMs, even not in very high resolution simulations (Koshyk and Hamilton, 2001). Hence, IGWs must be parameterized along with the turbulent diffusion. This represents a conceptional difficulty with regard to the direct heating rates owing to gravity wave-mean flow interaction and turbulent diffusion.

Several concepts to parameterize these heating rates can be found in the literature. For instance, Hines (1997,1999), Fritts and van Zandt (1993), Fritts and Werne (2000),

or Akmaev (2001) propose that the heating of the mean flow owing to wave-mean flow interaction (hereafter the *energy deposition*) is 'available for dissipation'. Such an interpretation is questionable since turbulent diffusion and convergence of the vertical wave fluxes are distinct processes associated with IGWs breaking in the middle atmosphere (Lindzen, 1981 and 1984). Even though momentum and energy deposition occur as a consequence of a diabatic process – for example damping of the wave amplitudes by turbulent diffusion as in saturation theory –, they represent wave-mean flow interactions and must be regarded as dynamic processes.[3] The turbulent dissipation owing to gravity wave breakdown should rather be identified as the frictional heating associated with turbulent momentum diffusion (Becker and Schmitz, 2002), and its relationship with the energy deposition should be investigated. Summarizing, a generally accepted theoretical concept of the direct heating rates associated with gravity wave-mean flow interaction and gravity wave-induced turbulent diffusion is not yet available.

1.4 Outline of this study

The present study proposes methods by which the aforementioned problems may be solved. In chapter 2 we recapitulate some general concepts concerning the action of subscale motions on the mean flow, and we identify the specific approximations which apply to small-scale turbulence on the one hand and to internal gravity waves on the other. An energetically consistent formulation of the primitive equations completed by turbulent diffusion and gravity wave fluxes is proposed.

The issue of how to formulate momentum diffusion and dissipation for the primitive equations in a hydrodynamically consistent way is addressed in chapter 3. In particular, a symmetric stress tensor formulation for horizontal momentum diffusion is given. The derivation is based on the constraint that, for a mere scale-selective damping of the horizontal motion, the frictional stress acting on horizontally aligned Eulerian sectional planes must vanish (Becker, 2001). Furthermore, the dissipation associated with vertical momentum diffusion (van Mieghem, 1973, section 9.3; Smagorinsky; 1993) is recapitulated, and an appropriate finite-difference form is proposed in chapter 4. This new numerical scheme is derived from the energy conservation constraint. More precisely, the general prerequisite that the work done by surface friction vanishes according to the no-slip condition is utilized (Becker, 2003). The resulting finite-difference form is designed to be implemented along with the hybrid coordinate system of Simmons and Burridge (1981) which is stan-

[3] This reasoning is analogous to the action of synoptic and planetary waves which maintain the general circulation in the troposphere by advecting momentum and enthalpy poleward. Obviously, the associated dynamic heating in the middle latitudes cannot be interpreted as dissipation.

dard in many present-day GCMs. The proposed scheme applies to both boundary layer mixing and the direct thermodynamic effects associated with gravity wave breakdown in the MLT.

Chapter 5 presents numerical experiments in order to test the new friction and dissipation forms against the corresponding conventional methods. First, the adiabatic life cycle of a baroclinic wave is revisited. Second, we utilize a simplified but nevertheless realistic troposphere-stratosphere GCM (Becker and Schmitz, 2001) in order to assess the sensitivity of the simulated general circulation to the neglect of frictional heating and asymmetry of the stress tensor. It is found that the simulated turbulent dissipation is mainly due to boundary layer mixing. A global mean frictional heating rate of about 2 Wm^{-2} is obtained, which is quantitatively consistent with the observational estimate associated with synoptic and planetary waves.

Chapter 6 starts with the presentation of Lindzen's gravity wave saturation theory completed by the analytical forms of the direct heating rates associated with wave-mean flow interaction and frictional heating. These forms are applied in corresponding numerical experiments. For this purpose the vertical domain of the simple GCM is extended up to about 100 km. The gravity wave parameterization is implemented in line with the aforementioned vertical discretization scheme. A special consequence of Lindzen's theory is that all direct heating rates owing to gravity wave breakdown can be defined without the need for additional free parameters other than those specifying the gravity wave momentum flux launched around the tropopause. The only exception is the vertical diffusion of mean entropy which is scaled by a Prandtl number. Nevertheless, from Lindzen's theory we can derive an upper bound of 2 for the effective Prandtl number that scales the total entropy flux owing to gravity waves and wave-induced turbulence. The so-defined model predicts reasonable dissipative heating rates in the MLT, once the gravity wave source is adjusted to drive a realistic residual circulation.

Chapter 7 gives a concluding discussion. The simple GCM employed in the present study is the *Kühlungsborn Mechanistic general Circulation Model* (*KMCM*). It is described in the course of this study. Additional model details can be found in appendix A.

Chapter 2

General remarks on the energetics of atmospheric flow

In this chapter we shall derive an energetically consistent form of the primitive equations completed by turbulent diffusion and gravity wave-mean flow interaction. To the best of my knowledge such an approach cannot be found in textbooks. Becker and Schmitz (2002) have already given a corresponding formulation of the primitive equations by assuming that the energy conservation law is satisfied by the mean flow. Here we do not start from this axiomatic constraint. Instead, we begin with the first principles of hydrodynamics. Turbulent motions and gravity waves are subsequently filtered out, and the shallow atmosphere approximations are applied. In this fashion we recover all approximations that lead to the conservation laws satisfied by the final model equations. With respect to gravity waves, a corresponding analysis has been sketched in the appendix of the paper of Becker and Schmitz (2002). With respect to turbulence, the presentation follows van Mieghem (1973).

2.1 Filtering out subscale motions

2.1.1 General method

Let us consider the Navier-Stokes equations completed by the Coriolis force and the thermodynamic equation of motion in geophysical spherical coordinates:

$$(\partial_t + \mathbf{v}_3 \cdot \nabla_3) \, \mathbf{v}_3 + 2 \, \mathbf{\Omega} \times \mathbf{v}_3 = -\rho^{-1} \, \nabla_3 \, p - g \, \mathbf{e}_z + \rho^{-1} \, \nabla_3 \, \mathsf{P} \tag{2.1}$$

$$\partial_t \, \rho + \nabla_3 \cdot (\, \rho \, \mathbf{v}_3 \,) = 0 \tag{2.2}$$

$$(\partial_t + \mathbf{v}_3 \cdot \nabla_3) \, h = \rho^{-1} \, (\partial_t \, p + \mathbf{v}_3 \cdot \nabla_3 p) + c_p \, Q - \rho^{-1} \, \nabla_3 \cdot \mathbf{q} + \rho^{-1} \, (\, \mathsf{P} \, \nabla_3 \,) \cdot \mathbf{v}_3 \, . \tag{2.3}$$

Horizontal and vertical velocity components are abbreviated by $\mathbf{v}$ and w such that $\mathbf{v}_3 = \mathbf{v} + w\,\mathbf{e}_z$, where $\mathbf{e}_z$ is the unit vector in vertical direction. Similarly we write $\nabla_3 = \nabla + \mathbf{e}_z\,\partial_z$ with the horizontal gradient operator given by

$$\nabla = \mathbf{e}_x \partial_x + \mathbf{e}_y \partial_y = \mathbf{e}_x \frac{\partial_\lambda}{r\cos\phi} + \mathbf{e}_y \frac{\partial_\phi}{r}\,. \tag{2.4}$$

Here, $\mathbf{e}_x$ and $\mathbf{e}_y$ are the unit vectors in zonal and meridional direction, while λ and ϕ are geographical longitude and latitude. Furthermore we have $r = a_e + z$, where a_e is the earth radius. The molecular stress tensor is written as P, h is the enthalpy per unit mass, and $\mathbf{q}$ is the molecular heat flux. The external diabatic forcing by radiation and latent heating is represented by Q. The other symbols have their usual meanings. The system (2.1)-(2.3) fulfills the following energy conservation law

$$\begin{aligned} &\partial_t \{\, \rho\, (\, e + \frac{\mathbf{v}_3^2}{2}\,)\,\} + \nabla_3 \cdot \{\, \rho\, \mathbf{v}_3\, (\, e + \frac{\mathbf{v}_3^2}{2}\,)\,\} \\ &= \; -\rho\, g\, w + \rho\, Q + \nabla_3 \cdot \{\, (\,\mathsf{P} - p\,\mathsf{I}\,)\,\mathbf{v}_3 \; - \mathbf{q}\,\}\,, \end{aligned} \tag{2.5}$$

where $e = h - p/\rho$ is the internal energy per unit mass and the symbol I denotes the idem factor. Equation (2.5) states that, for any fluid volume, friction and pressure can change the total energy via the boundary stresses only.

Small-scale fluctuations can be filtered out using ordinary and density weighted averages of any quantity X:

$$X = \overline{X} + X'\,, \quad \overline{X'} \equiv 0 \tag{2.6}$$

$$X = \overline{\overline{X}} + X''\,, \quad \overline{\overline{X''}} = 0\,, \quad \overline{\overline{X}} := \overline{\rho}^{\,-1}\,\overline{\rho\, X}\,. \tag{2.7}$$

The average is assumed to extend over the typical spatial and/or temporal scales of the subscale motion in question. Owing to (2.6) and (2.7), the governing equations (2.1)-(2.3) are transformed to

$$(\,\partial_t + \overline{\overline{\mathbf{v}}}_3 \cdot \nabla_3\,)\,\overline{\overline{\mathbf{v}}}_3 + 2\,\mathbf{\Omega} \times \overline{\overline{\mathbf{v}}}_3 = -\overline{\rho}^{\,-1}\,\nabla_3\,\overline{p} - g\,\mathbf{e}_z + \overline{\rho}^{\,-1}\,\nabla_3 \overline{\mathsf{P}} + \overline{\rho}^{\,-1}\,\nabla_3 \mathbf{\Sigma} \tag{2.8}$$

$$\partial_t\,\overline{\rho} + \nabla_3 \cdot (\,\overline{\rho}\,\overline{\overline{\mathbf{v}}}_3\,) = 0 \tag{2.9}$$

$$\begin{aligned} (\,\partial_t + \overline{\overline{\mathbf{v}}}_3 \cdot \nabla_3\,)\,\overline{\overline{h}} + \overline{\rho}^{\,-1}\,\nabla_3 \cdot \mathbf{J} \;&=\; \overline{\rho}^{\,-1}\,(\,\partial_t\,\overline{p} + \overline{\overline{\mathbf{v}}}_3 \cdot \nabla_3\,\overline{p} + \overline{\mathbf{v}_3'' \cdot \nabla_3\, p}\,) + c_p\,\overline{\overline{Q}} \\ &\quad + \overline{\rho}^{\,-1}(\,\overline{\mathsf{P}}\,\nabla_3\,) \cdot \overline{\overline{\mathbf{v}}}_3 + \overline{\rho}^{\,-1}\,\overline{(\,\mathsf{P}\,\nabla_3\,) \cdot \mathbf{v}_3''} - \overline{\rho}^{\,-1}\,\nabla_3 \cdot \overline{\mathbf{q}}\,. \end{aligned} \tag{2.10}$$

The Reynolds stress tensor is defined as

$$\mathbf{\Sigma} := -\overline{\rho}\,\overline{\overline{\mathbf{v}_3'' \circ \mathbf{v}_3''}}\,, \tag{2.11}$$

where the tensor product is indicated by an open circle. The convention is such that $(\mathbf{a}\circ\mathbf{b})\,\mathbf{c}=\mathbf{a}\,(\mathbf{b}\cdot\mathbf{c})$ and $\mathbf{a}\,(\mathbf{b}\circ\mathbf{c})=(\mathbf{a}\cdot\mathbf{b})\,\mathbf{c}$ for arbitrary vectors $\mathbf{a}$, $\mathbf{b}$, and $\mathbf{c}$. Note that Σ is symmetric by definition.

The symbol $\mathbf{J}$ denotes the subscale flux of sensible heat, which in the case of an ideal gas can be expressed as (van Mieghem, 1973, chapter 7)

$$\mathbf{J}:=\overline{\rho}\;\overline{\mathbf{v}_3''\,h''}=\overline{p'\,\mathbf{v}_3''}+c_p\,\overline{\rho}\,\overline{\overline{T}\,\overline{\Theta}^{-1}}\;\overline{\Theta''\mathbf{v}_3''}\,. \tag{2.12}$$

Here, $\Theta=T\,(p_{00}/p)^{R/c_p}$ is the potential temperature, and $p_{00}=1013$ mb denotes a reference sea level pressure. Furthermore, c_p is the heat capacity at constant pressure, and R is the gas constant. The entropy per unit mass s is a function of Θ by means of $d\,s=c_p\,\Theta^{-1}\,d\,\Theta$.

From (2.8) and (2.9) one obtains the following equation for the kinetic energy of the mean flow

$$\partial_t\,\{\,\overline{\rho}\,\frac{\overline{\overline{\mathbf{v}}}_3^{\,2}}{2}\,\}+\nabla_3\cdot\{\,\overline{\rho}\,\overline{\overline{\mathbf{v}}}_3\,\frac{\overline{\overline{\mathbf{v}}}_3^{\,2}}{2}\,\}=-\overline{\rho}\,g\,\overline{\overline{w}}+\overline{\overline{\mathbf{v}}}_3\cdot\{\,\nabla_3\,(\,\overline{\mathsf{P}}+\Sigma-\mathsf{I}\,\overline{p}\,)\,\}\,. \tag{2.13}$$

Similarly, (2.9) and (2.10) yield for the internal energy of the mean flow

$$\begin{aligned}\partial_t\,\{\,\overline{\rho}\,\overline{\overline{e}}\}+\nabla_3\cdot\{\,\overline{\rho}\,\overline{\overline{\mathbf{v}}}_3\,\overline{\overline{e}}\,\}\;&=\;-\overline{p}\,\nabla_3\cdot\overline{\overline{\mathbf{v}}}_3+c_p\,\overline{\rho}\,\overline{\overline{Q}}+(\,\overline{\mathsf{P}}\,\nabla_3\,)\cdot\overline{\overline{\mathbf{v}}}_3\\&\quad-\nabla_3\cdot(\,\overline{\mathbf{q}}+\mathbf{J}\,)+\overline{\mathbf{v}_3''\cdot\nabla_3\,p}+\overline{(\,\mathsf{P}\,\nabla_3\,)\cdot\mathbf{v}_3''}\,.\end{aligned} \tag{2.14}$$

In order to formulate an energy conservation constraint analogous to (2.5), we must also take the kinetic energy of the subscale motion into account. For this purpose we write $\mathbf{v}_3=\overline{\overline{\mathbf{v}}}_3+\mathbf{v}_3''$ in the momentum equation (2.1), multiply by $\rho\,\mathbf{v}_3''$, and take the average. The result may be written as (see van Mieghem, 1973, Eqs. (6.8) and (6.9))

$$\begin{aligned}\overline{\rho\,\dot{k}_e}\;&:=\;\partial_t\,\{\,\overline{\rho}\,\overline{\overline{k_e}}\}+\nabla_3\cdot\{\,\overline{\rho}\,\overline{\overline{\mathbf{v}}}_3\,\overline{\overline{k_e}}\,\}+\nabla_3\cdot\{\,\overline{\rho\,\mathbf{v}_3''\,k_e}\,\}\\&=\;(\,\Sigma\,\nabla_3\,)\cdot\overline{\overline{\mathbf{v}}}_3-\overline{\mathbf{v}_3''\cdot\nabla_3\,p}+\overline{\mathbf{v}_3''\cdot(\,\nabla_3\,\mathsf{P}\,)}\end{aligned} \tag{2.15}$$

with $k_e:=(\,\mathbf{v}_3''\,)^{\,2}/2$. The second term on the rhs of the second Eq. (2.15) is the generation of eddy kinetic energy by adiabatic conversion of mean enthalpy. If (2.15) is applied to a control volume large enough such that the boundary integral of $\Sigma\,\overline{\overline{\mathbf{v}}}_3$ is negligible, the volume integral of $(\,\Sigma\,\nabla_3\,)\cdot\overline{\overline{\mathbf{v}}}_3$ represents the transfer of mean kinetic energy into eddy kinetic energy.

Adding (2.15) to the sum of (2.13) and (2.14) yields the following energy conservation law for the total energy of the mean and subscale motion:

$$\begin{aligned}&\partial_t\,\{\,\overline{\rho}\,(\,\overline{\overline{e}}+\frac{\overline{\overline{\mathbf{v}}}_3^{\,2}}{2}+\overline{\overline{k_e}}\,)\}+\nabla_3\cdot\{\,\overline{\rho}\,\overline{\overline{\mathbf{v}}}_3\,(\,\overline{\overline{e}}+\frac{\overline{\overline{\mathbf{v}}}_3^{\,2}}{2}+\overline{\overline{k_e}}\,)+\overline{\rho\,\mathbf{v}_3''\,k_e}\,\}\\&=\;c_p\,\overline{\rho}\,\overline{\overline{Q}}-\overline{\rho}\,g\,\overline{\overline{w}}+\nabla_3\cdot\{\,(\,\overline{\mathsf{P}}+\Sigma-\mathsf{I}\,p\,)\,\overline{\overline{\mathbf{v}}}_3\,\}-\nabla_3\cdot(\,\overline{\mathbf{q}}+\mathbf{J}\,)+\nabla_3\cdot(\,\overline{\mathsf{P}\,\mathbf{v}_3''}\,)\,.\end{aligned} \tag{2.16}$$

So far we have not introduced any approximations.

2.1.2 The Boussinesq approximation

It is suitable to apply the well-known Boussinesq approximation to small-scale turbulence (e.g., van Mieghem, 1973; Pichler, 1986) and to internal gravity waves as well (Lindzen, 1981). In general, this approximation assumes that sound waves are negligible, and that the typical vertical scales of the subscale motion are small against the scale height of the mean flow. As a result, all density weighted averages can be substituted by ordinary averages, and, except for the adiabatic conversion term, all deviations from mass weighted averages can be substituted by deviations from ordinary averages. If the mean flow is approximately in hydrostatic balance, the adiabatic conversion term can be written as (van Mieghem, 1973, chapter 8)

$$\overline{\mathbf{v}_3'' \cdot \nabla_3 p} \;=\; \nabla_3 \cdot \overline{p' \, \mathbf{v}_3'} + g \, \overline{\rho' \, w'} \,. \tag{2.17}$$

The exclusion of sound waves implies

$$\rho' \,/\, \overline{\rho} \;=\; -\,\Theta' \,/\, \overline{\Theta} \,, \tag{2.18}$$

hence

$$\overline{\mathbf{v}_3'' \cdot \nabla_3 p} \;=\; \nabla_3 \cdot \overline{p' \, \mathbf{v}_3'} - g \, \overline{\rho} \, \overline{\Theta}^{-1} \, \overline{\Theta' \, w'} \,. \tag{2.19}$$

It is furthermore appropriate to assume that the averaged dissipation associated with the subscale motion and the averaged frictional loss of subscale kinetic energy balance each other, i.e.

$$-\overline{\rho}^{\,-1} \, \overline{\mathbf{v}_3' \cdot (\, \nabla_3 \, \mathsf{P}' \,)} = \overline{\rho}^{\,-1} \, \overline{(\, \mathsf{P}' \, \nabla_3 \,) \cdot \mathbf{v}_3'} \,. \tag{2.20}$$

Then, dropping the averaging operator with respect to mean flow components, the momentum and thermodynamic equations of motion can be written as

$$\begin{aligned}
(\, \partial_t + \mathbf{v}_3 \cdot \nabla_3 \,) \, \mathbf{v}_3 + 2 \, \mathbf{\Omega} \times \mathbf{v}_3 \;&=\; -\rho^{-1} \, \nabla_3 \, p - g \, \mathbf{e}_z + \rho^{-1} \, \nabla_3 \, (\, \Sigma + \mathsf{P} \,) && (2.21) \\
(\, \partial_t + \mathbf{v}_3 \cdot \nabla_3 \,) \, h \;&=\; \rho^{-1} \, (\, \partial_t \, p + \mathbf{v}_3 \cdot \nabla_3 \, p \,) + c_p \, Q && (2.22) \\
&\qquad -\rho^{-1} \, \nabla_3 \cdot (\, \mathbf{J} + \mathbf{q} \,) + \rho^{-1} \, \{ \, (\, \Sigma + \mathsf{P} \,) \, \nabla_3 \, \} \cdot \mathbf{v}_3 - \overline{\dot{k}_e} \,,
\end{aligned}$$

where

$$\begin{aligned}
\Sigma \;&=\; -\rho \, \overline{\mathbf{v}_3' \circ \mathbf{v}_3'} && (2.23) \\
\mathbf{J} \;&=\; \rho \, \overline{\mathbf{v}_3' \, h'} \;=\; \overline{p' \, \mathbf{v}_3'} \;+\; c_p \, \rho \, T \, \Theta^{-1} \, \overline{\Theta' \mathbf{v}_3'} && (2.24) \\
\rho \, \overline{\dot{k}_e} \;&:=\; \partial_t \, (\, \rho \, \overline{k_e} \,) + \nabla_3 \cdot (\, \rho \, \mathbf{v}_3 \, \overline{k_e} \,) + \nabla_3 \cdot (\, \rho \, \overline{\mathbf{v}_3' \, k_e} \,) && (2.25) \\
&=\; (\, \Sigma \, \nabla_3 \,) \cdot \mathbf{v}_3 - \nabla_3 \cdot \overline{\mathbf{v}_3' \, p'} + g \, \rho \, \Theta^{-1} \, \overline{\Theta' \, w'} \;-\; \overline{(\, \mathsf{P}' \, \nabla_3 \,) \cdot \mathbf{v}_3'}
\end{aligned}$$

and $k_e := (\mathbf{v}_3')^2/2$. The continuity equation takes the form (2.2)[1], and the energy conservation law yields

$$\begin{aligned} &\partial_t \{ \rho (e + \frac{\mathbf{v}_3^2}{2}) \} + \nabla_3 \cdot \{ \rho (e + \frac{\mathbf{v}_3^2}{2}) \mathbf{v}_3 \} \\ &\quad = c_p \rho Q - \rho g w + \nabla_3 \cdot \{ (\Sigma + \mathsf{P} - \mathsf{I} p) \mathbf{v}_3 \} - \nabla_3 \cdot (\mathbf{J} + \mathbf{q}) - \rho \overline{\dot{k}_e} . \end{aligned} \tag{2.26}$$

Except for $\rho \overline{\dot{k}_e}$, the system (2.21),(2.2),(2.22),(2.26) is quite analogous to the original system (2.1)-(2.3),(2.5). That is, velocity, enthalpy, internal energy, density, and pressure are substituted by the corresponding mean fields, while the molecular stress tensor P and the molecular heat flux $\mathbf{q}$ are supplemented by the Reynolds stress tensor Σ and the eddy heat flux $\mathbf{J}$.

2.2 Approximations in the case of small-scale turbulence

When the formalism of the previous section is used to filter out small-scale turbulent motions, two additional simplifications apply: the molecular stress and the molecular heat flux associated with the mean flow can be dropped, and pressure perturbations are generally negligible. With these idealizations the momentum and thermodynamic equations of motion, the turbulent heat flux, and the kinetic energy equation can be written as

$$(\partial_t + \mathbf{v}_3 \cdot \nabla_3) \mathbf{v}_3 + 2 \mathbf{\Omega} \times \mathbf{v}_3 = -\rho^{-1} \nabla_3 p - g \mathbf{e}_z + \rho^{-1} \nabla_3 \Sigma \tag{2.27}$$

$$\begin{aligned} (\partial_t + \mathbf{v}_3 \cdot \nabla_3) h &= \rho^{-1} (\partial_t p + \mathbf{v}_3 \cdot \nabla_3 p) + c_p Q \\ &\quad -\rho^{-1} \nabla_3 \cdot \mathbf{J} + \rho^{-1} (\Sigma \nabla_3) \cdot \mathbf{v}_3 - \overline{\dot{k}_e} \end{aligned} \tag{2.28}$$

$$\mathbf{J} = c_p \rho T \Theta^{-1} \overline{\Theta' \mathbf{v}_3'} \tag{2.29}$$

$$\overline{\dot{k}_e} = \rho^{-1} (\Sigma \nabla_3) \cdot \mathbf{v}_3 + g \Theta^{-1} \overline{\Theta' w'} - \epsilon . \tag{2.30}$$

Here, ϵ is the turbulent dissipation defined as

$$\epsilon := -\rho^{-1} \overline{\mathbf{v}_3' \cdot (\nabla_3 \mathsf{P}')} = \rho^{-1} \overline{(\mathsf{P}' \nabla_3) \cdot \mathbf{v}_3'} > 0 . \tag{2.31}$$

The corresponding energy conservation law yields

$$\begin{aligned} &\partial_t \{ \rho (\frac{\mathbf{v}_3^2}{2} + e) \} + \nabla_3 \cdot \{ \rho (\frac{\mathbf{v}_3^2}{2} + e) \mathbf{v}_3 \} \\ &\quad = c_p \rho Q - \rho g w + \nabla_3 \cdot \{ (\Sigma - \mathsf{I} p) \mathbf{v}_3 \} - \nabla_3 \cdot \mathbf{J} - \rho \overline{\dot{k}_e} . \end{aligned} \tag{2.32}$$

[1] The perturbation flow satisfies $\nabla_3 \cdot \mathbf{v}_3' = 0$.

The divergences of the Reynolds stress tensor Σ and of the turbulent heat flux $\mathbf{J}$ are usually parameterized by diffusion of momentum and potential temperature. These parameterizations must be completed by appropriate dynamic boundary conditions. The body of such a turbulence model is hidden behind the definitions of the diffusion and surface coefficients (e.g., Haltiner and Williams, 1980, section 8.9).

To a first approximation, the temporal evolution and the advection of eddy kinetic energy can be neglected in the energy budget, i.e. $\overline{\dot{k}_e} = 0$ (e.g., Panchev, 1971, chapter 8). We will refer to this approximation as *quasi-stationary turbulence*. In more sophisticated turbulence models of the planetary boundary layer including the parameterization of convection, $\overline{k_e}$ is retained as a prognostic variable (e.g., van Mieghem, 1973, section 9.3; Roeckner et al., 1996, section 3.2). In this case, the advection of $\overline{k_e}$ by the mean flow is neglected, the advection by the turbulent flow is represented by diffusion of $\overline{k_e}$, and the dissipation is assumed to behave like some nonlinear damping of $\overline{k_e}$. In any event, the transfer of mean kinetic energy into eddy kinetic energy, $\rho^{-1}(\Sigma\nabla_3)\cdot\mathbf{v}_3$, which formally represents the frictional heating of the mean flow owing to Reynolds stresses, appears as an indispensable part of the rhs of the thermodynamic equation (2.28).

For the remainder of this study we will assume quasi-stationary turbulence. Accordingly, $\overline{\dot{k}_e}$ is canceled on the rhs of (2.28) and (2.32) as well as on the lhs of (2.30). We will furthermore assume that the turbulent motion is maintained by downscaling of kinetic energy only. Then the frictional heating due to Reynolds stresses is equivalent to the turbulent dissipation

$$\epsilon \approx \rho^{-1}(\Sigma\nabla_3)\cdot\mathbf{v}_3 . \tag{2.33}$$

Note however that, with respect to the spatial scales resolved in a GCM, Eq. (2.33) represents a lower bound only for the total dissipation. It describes the dissipation of kinetic energy that is generated at the scales of the mean flow.

2.3 Approximations in the case of internal gravity waves

In the saturation theory of Lindzen (1981) or in the gravity wave model of Matsuno (1982), the interaction between internal gravity waves (IGWs) and the planetary-scale flow results from the damping of the wave amplitudes by turbulent diffusion. This is in accordance with Eliassen and Palm's second theorem (e.g., Lindzen, 1990, Eq. (8.24)) or with the generalized Eliassen-Palm theorem of Andrews and McIntyre (1976; see also Andrews et al., 1987, chapter 3). In this respect the theories of Lindzen or Matsuno reflect the general fact that the energetics of gravity wave-mean flow interaction must be

assessed along with the energetics of the accompanying small-scale turbulent motion. At first sight, this task appears rather complicated. However, we can simplify the analysis if we take advantage of the previous sections.

We start by assuming that the resolved flow still includes gravity waves, and that this flow is described by the governing equations derived in the previous section. In particular, we assume quasi-stationary turbulence together with (2.33). As a result, the governing equation system is perfectly analogous to (2.1)-(2.3). That is, in (2.1)-(2.3) we simply have to substitute P by $\mathsf{\Sigma}$ and $\mathbf{q}$ by $\mathbf{J}$. Then, gravity wave disturbances are filtered out by application of (2.6),(2.7), with the average extending over the typical horizontal and temporal scales of the planetary-scale flow, i.e. a few 1000 km and a few days.[2] Anticipating that turbulence can be represented by diffusion while gravity wave flux convergences are nondiffusive, this average implies a strict separation between the turbulent scale (several ten meters) and the scale of IGWs (typically a few hundred kilometers in the horizontal and several hundred meters in the vertical direction). As pointed out by McIntyre (1989), it is open to question whether such a scale separation can be justified by available observational data. On the other hand, the assumption is inherent in every present-day IGW parameterization designed for GCMs. Thus we stick to the scale separation assumption also in the present study. Furthermore, in analogy to the quasi-stationary turbulence approximation, we neglect the rate of change of IGW kinetic energy in the energy budget of the planetary-scale flow. Finally, applying the Boussinesq approximation to the IGW perturbations, the governing equation system follows directly from section 2.1.2. The momentum and thermodynamic equations are

$$
\begin{aligned}
(\,\partial_t + \mathbf{v}_3 \cdot \nabla_3\,)\,\mathbf{v}_3 &= -2\,\mathbf{\Omega} \times \mathbf{v}_3 - \rho^{-1}\,\nabla_3\,p - g\,\mathbf{e}_z + \rho^{-1}\,\nabla_3\,(\,-\rho\,\overline{\mathbf{v}_3' \circ \mathbf{v}_3'} + \mathsf{\Sigma}\,) \qquad (2.34)\\
(\,\partial_t + \mathbf{v}_3 \cdot \nabla_3\,)\,h &= \rho^{-1}\,(\,\partial_t\,p + \mathbf{v}_3 \cdot \nabla_3\,p\,) + c_p\,Q \qquad (2.35)\\
&\quad -\rho^{-1}\,\nabla_3 \cdot (\,\rho\,\overline{h'\,\mathbf{v}_3'} + \mathbf{J}\,) + \rho^{-1}\,\{\,(\,-\rho\,\overline{\mathbf{v}_3' \circ \mathbf{v}_3'} + \mathsf{\Sigma}\,)\,\nabla_3\,\} \cdot \mathbf{v}_3\,,
\end{aligned}
$$

while the energy conservation law becomes

$$
\begin{aligned}
&\partial_t\,\{\,\rho\,(\,\frac{\mathbf{v}_3^2}{2} + e\,)\} + \nabla_3 \cdot \{\,\rho\,(\,\frac{\mathbf{v}_3^2}{2} + e\,)\,\mathbf{v}_3\,\} \qquad (2.36)\\
&\quad = c_p\,\rho\,Q - \rho\,g\,w + \nabla_3 \cdot \{\,(\,-\rho\,\overline{\mathbf{v}_3' \circ \mathbf{v}_3'} + \mathsf{\Sigma} - \mathsf{I}\,p\,)\,\mathbf{v}_3\,\} - \nabla_3 \cdot (\,\rho\,\overline{h'\,\mathbf{v}_3'} + \mathbf{J}\,)\,.
\end{aligned}
$$

Here, $\rho\,\overline{\mathbf{v}_3' \circ \mathbf{v}_3'}$ describes the nondiffusive momentum fluxes owing to internal gravity waves. The corresponding convergence appearing on the rhs of (2.34) represents the familiar momentum deposition that drives the summer-to-winter-pole residual circulation in the mesosphere. The gravity wave sensible heat flux appearing on the rhs of (2.35) and

[2] Of course, to reasonably resolve the planetary flow in a GCM, the spatial and temporal resolution must be finer than these scales.

(2.36) has the general form

$$\rho\,\overline{\mathbf{v}_3'\,h'} \;=\; \overline{p'\,\mathbf{v}_3'} \;+\; c_p\,\rho\,T\,\Theta^{-1}\,\overline{\Theta'\mathbf{v}_3'}\,. \tag{2.37}$$

This flux is usually approximated by the pressure flux term. However, as will be shown in chapter 6, such an assumption is valid in the case of conservative wave propagation only. In fact, the entropy flux generated by IGWs can by no means be neglected in regions of wave breaking.

Also the kinetic energy equation for gravity waves[3]

$$0 = -(\,\overline{\mathbf{v}_3'\circ\mathbf{v}_3'}\,\nabla_3\,)\cdot\mathbf{v}_3 - \rho^{-1}\,\nabla_3\cdot\overline{\mathbf{v}_3'\,p'} + g\,\Theta^{-1}\,\overline{\Theta'\,w'} \;-\rho^{-1}\,\overline{(\,\boldsymbol{\Sigma}'\,\nabla_3\,)\cdot\mathbf{v}_3'}\,. \tag{2.38}$$

invokes both pressure perturbations and entropy perturbations. Note that (2.38) already provides a balance equation for the turbulent dissipation associated with IGW disturbances (last term on the rhs of (2.38)).

2.4 The primitive equations with parameterizations of small-scale turbulence and internal gravity waves

Numerical models of the general circulation of the atmosphere (GCMs) are based on the shallow-atmosphere version of the governing equations, known as the primitive equations. These invoke the following scale approximations (Phillips, 1973)

$$\begin{aligned}
r &= a_e && (2.39)\\
O(\,\mathbf{v}\,) &= U \approx 30\ \mathrm{ms}^{-1} && (2.40)\\
O(\,\nabla\,) &= L^{-1} \approx (\,3000\ \mathrm{km}\,)^{-1} && (2.41)\\
O(\,\partial_z\,) &= H^{-1} \approx (\,10\ \mathrm{km}\,)^{-1} && (2.42)\\
O(\,w\,) &\le U\,\frac{H}{L} && (2.43)\\
O(\,\nabla\rho\,) &\ll \rho\,/\,L\,, && (2.44)
\end{aligned}$$

as well as the traditional approximation for the Coriolis force (Phillips, 1966).

[3] According to the gravity wave analogue of (2.20)

$$\overline{(\,\boldsymbol{\Sigma}'\,\nabla_3\,)\cdot\mathbf{v}_3'} = -\overline{\mathbf{v}_3'\cdot(\,\nabla_3\,\boldsymbol{\Sigma}'\,)}\,,$$

the averaged dissipation owing to gravity waves is assumed to equal the averaged frictional loss of gravity wave kinetic energy.

As concerns the parameterization of internal gravity waves, horizontal transport is of minor importance such that the single column approximation is quite usual, i.e.

$$\rho \, \overline{\mathbf{v}_3' \circ \mathbf{v}_3'} = \rho \, \{ \, \overline{\mathbf{v}' \, w'} \circ \mathbf{e}_z + \mathbf{e}_z \circ \overline{\mathbf{v}' \, w'} \, \} \tag{2.45}$$

$$\rho \, \overline{h' \, \mathbf{v}_3'} = \{ \, \overline{p' \, w'} + c_p \, \rho \, T \, \Theta^{-1} \, \overline{\Theta' \, w'} \, \} \, \mathbf{e}_z \, . \tag{2.46}$$

We furthermore make use of the following abbreviations for momentum flux, pressure flux, and entropy flux:

$$\mathbf{F} := \rho \, \overline{\mathbf{v}' \, w'} \tag{2.47}$$

$$F_p := \overline{p' \, w'} \tag{2.48}$$

$$F_s := \overline{s' \, w'} = c_p \, \Theta^{-1} \, \overline{\Theta' \, w'} \tag{2.49}$$

Then, the momentum equation (2.34) and the continuity equation are transformed to

$$\partial_t \, \mathbf{v} = \mathbf{v} \times (\, f + \xi \,) \, \mathbf{e}_z - w \, \partial_z \, \mathbf{v} - \nabla \, \frac{\mathbf{v}^2}{2} - \rho^{-1} \, \nabla \, p + \rho^{-1} \, (\, \nabla_3 \, \Sigma \, - \, \partial_z \, \mathbf{F} \,) \tag{2.50}$$

$$0 = \partial_z \, p + g \, \rho \tag{2.51}$$

$$0 = \partial_t \, \rho + \nabla \cdot (\, \rho \, \mathbf{v} \,) + \partial_z \, (\, \rho \, w \,) \, , \tag{2.52}$$

while the thermodynamic equation (2.35) yields

$$\begin{aligned} (\, \partial_t + \mathbf{v}_3 \cdot \nabla_3 \,) \, h = {} & \rho^{-1} \, (\, \partial_t \, p + \mathbf{v}_3 \cdot \nabla_3 \, p \,) + c_p \, Q - \rho^{-1} \, \nabla_3 \cdot \mathbf{J} \\ & - \rho^{-1} \, \partial_z \, (\, F_p + \rho \, T \, F_s \,) - \rho^{-1} \, \mathbf{F} \cdot \partial_z \, \mathbf{v} + \rho^{-1} \, (\, \Sigma \, \nabla_3 \,) \cdot \mathbf{v} \, . \end{aligned} \tag{2.53}$$

Here, the relative vorticity and the Coriolis parameter are denoted by $\xi = \mathbf{e}_z \cdot (\, \nabla \times \mathbf{v} \,)$ and f. Although we have written the three-dimensional tensor divergence $\nabla_3 \, \Sigma$ in Eq. (2.50), only the horizontal components of this divergence are retained. The specification of Σ is the topic of the next chapter.

The turbulent heat flux is specified as usual

$$\mathbf{J} = - c_p \, \rho \, \frac{K_h}{2} \, \nabla \, T \, - \, \mathbf{e}_z \, c_p \, \rho \, K_z \, \frac{T}{\Theta} \, \partial_z \, \Theta \, , \tag{2.54}$$

where K_h and K_z denote the horizontal and vertical diffusion coefficients. The corresponding Prandtl numbers are 2 and 1, respectively. With the aid of (2.44) and the additional scale assumption

$$O \, (\, \nabla K_h \,) \ll K_h \, / \, L \tag{2.55}$$

we have

$$- (\, c_p \, \rho \,)^{-1} \, \nabla_3 \cdot \mathbf{J} = \underbrace{\frac{K_h}{2} \, \nabla^2 \, T}_{=: \, \mu_h} + \underbrace{\rho^{-1} \, \partial_z \, \{ \, \rho \, K_z \, \frac{T}{\Theta} \, \partial_z \, \Theta \, \}}_{=: \, \mu_z} \, . \tag{2.56}$$

Disregarding the gravity wave entropy flux F_s, the heating of the mean flow owing to gravity wave-mean flow interaction is often referred to as the *energy deposition* which is defined as

$$E := -\rho^{-1}\,\partial_z\,F_p\;+\;W_{res}\;,\quad W_{res} := -\rho^{-1}\,\mathbf{F}\cdot\partial_z\,\mathbf{v}\;. \tag{2.57}$$

It consists of the pressure flux convergence plus a residual work that is due to the IGW momentum flux and the mean wind shear (Hines and Reddy, 1967; Becker and Schmitz, 2002). Simplifying the IGW kinetic energy equation (2.38) with the aid of (2.45)-(2.49), we get

$$W_{res} = \rho^{-1}\,\partial_z\,F_p - g\,c_p^{-1}\,F_s + \epsilon_{igw}\;, \tag{2.58}$$

where

$$\epsilon_{igw} := \rho^{-1}\,\overline{(\,\boldsymbol{\Sigma}'\,\nabla_3\,)\cdot\mathbf{v}_3'} \tag{2.59}$$

represents the frictional heating owing to the gravity waves themselves, that is, the turbulent dissipation of gravity wave kinetic energy. The sum of the first and second term on the rhs of (2.58) represents the adiabatic conversion of mean enthalpy into gravity wave kinetic energy. Hence, W_{res} is simply the residuum of dissipation and adiabatic conversion.

In section 1.3 it has been noted that several authors equate the energy deposition E with the turbulent dissipation ϵ_{igw}. Combining (2.57) and (2.58) proves that such an assumption is not correct because of the wave entropy flux:

$$E = -g\,c_p^{-1}\,F_s + \epsilon_{igw}\;. \tag{2.60}$$

Note furthermore that the thermodynamic equation (2.53) supplemented by (2.57)-(2.59) goes beyond previous forms of the planetary-scale heat budget of the MLT (Chandra, 1989; Lübken et al., 1993). In particular, the present heat budget consistently includes the dissipation of gravity wave kinetic energy, as well as two other potentially important processes that are usually ignored, namely the adiabatic conversion of mean enthalpy into gravity wave kinetic energy and the wave entropy flux convergence. In chapter 6 we will quantitatively assess these terms.

The dissipation of the mean flow is

$$\epsilon_m := \rho^{-1}\,(\,\boldsymbol{\Sigma}\,\nabla_3\,)\cdot\mathbf{v}\;. \tag{2.61}$$

Hence, in regions of gravity wave breaking, ϵ_m does not represent the total dissipation. The latter is $\epsilon_m + \epsilon_{igw}$, and this dissipative heating is implicitly accounted for by means of $E + \epsilon_m$.

Summarizing, the present formulation of the primitive equations includes the effects of small-scale turbulence and internal gravity waves in an energetically consistent way,

giving rise to the following energy conservation law (Becker and Schmitz, 2002):

$$\begin{aligned} &\partial_t \{ \rho (\mathbf{v}^2/2 + e) \} + \nabla_3 \cdot \{ \rho (\mathbf{v}^2/2 + e) \mathbf{v}_3 \} \\ &= c_p \rho Q - \rho g w + \nabla_3 \cdot \{ \Sigma \mathbf{v} - p \mathbf{v}_3 \} - \nabla_3 \cdot \mathbf{J} - \partial_z (F_p + \rho T F_s + \mathbf{F} \cdot \mathbf{v}) . \end{aligned} \tag{2.62}$$

Chapter 3

Momentum diffusion and dissipation for general circulation models

In any climate model, either global or mesoscale, one cannot calculate the *true* dissipation directly since this heating is ultimately due to molecular viscosity. Nonetheless, assuming quasi-stationary turbulence and that turbulent kinetic energy is mainly generated by the transfer of mean kinetic energy, the dissipative heating per unit mass is to a good approximation given by (2.33).[1] Hence, in any atmospheric circulation model that explicitly accounts for turbulent friction, the Reynolds stress tensor Σ must be parameterized. Then, the friction force per unit mass $\rho^{-1}\,\nabla_3\Sigma$ and the associated dissipation can be computed. Furthermore, two elementary constraints must be fulfilled. First, Σ must be symmetric, and second, the dissipation must be positive definite. As noted in the introduction, these constraints correspond to the Eulerian law of angular momentum conservation and the second law of thermodynamics.

In order to simulate the large-scale atmospheric flow using the primitive equations, one must account for both the enstrophy cascade in the free atmosphere and boundary layer mixing. If the mesosphere is included, also gravity wave-induced turbulent diffusion should be part of the Reynolds stress tensor. Generally we have to introduce an anisotropic turbulent viscosity, i.e. the horizontal diffusion coefficient K_h is usually much greater than the vertical one K_z (e.g., Pedlosky, 1987, section 4.2). As a result, the formulation of an appropriate stress tensor for global circulation models is not a trivial task. It was noted in Becker (2001) that conventional methods to formulate horizontal momentum diffusion violate the symmetry property of Σ. Since the friction force rather than the stress tensor is commonly parameterized, the frictional heating cannot even be defined. In the following we derive an anisotropic stress tensor that yields friction and dissipation forms suitable for the primitive equations.

[1] The shallow-atmosphere analogue of (2.33) is given by (2.61).

Assuming zero volume viscosity and disregarding vertical motions, the molecular stress tensor has the following anisotropic turbulent analogue:

$$\{\, \rho\, (\, K_h\, \nabla + K_z\, \mathbf{e}_z\, \partial_z\,)\circ \mathbf{v}\, \} + \{\, \ldots \}^T\,. \tag{3.1}$$

Here, ∇ is the horizontal gradient operator without the scale approximation (2.39), and the exponent ^{T} denotes the transposed. Using the derivatives of the unit vectors

$$\begin{aligned}
\partial_x \mathbf{e}_x &= \frac{\mathrm{tg}\,\phi}{r}\,\mathbf{e}_y - \frac{\mathbf{e}_z}{r}\,, \quad \partial_y \mathbf{e}_x = 0\,, \quad \partial_z \mathbf{e}_x = 0 \\
\partial_x \mathbf{e}_y &= -\frac{\mathrm{tg}\,\phi}{r}\,\mathbf{e}_x\,, \quad \partial_y \mathbf{e}_y = -\frac{\mathbf{e}_z}{r}\,, \quad \partial_z \mathbf{e}_y = 0 \\
\partial_x \mathbf{e}_z &= \frac{\mathbf{e}_x}{r}\,, \quad \partial_y \mathbf{e}_z = \frac{\mathbf{e}_y}{r}\,, \quad \partial_z \mathbf{e}_z = 0\,,
\end{aligned} \tag{3.2}$$

the stress tensor (3.1) can be expressed as

$$\begin{aligned}
\rho\, K_h\, \{\; & 2\, \mathbf{e}_x \circ \mathbf{e}_x\, (D - \partial_y v) + \mathbf{e}_x \circ \mathbf{e}_y\, (\xi + 2\, \partial_y u) - \mathbf{e}_x \circ \mathbf{e}_z\, u/r \\
& + \mathbf{e}_y \circ \mathbf{e}_x\, (\xi + 2\, \partial_y u) + 2\, \mathbf{e}_y \circ \mathbf{e}_y\, \partial_y v - \mathbf{e}_y \circ \mathbf{e}_z\, v/r \\
& - \mathbf{e}_z \circ \mathbf{e}_x\, u/r - \mathbf{e}_z \circ \mathbf{e}_y\, v/r\; \} \\
+\; \rho\, K_z\, \{\; & 2\, (\, \mathbf{e}_x \circ \mathbf{e}_z + \mathbf{e}_z \circ \mathbf{e}_x\,)\, \partial_z\, u + 2\, (\, \mathbf{e}_y \circ \mathbf{e}_z + \mathbf{e}_z \circ \mathbf{e}_y\,)\, \partial_z\, v\, \}\,.
\end{aligned} \tag{3.3}$$

As usual, the zonal and meridional velocity components are abbreviated as u and v. $D = \nabla\cdot\mathbf{v}$ denotes the horizontal divergence, and the relative vorticity $\xi = \mathbf{e}_z\cdot(\nabla\times\mathbf{v})$ is defined like in the previous section. The terms proportional to K_z are consistent with the familiar vertical momentum diffusion. The remainder, which is proportional to K_h, is meant to describe a mere scale-selective damping of the horizontal motion in order to balance the enstrophy cascade (and kinetic energy cascade as well) associated with atmospheric macro-turbulence. Hence, the stress proportional to K_h must vanish on any Eulerian sectional plane that is aligned horizontally. Stated otherwise, horizontal momentum diffusion must not drive a barotropic flow away from barotropy. Obviously, this elementary constraint is not fulfilled by (3.3) because of the geometric terms $-\rho\, K_h\, (\, \mathbf{v}\circ\mathbf{e}_z/r + \mathbf{e}_z/r\circ\mathbf{v}\,)$. Hence, a stress tensor appropriate for the primitive equations may be written as:

$$\boldsymbol{\Sigma} = \boldsymbol{\Sigma}_h + \boldsymbol{\Sigma}_z \tag{3.4}$$

$$\begin{aligned}
\boldsymbol{\Sigma}_h &= \rho\, K_h\, \Big(\, \{\, (\, \nabla + \mathbf{e}_z/r\,)\circ\mathbf{v}\,\} + \{\,\ldots\}^T\,\Big) \qquad (3.5)\\
&= \rho\, K_h\, \{\, 2\, \mathbf{e}_x \circ \mathbf{e}_x\, (D - \partial_y v) + \mathbf{e}_x \circ \mathbf{e}_y\, (\xi + 2\, \partial_y u) \\
&\qquad + \mathbf{e}_y \circ \mathbf{e}_x\, (\xi + 2\, \partial_y u) + 2\, \mathbf{e}_y \circ \mathbf{e}_y\, \partial_y v\, \}
\end{aligned}$$

$$\boldsymbol{\Sigma}_z = \rho\, K_z\, (\, \{\, \mathbf{e}_z\, \partial_z \circ \mathbf{v}\,\} + \{\,\ldots\}^T\,)\,. \tag{3.6}$$

The derivation of friction and dissipation from (3.5) and (3.6) requires some cumbersome analytical calculations as sketched in appendix B. The procedure is straightforward if we

take (3.2) and $\partial_x \partial_y = \partial_y \partial_x - (\mathrm{tg}\,\phi/r)\,\partial_x$ into account. We furthermore have to make use of the scaling assumptions (2.44) and (2.55). The resulting friction and dissipation forms owing to (3.5) and (3.6) are

$$\mathbf{H} := \rho^{-1}\,\nabla_3\,\Sigma_h \;=\; K_h\,\{\,\nabla^2\mathbf{v} + \nabla D \;+ 2\,\mathbf{v}/r^2\,\} \tag{3.7}$$

$$\mathbf{Z} := \rho^{-1}\,\nabla_3\,\Sigma_z \;=\; \rho^{-1}\,\partial_z\,(\,\rho\,K_z\,\partial_z\,\mathbf{v}\,) \tag{3.8}$$

and

$$\epsilon_h := \rho^{-1}\,(\Sigma_h \nabla_3\,)\cdot\mathbf{v} \;=\; K_h\,\{\,2(D-\partial_y v)^2 + 2(\partial_y v)^2 + (\xi + 2\,\partial_y u)^2\,\} \tag{3.9}$$

$$\epsilon_z := \rho^{-1}\,(\Sigma_z \nabla_3\,)\cdot\mathbf{v} \;=\; K_z\,(\,\partial_z\,\mathbf{v}\,)^2\,. \tag{3.10}$$

The vertical momentum diffusion (3.8) is standard. The associated dissipation (3.10) is well known (e.g., van Mieghem, 1973, section 9.2), though hardly being employed in present-day boundary layer or gravity wave schemes. The trace of Σ_z is zero while it is $2\,D$ for Σ_h. One may reformulate Σ_h such that its trace vanishes and normal components of turbulent stress are eliminated. This results in minor changes for the horizontal terms:

$$\Sigma_{h0} \;=\; \Sigma_h - D\,(\;\mathbf{e}_x \circ \mathbf{e}_x \;+\; \mathbf{e}_y \circ \mathbf{e}_y\;) \tag{3.11}$$

$$\mathbf{H}_0 \;=\; K_h\,\{\,\nabla^2\mathbf{v} + 2\,\mathbf{v}/r^2\,\} \tag{3.12}$$

$$\epsilon_{h0} \;=\; K_h\,\{\,(D - 2\partial_y v)^2 + (\xi + 2\,\partial_y u)^2\,\}\,. \tag{3.13}$$

Equations (3.12) and (3.13) can be used alternatively to (3.7) and (3.9). They may also be extracted from Smagorinsky (1993).

The horizontal friction forces (3.7) or (3.12) differ from the corresponding conventional form

$$\mathbf{H}_{c0} = \;K_h\,\nabla^2\,\mathbf{v}\,. \tag{3.14}$$

In this respect, $2\,K_h\mathbf{v}/r^2$ is the relevant term. This can be understood as follows. Let us consider the streamfunction and velocity field of an arbitrary superrotation with the maximum zonal velocity being a function of height z:

$$\psi_a := -u_a(z)\,r\sin\phi\;, \quad \mathbf{v}_a := u_a(z)\cos\phi\,\mathbf{e}_x\,. \tag{3.15}$$

(For $u_a(z) = \mathrm{const}$, (3.15) describes an ordinary superrotation, $u_a(z) \propto r/a_e$ yields a solid body rotation.) We can as well specify corresponding superrotations with their axes lying in the equatorial plane and pointing from $\lambda = 180^0$ to $\lambda = 0$,

$$\psi_b := -u_b(z)\,r\cos\phi\cos\lambda\;, \quad \mathbf{v}_b := -u_b(z)\,\{\,\sin\phi\cos\lambda\,\mathbf{e}_x - \sin\lambda\,\mathbf{e}_y\,\}\,, \tag{3.16}$$

or from $\lambda = 270^0$ to $\lambda = 90^0$,

$$\psi_c := -u_c(z)\,r\cos\phi\sin\lambda\;, \quad \mathbf{v}_c := -u_c(z)\,\{\,\sin\phi\sin\lambda\,\mathbf{e}_x \;+\; \cos\lambda\,\mathbf{e}_y\}\,. \tag{3.17}$$

Any superposition of (3.15)-(3.17) must be unaffected by horizontal diffusion since otherwise the angular momentum of the flow would change without a balancing surface drag. Now it is readily shown that

$$\nabla^2 \mathbf{v}_a = -2\,\mathbf{v}_a/r^2\,, \quad \nabla^2 \mathbf{v}_b = -2\,\mathbf{v}_b/r^2\,, \quad \text{and} \quad \nabla^2 \mathbf{v}_c = -2\,\mathbf{v}_c/r^2\,. \tag{3.18}$$

Hence, any superrotation is uniformely damped out by the conventional friction $K_h\,\nabla^2\,\mathbf{v}$ which therefore cannot be derived from a symmetric stress tensor. On the other hand, the friction forms (3.7) or (3.12) give no contribution as it should be. It is furthermore evident that the dissipation rates (3.9) or (3.13) vanish as well for any superposition of $\mathbf{v}_a$, $\mathbf{v}_b$, and $\mathbf{v}_c$ since we have $D = \partial_y v = 0$ and $\xi = -2\,\partial_y u$ in each case.

Spectral GCMs usually employ higher orders of horizontal diffusion. This is done to restrict the damping to the smallest resolved scales while leaving the planetary-scale flow almost unaffected. As described in Becker (2001, section 3b), the stress tensors (3.5) or (3.11) can easily be generalized to arbitrary orders. For instance, the biharmonic momentum diffusion yields

$$\text{conventional}: \quad \mathbf{H}_{c0}^{(bi)} = -r^2\,K_h\,\nabla^4\mathbf{v} \tag{3.19}$$

$$\text{symmetric}: \quad \mathbf{H}^{(bi)} = -r^2\,K_h\,\{\,\nabla^4\mathbf{v} + \nabla\,(\nabla\cdot\nabla^2\mathbf{v}\,) + 2\,\nabla^2\mathbf{v}/r^2\,\} \tag{3.20}$$

$$\mathbf{H}_0^{(bi)} = -r^2\,K_h\,\{\,\nabla^4\mathbf{v} + 2\,\nabla^2\mathbf{v}/r^2\,\}\,.$$

Both Eqs. (3.20) show that the correction to satisfy the Eulerian law of angular momentum conservation must have the form $-K_h\,2\,\nabla^2\mathbf{v}$ in the biharmonic case. This is quite different from the correction $K_h\,4\,\mathbf{v}/r^2$ which is used in the NCAR community climate model in order to simply conserve superrotations (see Kiehl et al., 1996, page 25).

Any horizontal momentum diffusion removes kinetic energy from the flow. However, even if the stress tensor is symmetric and the corresponding frictional heating can be defined, this does not necessarily ensure thermodynamic irreversibility, i.e. an increase of entropy due to frictional heating. For instance, in the biharmonic case the stress tensors corresponding to (3.5) and (3.11) can be written as

$$\boldsymbol{\Sigma}_h^{(bi)} = \rho\,K_h\,\left(\,\{\,(\,\nabla + \mathbf{e}_z/r\,)\circ\mathbf{v}^{(bi)}\,\} + \{\,\ldots\,\}^T\,\right) \tag{3.21}$$

$$\boldsymbol{\Sigma}_{h0}^{(bi)} = \boldsymbol{\Sigma}_h^{(bi)} - D^{(bi)}\,(\,\mathbf{e}_x\circ\mathbf{e}_x + \mathbf{e}_y\circ\mathbf{e}_y\,)\,, \tag{3.22}$$

where $\mathbf{v}^{(bi)} = u^{(bi)}\,\mathbf{e}_x + v^{(bi)}\,\mathbf{e}_y := -r^2\,\nabla^2\,\mathbf{v}$ and $D^{(bi)} := \nabla\cdot\mathbf{v}^{(bi)}$. The corresponding friction forms are given in (3.20). Using the abbreviation $\xi^{(bi)} = \mathbf{e}_z\cdot(\,\nabla\times\mathbf{v}^{(bi)}\,)$, the frictional heating rates are

$$\epsilon_h^{(bi)} = K_h \{ 2(D - \partial_y v) (D^{(bi)} - \partial_y v^{(bi)}) + 2 (\partial_y v) (\partial_y v^{(bi)}) + (\xi + 2 \partial_y u) (\xi^{(bi)} + 2 \partial_y u^{(bi)}) \} \tag{3.23}$$

$$\epsilon_{h0}^{(bi)} = K_h \{ (D - 2 \partial_y v) (D^{(bi)} - 2 \partial_y v^{(bi)}) + (\xi + 2 \partial_y u) (\xi^{(bi)} + 2 \partial_y u^{(bi)}) \} . \tag{3.24}$$

Similar expressions are obtained for any order of horizontal momentum diffusion higher than harmonic (Becker, 2001, section 3b). From (3.23) or (3.24) it is evident that in these cases the frictional heating is not positive definite. Therefore, higher orders are generally not consistent with the second law of thermodynamics. Accordingly, the numerical experiments presented in this study employ harmonic horizontal diffusion only.

Finally, in order to achieve consistence with the primitive equations as defined in the previous section, the scale approximation (2.39) is applied to the final forms for stress tensor, friction, and dissipation, that is, r is substituted by a_e. Note furthermore that, in the case of a divergent horizontal flow, horizontal momentum diffusion has a component in the vertical direction since

$$\nabla^2 \mathbf{v} = \mathbf{e}_x (\nabla^2 u - \frac{u}{a_e^2 \cos^2 \phi} - \frac{2 \operatorname{tg} \phi}{a_e} \partial_x v) + \mathbf{e}_y (\nabla^2 v - \frac{v}{a_e^2 \cos^2 \phi} + \frac{2 \operatorname{tg} \phi}{a_e} \partial_x u) - 2 \, \mathbf{e}_z \, \frac{D}{a_e} . \tag{3.25}$$

The corresponding vertical acceleration $-K_h \, 2 \, \mathbf{e}_z \, D/a_e$ is neglected by means of the hydrostatic approximation (2.51).

Chapter 4

Finite-difference representation of diffusion, dissipation, and gravity wave-mean flow interaction

The no-slip condition generally applies at fixed or solid boundaries of viscous fluids. The normal component of the no-slip condition, also known as the kinematic boundary condition, is trivial and generally accounted for by vertical discretization schemes used in atmospheric circulation models (see also appendixes A.1 and A.2). The motivation of this chapter is to translate the tangential component of the no-slip condition into its finite-difference analogue for application in GCMs or mesoscale atmospheric circulation models. Note that this boundary condition is usually ignored along with the frictional heating. We shall however show that, in addition to the flux-boundary conditions, the tangential component of the no-slip condition must be retained in order to account for the frictional heating in an energetically consistent way (Becker, 2003). Consequently, also the discretization of gravity wave effects must be formulated in line with the finite-difference forms for the boundary layer.

Another problem addressed in this chapter is the representation of horizontal diffusion and dissipation terms in a terrain-following vertical coordinate system. The point to be made is that the formulations given in the previous chapter can be applied in a hybrid coordinate system (Simmons and Burridge, 1981) as well, provided the horizontal diffusion coefficient is set equal zero in the lowermost model layers.

4.1 Vertical diffusion and gravity waves

Let us consider the sum of kinetic and internal energy of a fluid column. In the continuous case, vertical momentum diffusion and dissipation give rise to the following energy

generation rate:

$$\int_{z_s}^{\infty} \rho\, dz \,\{\, \mathbf{v} \cdot (\ \rho^{-1}\, \partial_z\, (\, \rho\, K_z\, \partial_z\, \mathbf{v}\,)\,) + K_z\, (\, \partial_z\, \mathbf{v}\,)^2\,\} = -\mathbf{v} \cdot (\, \rho\, K_z\, \partial_z\, \mathbf{v}\,)\Big|_{z=z_s} . \tag{4.1}$$

To evaluate the integral, the no-flux condition for $z \to \infty$ has been employed. The remaining term on the rhs of (4.1) is the work done by surface friction which vanishes according to the no-slip condition

$$\mathbf{v}\,|_{z=z_s} = 0\,, \tag{4.2}$$

where z_s denotes the topographic height.[1] The no-slip condition implies global balance between the rate of change of kinetic energy owing to friction and frictional heating (e.g., Lorenz, 1967; Pichler, 1986, chapter 9). If this constraint did not apply, surface friction would yield a significant contribution to the global energy budget of the atmosphere, and this would not be physically meaningful. Hence, for a given vertical discretization method that applies to the primitive equations, the finite-difference representation of vertical momentum diffusion and dissipation must be chosen in a way that the finite-difference form of (4.1) is zero by definition.

The angular momentum and energy conserving finite-difference scheme introduced by Simmons and Burridge (1981) has become a widely used method in present-day global circulation models (e.g., DKRZ, 1992; Kiehl at el., 1996). This scheme is also employed in the present simple GCM (see appendix A). For this type of models the finite-difference form of (4.1) may be written as

$$A \;=\; \sum_{l=1}^{lev} \frac{\Delta p_l}{g} \{\, \mathbf{v}_l \cdot \mathbf{Z}_l + \epsilon_{zl}\,\} \tag{4.3}$$

$$\begin{aligned} :=\; \sum_{l=1}^{lev} \frac{\Delta p_l}{g} \Big\{ & \frac{g}{\Delta p_l}\, \mathbf{v}_l \cdot \Big((\, \rho\, K_z\, \partial_z \mathbf{v}\,)_{l-\frac{1}{2}} - (\, \rho\, K_z\, \partial_z \mathbf{v}\,)_{l+\frac{1}{2}} \Big) \\ & + \frac{1}{2} \Big(\frac{p_l - p_{l-1}}{\Delta p_l\, \rho_{l-\frac{1}{2}}}\, (\, \partial_z \mathbf{v}\,)_{l-\frac{1}{2}} \cdot (\, \rho\, K_z\, \partial_z \mathbf{v}\,)_{l-\frac{1}{2}} \\ & \quad + \frac{p_{l+1} - p_l}{\Delta p_l\, \rho_{l+\frac{1}{2}}}\, (\, \partial_z \mathbf{v}\,)_{l+\frac{1}{2}} \cdot (\, \rho\, K_z\, \partial_z \mathbf{v}\,)_{l+\frac{1}{2}} \Big) \Big\}\,. \end{aligned} \tag{4.4}$$

Here, lev is the total number of full model layers, and $\Delta p_l := p_{l+1/2} - p_{l-1/2}$ is the pressure increment between intermediate half model layer. The discretization of momentum diffusion $\mathbf{Z}_l$ is straightforward. The corresponding dissipation rate ϵ_{zl} on a full model layer l is defined as the approximate average of the dissipation rates at adjacent half

[1] The familiar kinematic boundary condition $w = \mathbf{v} \cdot \nabla z_s$ applies in the inviscid case only and is ruled out at the lower edge of the friction layer. Note also that (4.2) is not exactly valid over the sea since the atmosphere exerts a significant amount of work on the ocean. However, this work is negligible in the energy budget of the atmosphere.

layers. Weighting these contributions with appropriate pressure differences is essential for further simplification of (4.4). First we make use of the dynamic boundary conditions

$$(\,\rho\,K_z\,\partial_z\,\mathbf{v}\,)_{\frac{1}{2}} \;=\; 0 \tag{4.5}$$

$$(\,\rho\,K_z\,\partial_z\,\mathbf{v}\,)_{lev+\frac{1}{2}} \;=\; C\,\rho_{lev}\,\mathbf{v}_{lev}\,, \tag{4.6}$$

where C is a surface coefficient (see appendix A.3). Then A can be expressed as

$$\begin{aligned} A \;=\; & \sum_{l=2}^{lev}\Big\{\,\mathbf{v}_l\cdot(\,\rho\,K_z\,\partial_z\mathbf{v}\,)_{l-\frac{1}{2}} + \frac{1}{2}\,\frac{p_l-p_{l-1}}{g\,\rho_{l-\frac{1}{2}}}\,(\,\partial_z\mathbf{v}\,)_{l-\frac{1}{2}}\cdot(\,\rho\,K_z\,\partial_z\mathbf{v}\,)_{l-\frac{1}{2}}\Big\} \\ + \; & \sum_{l=1}^{lev-1}\Big\{\,-\mathbf{v}_l\cdot(\,\rho\,K_z\,\partial_z\mathbf{v}\,)_{l+\frac{1}{2}} + \frac{1}{2}\,\frac{p_{l+1}-p_l}{g\,\rho_{l+\frac{1}{2}}}\,(\,\partial_z\mathbf{v}\,)_{l+\frac{1}{2}}\cdot(\,\rho\,K_z\,\partial_z\mathbf{v}\,)_{l+\frac{1}{2}}\Big\} \\ - \; & C\,\rho_{lev}\,\mathbf{v}_{lev}^2 + \frac{1}{2}\left[\frac{(p_{l+1}-p_l)}{g\,\rho_{l+\frac{1}{2}}}\,(\,\partial_z\,\mathbf{v}\,)_{l+\frac{1}{2}}\right]_{l=lev}\cdot\;C\,\rho_{lev}\,\mathbf{v}_{lev}\,. \end{aligned} \tag{4.7}$$

Defining the half level wind shear as

$$(\,\partial_z\,\mathbf{v}\,)_{l+\frac{1}{2}} = -g\,\rho_{l+\frac{1}{2}}\,(\mathbf{v}_{l+1}-\mathbf{v}_l\,)\,(\,p_{l+1}-p_l\,)^{-1} \quad \text{for} \quad l=1\ldots lev-1\,, \tag{4.8}$$

Eq. (4.7) reduces to

$$\begin{aligned} A \;=\; & \sum_{l=2}^{lev}\frac{1}{2}(\,\mathbf{v}_l+\mathbf{v}_{l-1}\,)\cdot(\,\rho\,K_z\,\partial_z\mathbf{v}\,)_{l-\frac{1}{2}} \;+\; \sum_{l=1}^{lev-1}\frac{1}{2}(\,-\mathbf{v}_l-\mathbf{v}_{l+1}\,)\cdot(\,\rho\,K_z\,\partial_z\mathbf{v}\,)_{l+\frac{1}{2}} \\ & -C\,\rho_{lev}\,\mathbf{v}_{lev}^2 + \frac{1}{2}\left[\frac{(p_{l+1}-p_l)}{g\,\rho_{l+\frac{1}{2}}}\,(\,\partial_z\,\mathbf{v}\,)_{l+\frac{1}{2}}\right]_{l=lev}\cdot\;C\,\rho_{lev}\,\mathbf{v}_{lev} \\ A \;=\; & -C\,\rho_{lev}\,\mathbf{v}_{lev}^2 \;+\; \frac{1}{2}\left[\frac{(p_{l+1}-p_l)}{g\,\rho_{l+\frac{1}{2}}}\,(\,\partial_z\,\mathbf{v}\,)_{l+\frac{1}{2}}\right]_{l=lev}\cdot\;C\,\rho_{lev}\,\mathbf{v}_{lev}\,. \end{aligned} \tag{4.9}$$

The rhs of Eq. (4.9) is the finite-difference form of the work done by surface friction. It vanishes by definition if we specify the term in brackets as

$$\left[\frac{(p_{l+1}-p_l)}{g\,\rho_{l+\frac{1}{2}}}\,(\partial_z\mathbf{v})_{l+\frac{1}{2}}\right]_{l=lev} := 2\,\mathbf{v}_{lev} \tag{4.10}$$

which is the finite-difference analogue of the no-slip condition (4.2). An intuitive interpretation of (4.10) is that a velocity profile, linear in z and formally extrapolated in the ground, intersects the surface with $\mathbf{v}=0$.

Summarizing, a model's energy source owing to vertical momentum diffusion and dissipation is zero by definition if we let

$$\mathbf{Z}_l = \frac{-g}{\Delta p_l}\begin{cases} (\,\rho\,K_z\,\partial_z\mathbf{v}\,)_{l+\frac{1}{2}} & l=1 \\ (\,\rho\,K_z\,\partial_z\mathbf{v}\,)_{l+\frac{1}{2}} - (\,\rho\,K_z\,\partial_z\mathbf{v}\,)_{l-\frac{1}{2}} & l=2\ldots lev-1 \\ C\,\rho_l\,\mathbf{v}_l - (\,\rho\,K_z\,\partial_z\mathbf{v}\,)_{l-\frac{1}{2}} & l=lev \end{cases} \tag{4.11}$$

$$\epsilon_{zl} = \frac{1}{2\,\Delta p_l} \begin{cases} (\,\rho\,K_z\,\partial_z \mathbf{v}\,)_{l+\frac{1}{2}} \cdot (\,\partial_z \mathbf{v}\,)_{l+\frac{1}{2}} (p_{l+1} - p_l\,)/\rho_{l+\frac{1}{2}} & l = 1 \\ (\,\rho\,K_z\,\partial_z \mathbf{v}\,)_{l-\frac{1}{2}} \cdot (\,\partial_z \mathbf{v}\,)_{l-\frac{1}{2}} (p_l - p_{l-1}\,)/\rho_{l-\frac{1}{2}} & l = 2 \ldots lev-1 \\ \quad + (\,\rho\,K_z\,\partial_z \mathbf{v}\,)_{l+\frac{1}{2}} \cdot (\,\partial_z \mathbf{v}\,)_{l+\frac{1}{2}} (p_{l+1} - p_l\,)/\rho_{l+\frac{1}{2}} & \\ (\,\rho\,K_z\,\partial_z \mathbf{v}\,)_{l-\frac{1}{2}} \cdot (\,\partial_z \mathbf{v}\,)_{l-\frac{1}{2}} (p_l - p_{l-1}\,)/\rho_{l-\frac{1}{2}} & l = lev \\ \quad + 2\,g\,C\,\rho_l\,\mathbf{v}_l^2 & \end{cases} \tag{4.12}$$

and take the definition (4.8) into account.

The no-slip condition (4.10) is required to specify the frictional heating in the lowermost full model layer $l = lev$ (last term on the rhs of the third Eq. (4.12)). It thus defines the contribution from the Prandtl layer. With the usual definition of the surface coefficient, $C = C_D\,|\mathbf{v}_{lev}|$, this Prandtl layer frictional heating is proportional to $C_D\,|\mathbf{v}_{lev}|^3$. Such a relation also follows from multiplying the Prandtl layer stress with the corresponding wind shear, assuming that both are constant with height in the Prandtl layer. A corresponding formulation has been used by Bister and Emanuel (1998, see Eq. (6) in their paper). On the other hand, the present finite-difference formulation does not invoke any assumption about the velocity profile in the Prandtl layer (which is typically logarithmic) nor in the underlying viscous layer.

Specifying the discretization of vertical diffusion of potential temperature (second term on the rhs of (2.56)) in an energy conserving way is generally an easy task. For the model calculations presented in the following chapters, the definition

$$\mu_{z\,l} = \frac{-g}{\Delta p_l} \{\, (\,\rho\,K_z\,\frac{T}{\Theta}\,\partial_z\,\Theta\,)_{l+\frac{1}{2}} - (\,\rho\,K_z\,\frac{T}{\Theta}\,\partial_z\,\Theta\,)_{l-\frac{1}{2}} \,\} \quad \text{for} \quad l = 1 \ldots lev \tag{4.13}$$

is used along with the dynamic boundary conditions

$$(\,\rho\,K_z\,\frac{T}{\Theta}\,\partial_z\,\Theta\,)_{\frac{1}{2}} = 0 \tag{4.14}$$

$$(\,\rho\,K_z\,\frac{T}{\Theta}\,\partial_z\,\Theta\,)_{lev+\frac{1}{2}} = C\,\rho_{lev}\,(\,\Theta_{lev} - \Theta_s\,)\,. \tag{4.15}$$

Here, Θ_s is a surface potential temperature which is related to the surface temperature T_s via $\Theta_s = T_s\,(\,p_{00}/p_s\,)^{R/c_p}$, and p_s is the surface pressure. The net energy input due to vertical diffusion of momentum and potential temperature results from the surface sensible heat flux, as it should be:

$$\sum_{l=1}^{lev} \frac{\Delta p_l}{g} \{\, \mathbf{v}_l \cdot \mathbf{Z}_l + \epsilon_{zl} + \mu_{z\,l} \,\} = -C\,\rho_{lev}\,(\,\Theta_{lev} - \Theta_s\,)\,. \tag{4.16}$$

The proposed differencing scheme can easily be generalized to account for gravity wave effects. To achieve this we have to include the turbulent diffusion coefficient owing

to gravity wave breakdown, $K_{z\,igw}$ (see section 6.2), in the definition of K_z. With regard to vertical diffusion of potential temperature, $K_{z\,igw}$ is scaled by an additional Prandtl number. In this context we anticipate the following result derived in section 6.1 on the basis of Lindzen's saturations hypothesis: The gravity wave entropy flux convergence is formally equal to a wave-induced vertical diffusion of mean potential temperature with a Prandtl number of 2. Accordingly, we incorporate also the gravity wave entropy flux in the vertical diffusion term (4.13). As a result, the effective Prandtl number must not exceed a value of 2. In the control simulation presented in chapter 6, the IGW-associated effective Prandtl number is set equal 1.

To further account for gravity wave effects, we have to include the tendencies owing to the nondiffusive gravity wave fluxes of horizontal momentum and pressure (see section 2.4). The discretization of these tendencies is analogous to (4.11)-(4.13) and yields with regard to the dynamic boundary conditions

$$\mathbf{F}_{1/2} = \mathbf{F}_{lev+1/2} = 0 \quad \text{and} \quad F_{p\,1/2} = F_{p\,lev+1/2} = 0 \tag{4.17}$$

the following expressions for momentum deposition, residual work, and energy deposition:

$$(\,-\rho^{-1}\,\partial_z\,\mathbf{F}\,)_l \;=\; \frac{g}{\Delta p_l}\begin{cases} \mathbf{F}_{l+\frac{1}{2}} & l=1 \\ \mathbf{F}_{l+\frac{1}{2}} - \mathbf{F}_{l-\frac{1}{2}} & l=2\ldots lev-1 \\ -\mathbf{F}_{l-\frac{1}{2}} & l=lev \end{cases} \tag{4.18}$$

$$W_{res\,l} \;=\; \frac{-1}{2\,\Delta p_l}\begin{cases} \mathbf{F}_{l+\frac{1}{2}}\cdot(\,\partial_z\mathbf{v}\,)_{l+\frac{1}{2}}(\,p_{l+1}-p_l\,)/\rho_{l+\frac{1}{2}} & l=1 \\ \mathbf{F}_{l-\frac{1}{2}}\cdot(\,\partial_z\mathbf{v}\,)_{l-\frac{1}{2}}(\,p_l-p_{l-1}\,)/\rho_{l-\frac{1}{2}} & \\ \quad +\mathbf{F}_{l+\frac{1}{2}}\cdot(\,\partial_z\mathbf{v}\,)_{l+\frac{1}{2}}(\,p_{l+1}-p_l\,)/\rho_{l+\frac{1}{2}} & l=2\ldots lev-1 \\ \mathbf{F}_{l-\frac{1}{2}}\cdot(\,\partial_z\mathbf{v}\,)_{l-\frac{1}{2}}(\,p_l-p_{l-1}\,)/\rho_{l-\frac{1}{2}} & l=lev \end{cases} \tag{4.19}$$

$$E_l \;=\; W_{res\,l} \;+\; \frac{g}{\Delta p_l}\begin{cases} F_{p\,l+\frac{1}{2}} & l=1 \\ F_{p\,l+\frac{1}{2}} - F_{p\,l-\frac{1}{2}} & l=2\ldots lev-1 \\ -F_{p\,l-\frac{1}{2}} & l=lev\ . \end{cases} \tag{4.20}$$

Consequently, the nondiffusive gravity wave-mean flow interaction terms give rise to

$$\sum_{l=1}^{lev}\frac{\Delta p_l}{g}\,\{\,\mathbf{v}_l\cdot(\,-\rho^{-1}\,\partial_z\,\mathbf{F}\,)_l + E_l\,\} = 0 \tag{4.21}$$

such that internal wave fluxes do not affect the total energy.

4.2 Constraints on horizontal diffusion terms

In a spectral model, the horizontal diffusion and dissipation terms (3.7) and (3.9) or (3.12) and (3.13), as well as the first term on the rhs of (2.56) can be computed with

machine accuracy. Disregarding aliasing errors, their numerical representation deserves no further analysis. However, these horizontal terms have been defined in the z-coordinate system, and an exact analytical transformation into the hybrid coordinate system seems to be impossible. Alternatively, we may apply (3.7) and (3.9) or (3.12) and (3.13), and the conventional horizontal diffusion of temperature directly on hybrid surfaces, provided these surfaces are sufficiently flat. That is, for any flow variable X the approximation

$$\nabla_z X = \nabla_\eta X \; - \; \frac{\partial X}{\partial z} \, (\nabla_\eta z) \approx \nabla_\eta X \tag{4.22}$$

or equivalently

$$| L \nabla_\eta z | \; << \; H \tag{4.23}$$

must be valid. Here, ∇_z or ∇_η denote the horizontal gradient operator applied on surfaces of constant height z or constant hybrid coordinate η. For terrain-following surfaces close to the lower boundary, the condition (4.23) may be violated. For instance, in the vicinity of the Himalayas we have $| L \nabla_\eta z_s | \sim H$. Therefore, only if η-surfaces do gradually change from terrain-following surfaces near the ground to surfaces of constant pressure in the middle troposphere, can we assume that (4.23) is valid around that level and farther above. In the global circulation model used in the following chapters, such a behavior of the hybrid coordinate is achieved using Eqs. (A1)-(A3) (see appendix A.1). Figure 1 shows the corresponding behavior of some representative hybrid surfaces (solid lines) in presence of a mountain range with a maximum elevation of about 3.5 km. In this figure we have assumed an atmosphere at rest with $T = T_{ref}(p)$, where the reference temperature T_{ref} is given by Fig. 32a (see appendix A.2). The thin lines in Fig. 1 indicate the sigma surfaces that correspond to the hybrid surfaces. It is obvious that in the sigma-coordinate system the condition (4.23) is generally not valid because every model layer follows the orographic elevations. The same holds if the log-pressure coordinate is used (not shown). For the present global circulation model it will be shown that setting $K_h = 0$ below $\eta = 0.8$ and assuming a smooth increase between $\eta = 0.8$ and 0.6 (Figs. 5c, 18c) is sufficient to ensure satisfactory angular momentum and energy budgets. This approach may furthermore be justified by the fact that the enstrophy cascade is not relevant in the lower troposphere.

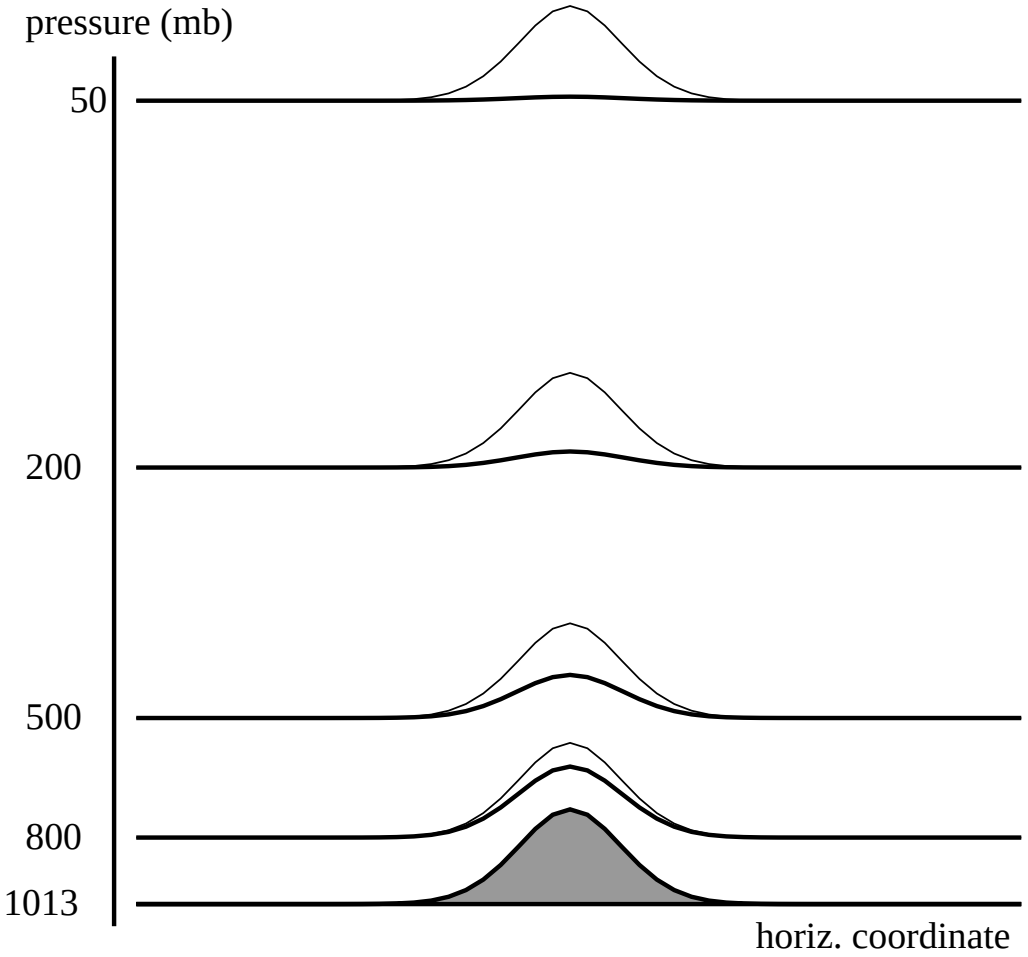

Figure 1: Surfaces of constant hybrid coordinate (solid lines) and constant sigma coordinate (thin lines) in the presence of a major mountain range (shaded) and for assuming $T = T_{ref}(p)$.

Chapter 5

Numerical experiments without internal gravity waves

This chapter presents some numerical experiments in order to test the diffusion and dissipation forms proposed in the previous chapters against the corresponding conventional methods. Our specific focus is on the global energy budget of the troposphere. We start by analysing the life cycle of a baroclinic wave in a thermally and mechanically isolated atmosphere (section 5.1). Comparatively realistic simulations of the boreal winter climate are investigated in section 5.2. We utilize the *Kühlungsborn Mechanistic general Cirulation Model (KMCM)* developed by the author. The relevant characteristics of this model are mentioned in the text, while further details can be found in appendix A.

5.1 Adiabatic baroclinic life cycle

Let us reevaluate the life cycle of a baroclinic wave originally investigated by Simmons and Hoskins (1978). We use *KMCM* with a T54 spectral resolution and 40 equally spaced hybrid levels. Orography and all so-called physical parameterizations are switched off, except for horizontal momentum diffusion. A globally constant horizontal diffusion coefficient of $K_h = 2.5 \times 10^5$ m^{2}s^{-1} is used. This corresponds to a damping time constant of about 0.6 days for wave number 54 of relative vorticity. We consider two simulations. In the *conventional* run, horizontal momentum diffusion is accounted for owing to (3.14), and the dissipation is accordingly ignored. The *control* run employs (3.7) together with the associated frictional heating rate (3.9).

The initial condition is a thermally balanced zonal flow superposed with a small perturbation of the most unstable normal mode of zonal wave number $m = 6$. The thermally balanced zonal flow is shown in Figs. 2a,d. It consists of a temperature field $T_E(\phi, p)$ and a corresponding zonal wind $u_E(\phi, p)$ such that T_E and u_E obey the nonlinear thermal

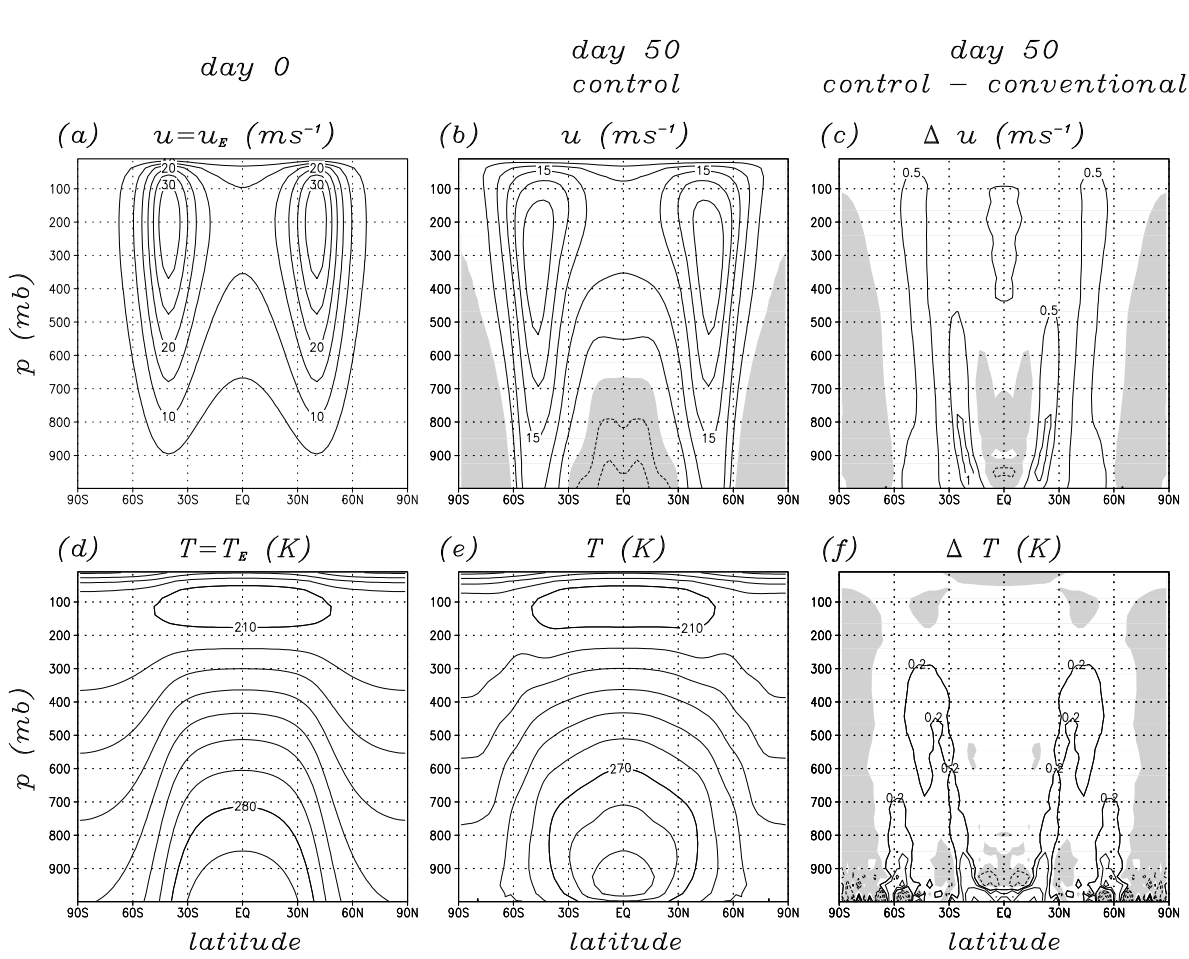

Figure 2: (a),(d) Zonal-mean zonal wind and temperature at day 0 of the baroclinic life cycle experiment. (b),(e) Same as (a),(d) but for day 50 of the control simulation. (c),(f) Differences at day 50 in the control run from the conventional run. Contour intervals are (a),(b) 5 ms^{-1}, (c) 0.5 ms^{-1}, (d),(e) 10 K, and (f) 0.2 K. Zero contours are not drawn, and negative values are shaded.

wind relation

$$\partial_p \{ f\, u_E + \frac{\mathrm{tg}\ \phi}{a_e}\, u_E^2 \} = \frac{R}{p}\, \frac{\partial_\Phi\, T_E}{a_e}\,. \tag{5.1}$$

From (5.1) follows that T_E must be symmetric about the equator near the equator. In the present experiment, T_E and u_E are completely symmetric about the equator. T_E is specified analytically (see Becker et al., 1997, appendix), and u_E is computed by vertical integration of (5.1) with respect to the boundary condition $u_E = 0$ for $p_s = p_{00} = 1013$ mb. Even though (T_E, u_E) exhibits baroclinic instability, it is conserved by the model as long as wave perturbations are absent. In the following we consider the temporal evolution of a baroclinic wave that is excited by the aforementioned normal mode initialization.

Figure 3 shows available potential energy of the zonal-mean flow and the eddies, AZ

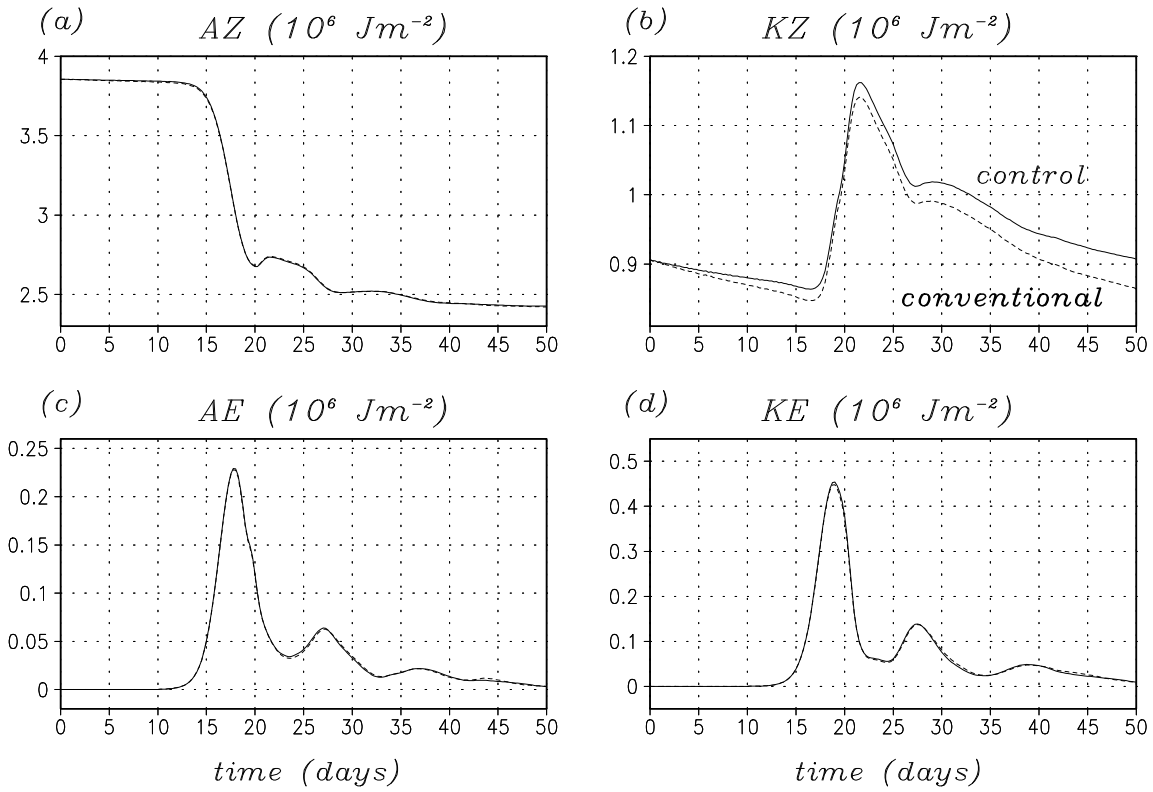

Figure 3: Available potential energy and kinetic energy of the zonal-mean flow (AZ and KZ) and of the eddies (AE and KE) in the baroclinic life cycle experiments (control: solid lines, conventional: dashed lines).

and AE as defined by Lorenz (1955), along with the corresponding kinetic energies KZ and KE. The prominent growth and decay of a baroclinic wave is evident in both simulations. Differences are quantitatively negligible when considering AZ, AE, and KE. The behavior of KZ is only qualitatively similar in both runs. The difference indicates a weaker zonal circulation in the conventional run.

The zonally averaged zonal wind and temperature at day 50 look similar in both simulation. Figures 2b,e show these fields for the control run. The differences in the control run from the conventional run are shown in Figs. 2c,f. These signals indicate a stronger relative angular momentum and a higher internal energy in the control run. The importance of these differences can be acknowledged by considering the temporal evolutions of total potential energy TP, total kinetic energy TK, relative angular momentum L_r, and Ω-angular momentum L_0 per unit area:

$$TP \;:=\; (4\,\pi\,a_e^2)^{-1} \int\limits_{atmos} dV\;\rho\,(c_v\,T + g\,z\,) \;=\; (4\,\pi\,a_e^2)^{-1} \int\limits_{atmos} dV\;\rho\,c_p\,T \qquad (5.2)$$

$$TK := (4\pi a_e^2)^{-1} \int\limits_{atmos} dV\, \rho \frac{\mathbf{v}^2}{2} \tag{5.3}$$

$$L_r := (4\pi a_e^2)^{-1} \int\limits_{atmos} dV\, \rho\, u\, a_e \cos\phi \tag{5.4}$$

$$L_0 := (4\pi a_e^2)^{-1} \int\limits_{atmos} dV\, \rho\, \Omega\, a_e^2 \cos^2\phi\,. \tag{5.5}$$

The integrals extend over the whole model atmosphere. The numerical representation of (5.2)-(5.5) is straightforward. Total energy $TP + TK$ and total angular momentum $L_r + L_0$ should be conserved quantities in the life cycle experiments. Figure 4 shows (5.2)-(5.5), as well as total energy and total angular momentum as functions of time for both simulations. In $\Delta\, TP$ and $\Delta\, L_0$, the total potential energy and the Ω-angular momentum of the initial state are subtracted. Total kinetic energy, as well as relative and Ω-angular momentum behave qualitatively similar in both simulations. However, total energy and total angular momentum are conserved in the control run only. There is a continuous spurious loss of total angular momentum in the conventional case. At day 50, this loss amounts to about 5-10% of the overall relative angular momentum. A worse shortcoming is due to a substantial loss of total energy. Within a couple of days around the life cycle maximum, this loss is of the same magnitude as the overall kinetic energy of the model atmosphere. This result may be interpreted as follows.

During the phase of baroclinic instability (day 0-17), total kinetic energy grows at the cost of available potential energy due to adiabatic conversion. To a first approximation this growth can be considered as a thermodynamically reversible process. Stated otherwise, during the phase of linear baroclinic instability the enstrophy cascade and horizontal momentum diffusion are not very effective.[1] From about day 20 on, kinetic energy is lost while available potential energy does not increase again. Hence, the decay phase of a baroclinic life cycle is strongly irreversible due to the downscaling of enstrophy (and kinetic energy as well) and the action of horizontal diffusion. Bound up with this, there must be some diabatic heating to balance the frictional loss of kinetic energy. Only a symmetric stress tensor formulation of horizontal momentum diffusion completed by the proper dissipation accounts for the corresponding generation of nonavailable potential energy

$$TP - (AZ + AE)$$

in a physically reasonable way.

[1] In the control run, there is a notably frictional heating even during the grow phase. As a result, the decline of $AZ + AE$ is stronger than the decline of TP.

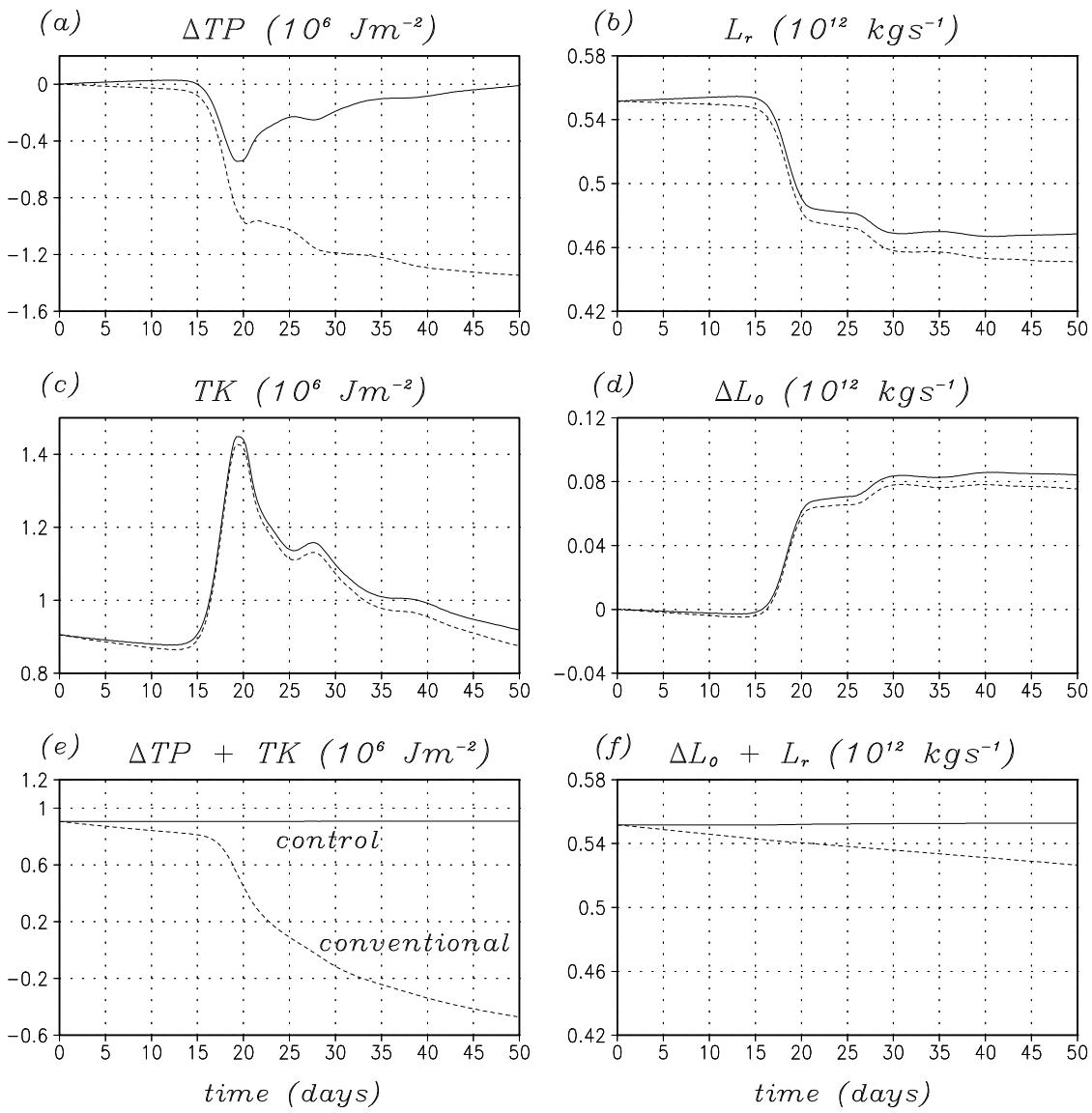

Figure 4: Temporal behavior of global energy and angular momentum quantities in the life cycle experiments (control: solid lines, conventional: dashed lines).

5.2 Perpetual January simulations

In the previous section we have considered an instructive but nevertheless academic example where neither thermal nor mechanical forcing of the model atmosphere was present. In the following we apply the proposed friction and dissipations forms under more realistic conditions, namely in perpetual January simulations of the troposphere and stratosphere. Even though our specifications of radiative and latent heating are quite simple, the thermal and mechanical forcing of the model atmosphere is quantitatively realistic, giving rise

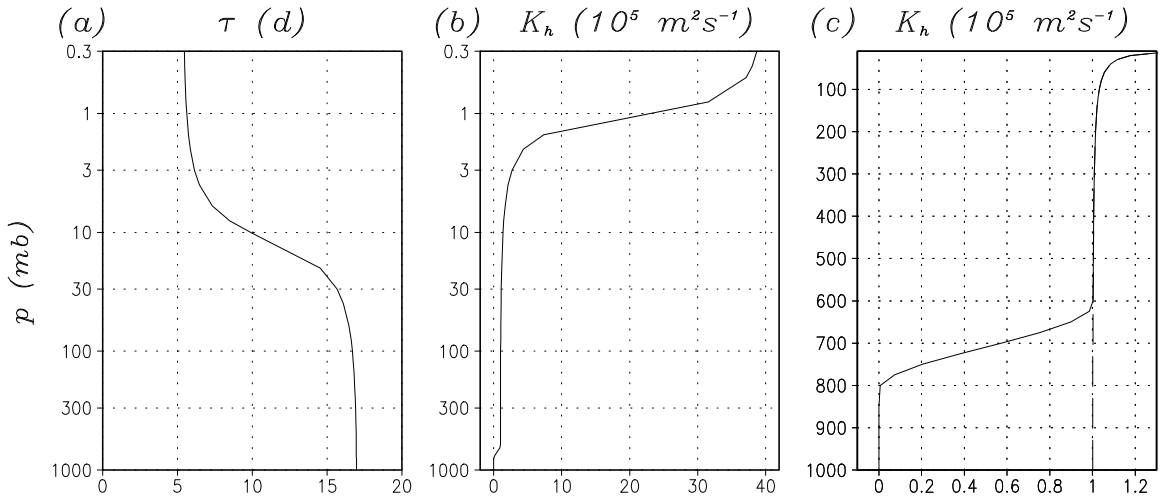

Figure 5: (a) Relaxation time τ and (b) standard horizontal diffusion coefficient K_h as functions of $\eta \times 1013$ mb for the T42/L24 model configuration. Both profiles are calculated as continuous functions of η. The extra panel (c) shows the tropospheric and lower stratospheric branch of the standard K_h (solid line). The dashed line in panel (c) shows a K_h-profile that is finite in the lower troposphere and identical to the standard profile otherwise.

to a comparatively realistic simulation of the boreal winter climate. The spatial resolution is spectral truncation at total wavenumber 42 and 24 unequally spaced hybrid levels from 990 to 0.3 mb. This resolution is abbreviated as T42/L24.

5.2.1 Model description

Compared to comprehensive GCMs, the key idealization in the present model *KMCM* is that we treat only the flow of dry air. Following Lorenz (1967, chapter V), the thermal forcing of the model atmosphere consists of the bulk heating Q which is due to radiation and condensation, plus the surface sensible heat flux. Radiative and latent heating are accounted for by simple parameterizations, namely by temperature relaxation towards an equilibrium temperature $T_E(\phi, p)$ and prescribed cumulus heating $Q_c(\lambda, \phi, p)$ in the deep tropics (Hou, 1993) together with self-induced condensational heating in the middle latitudes using a heating function $Q_m(\lambda, \phi, p)$ (Mak, 1994). Written in terms of sensible heat divided by c_p the bulk heating yields

$$Q = -\frac{T - T_E}{\tau} + Q_c + \frac{|\omega|\, h(-\omega)}{40 \text{ mb d}^{-1}}\, Q_m \,, \tag{5.6}$$

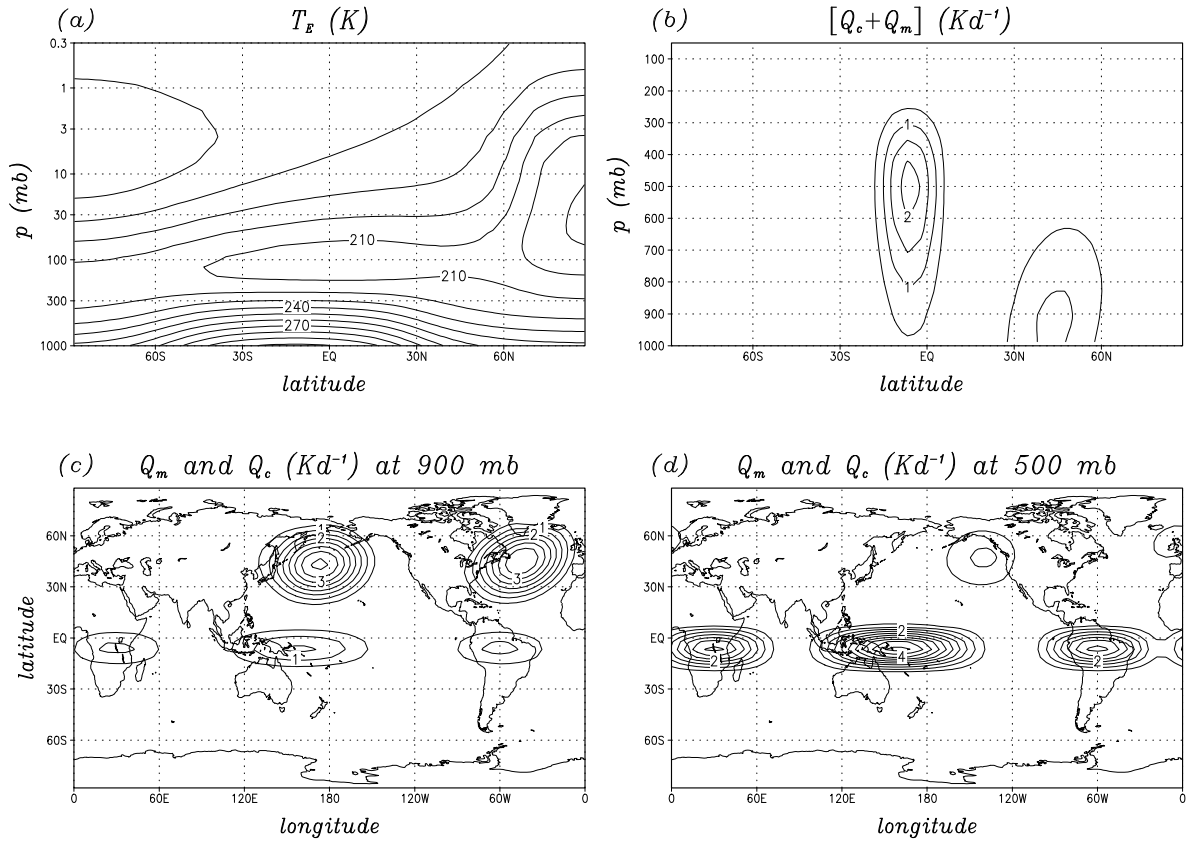

Figure 6: (a) Equilibrium temperature in the T42/L24 version of *KMCM* (contour interval 10 K). (b) Zonal means of the heating functions Q_c and Q_m (contour interval 0.5 K/d). (c)-(d) Longitude-dependencies of the heating functions Q_c and Q_m at 900 and 500 mb. Contours are from 0.5 to 5 K/d in intervals of 0.5 K/d.

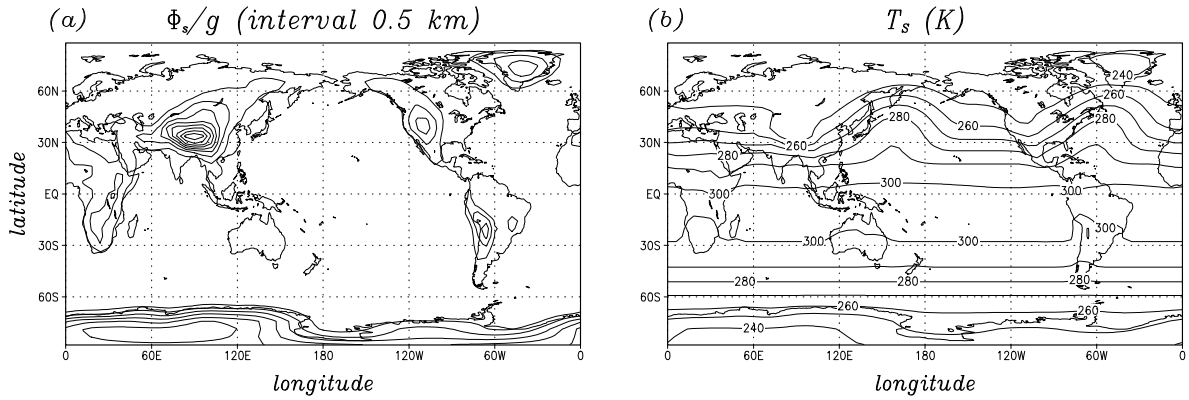

Figure 7: (a) Model topography Φ_s/g. Contours are from 0.5 to 4 km in intervals of 0.5 km. The Himalayas and the Rockies reach maximum elevations of about 4.4 and 1.8 km, respectively. (b) Model surface temperature according to Eq. (5.7) (contour interval 10 K).

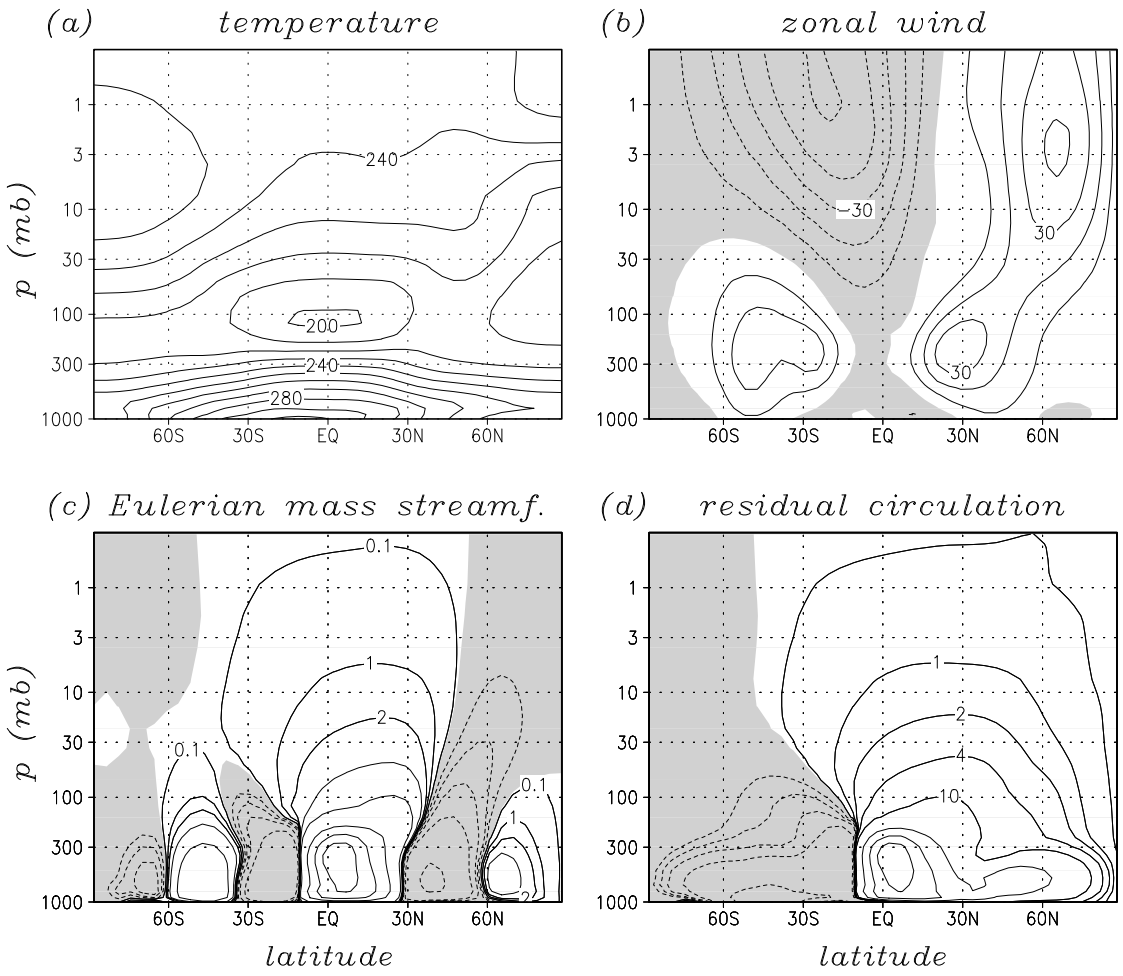

Figure 8: Zonal-mean climatology of the T42/L24 version of *KMCM*. (a) Temperature (contour interval 10 K). (b) Zonal wind (contour interval 10 ms^{-1}). (c) Eulerian mass streamfunction (contours $0.1, \pm 1, \pm 2, \pm 4, \pm 10, \pm 50, 100, 150 \times 10^9$ kgs^{-1}). (d) Same as (c), but for the residual mass streamfunction. Zero contours are not drawn, and negative values are shaded.

where ω is the pressure velocity and h denotes the Heaviside-function. The relaxation time τ is about 17 days in the lower troposphere and slopes down to 5 days in the upper stratosphere (Fig. 5a). The surface sensible heat flux is due to the boundary condition (4.15) using

$$T_s := [\, T_E + 0.4\, \tau\, (\, Q_c + Q_m\,)\,]_{p=p_s}\,. \tag{5.7}$$

The fields T_E, Q_c, and Q_m have been adjusted to mimic perpetual January conditions. Figure 6a shows the equilibrium temperature that is used in the present T42/L24 model version with the uppermost model layer at about 0.3 mb. The heating functions are depicted in Figs. 6b-d. Figure 7 shows the model topography together with the surface

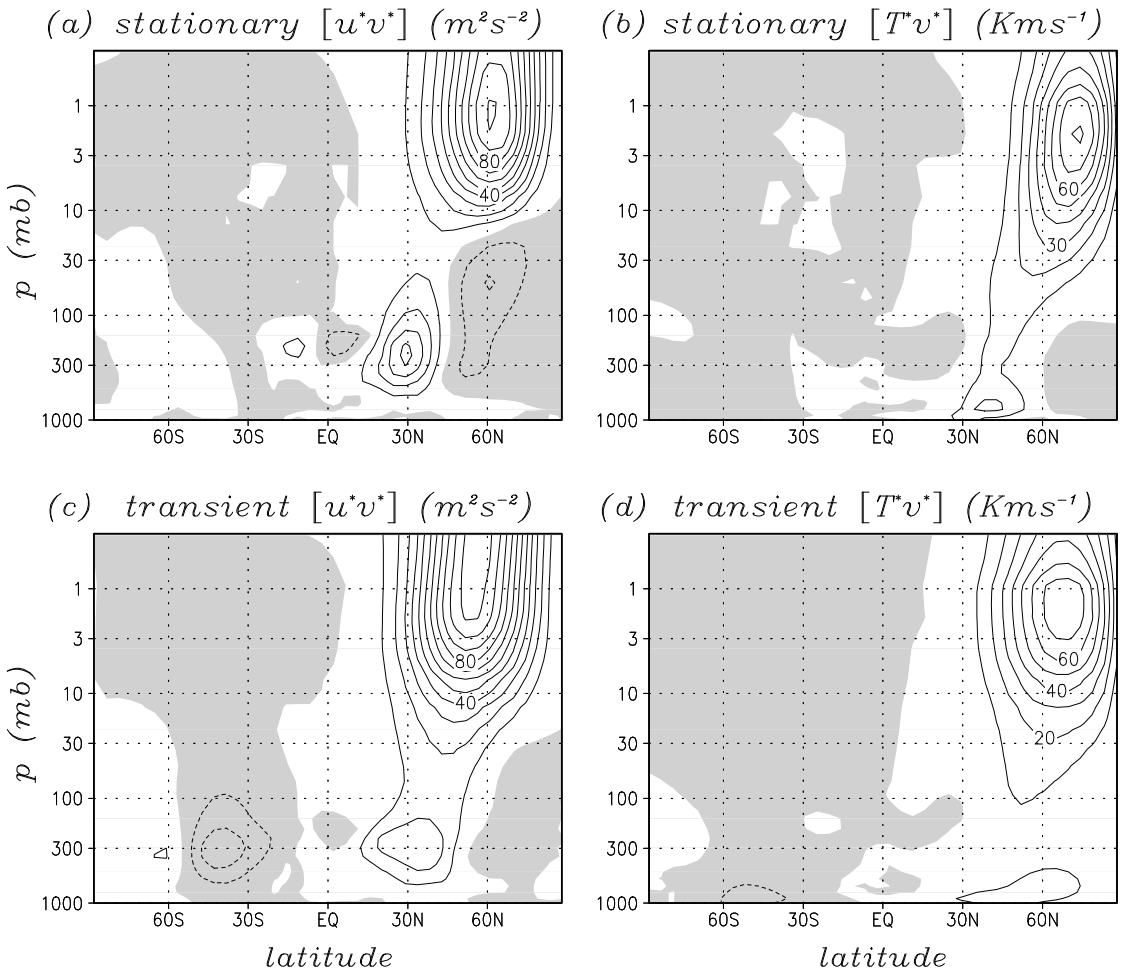

Figure 9: Zonal-mean climatology of the T42/L24 version of *KMCM*. (a) Stationary eddy momentum flux (contour interval 10 m^2s^{-2}). (b) Stationary eddy heat flux (contour interval 10 Kms^{-1}). (c),(d) Same as (a),(b) but for the transient wave fluxes. Zero contours are not drawn, and negative values are shaded.

temperature (5.7).

The assumed scale-selective damping owing to horizontal momentum diffusion is such that, in the upper troposphere, wave number 42 of relative vorticity has a damping time constant of about 2.6 days which corresponds to $K_h \sim 1 \times 10^5$ m^2s^{-1} (Fig. 5c). The diffusion coefficient gradually increases in the upper stratosphere in order to avoid wave reflection from the model top. A maximum diffusion coefficient of 4×10^6 m^2s^{-1} is assumed in the lower mesosphere (Fig. 5b). Between $\eta = 0.6$ and $\eta = 0.8$ the horizontal diffusion coefficient approaches zero in order to reduce coordinate transformation errors in regions of steep orography as discussed in section 4.2.

KMCM simulates the boreal winter climate and its intraseasonal variability quite reasonably (Becker and Schmitz, 2001; Körnich et al., 2003). This is illustrated in Figs. 8-10. These results may be compared to observational analyses and other model data provided for instance by Randel (1992) or Roeckner et al. (1992). In the troposphere and stratosphere, zonal-mean zonal wind and temperature (Figs. 8a,b) are sufficiently realistic in view of the simplicity of the model. Also the transient and stationary eddy momentum and heat fluxes are simulated appropriately (Fig. 9). Furthermore, the main features of the stationary waves in the troposphere and lower stratosphere as well as the horizontal distribution of transients are captured (Fig. 10). In the following we discuss results obtained with this T42/L24 version of *KMCM*.

5.2.2 Effects of conventional momentum diffusion versus new diffusion and dissipation forms

As in section 5.1 we inspect two integrations of the model. Here, we consider 10 year perpetual January integrations preceded by sufficiently long spin-up times. In the *control* run (Figs. 8-10), horizontal momentum diffusion is included using (3.7), and the dissipation is fully accounted for according to (3.9) and (4.12). In the corresponding *conventional* run, (3.7) is substituted by

$$\mathbf{H}_c = K_h \{ \nabla^2 \mathbf{v} + \nabla D \} , \tag{5.8}$$

and the frictional heating terms (3.9) and (4.12) are omitted. The model setup of the conventional run is otherwise identical to that of the control run.

The climatological differences between the conventional run and the control run are depicted in Fig. 11 for zonal-mean zonal wind and temperature. The 99% statistical significance range based on Student's t-test is indicated by shading. The representation reveals a significant sensitivity of the simulated zonal-mean climate to employing (5.8) instead of (3.7) and omitting the frictional heating terms. In the conventional run, the stratospheric polar night jet is clearly stronger and colder. The signal extends down to the lower troposphere where polar temperatures decrease by about 0.5^0 C. These high-latitude anomalies are quite similar when only the frictional heating terms are neglected (Becker, 2003, Fig. 2). It can be proven that they are due to somewhat reduced planetary wave activity in the conventional run (see Becker 2003, Fig. 4) and, hence, that they are an indirect rather than direct consequence of neglecting the frictional heating terms. The anomalous stratospheric superrotation component visible in Fig. 11a results from substituting (3.7) by (5.8). This signal is again indirect since the difference between the diffusion forms (5.8) and (3.7) would suggest an anomalous damping rather than amplification of the superrotation component.

(a) *u at 200 mb (ms^{-1})*

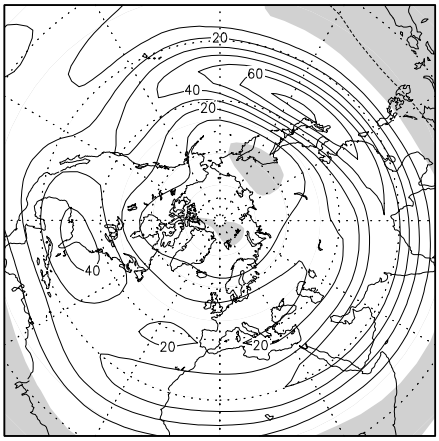

height at 200 mb (m)* (b)

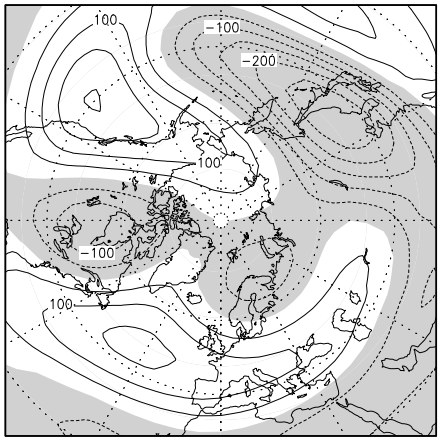

(c) *T* at 30 mb (K)*

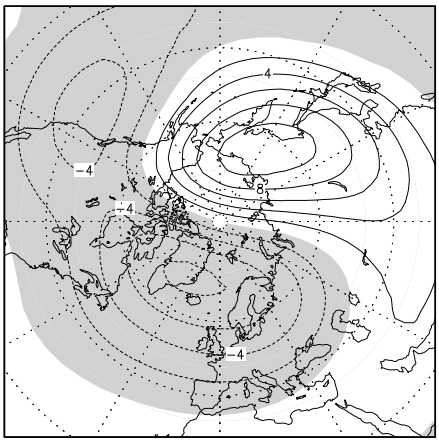

height at 30 mb (m)* (d)

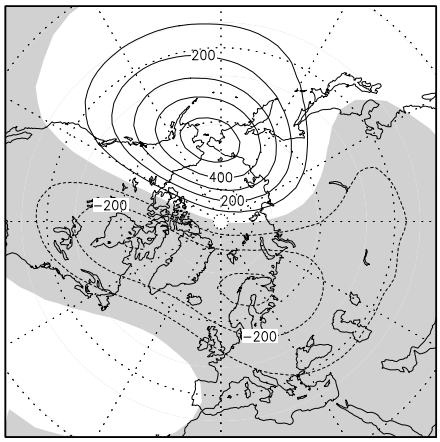

(e) *tr. u^*v^* at 300 mb (m^2s^{-2})*

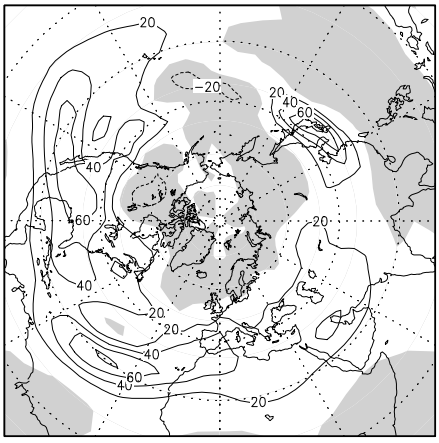

tr. T^*v^* at 750 mb (Kms^{-1}) (f)

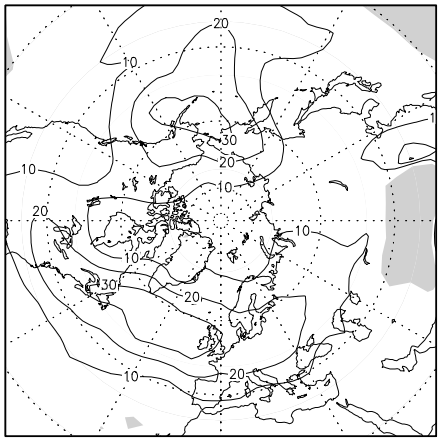

Figure 10 (previous page): Model climatology of the T42/L24 version of *KMCM*. (a) Zonal wind at 200 mb (contour interval 10 ms^{-1}). (b) Eddy component of geopotential height at 200 mb (contour interval 50 m). (c),(d) Eddy components of temperature and geopotential height at 30 mb (contour intervals 2 K and 100 m). (e) Transient eddy momentum flux at 300 mb (contour interval 20 m^2s^{-2}). (f) Transient eddy heat flux at 750 mb (contour interval 10 Kms^{-1}). Zero contours are not drawn, and negative values are shaded.

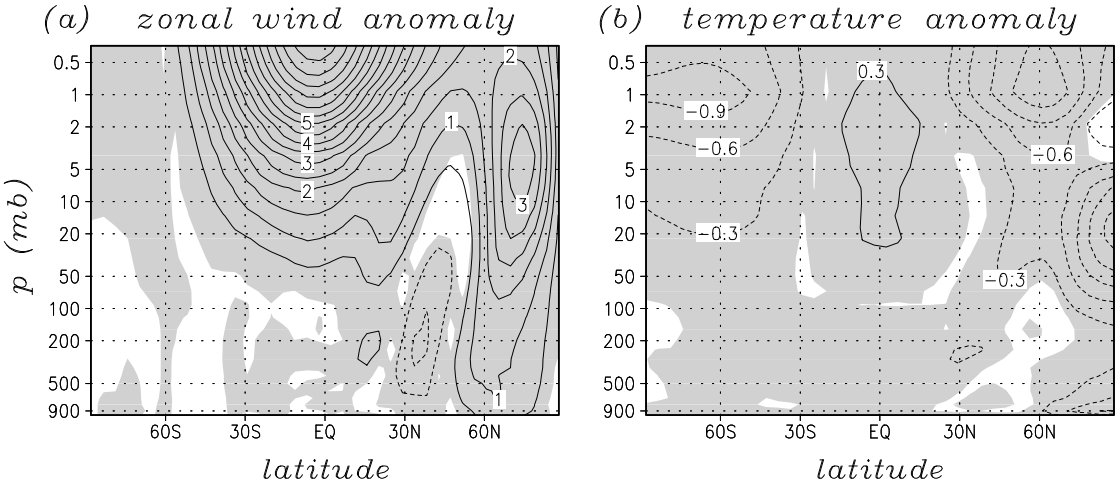

Figure 11: Climatological zonal-mean zonal wind and temperature differences in the conventional run from the control run. The contour intervals are (a) 0.5 ms^{-1} and (b) 0.3 K. In addition, the 99% confidence range based on Student's t-test is indicated by shading. Zero contours are not drawn.

Given that the climatological differences in the conventional run from the control run are weak compared to the uncertainties of any climate model to adjustments of all kind of parameterizations, there appears to be no necessity for employing the proposed friction and dissipation forms in present-day GCMs. More convincing arguments follow from the global angular momentum and energy budgets.

Similar to estimates given by Lorenz (1967), the Eulerian law of angular momentum conservation (e.g., Serrin, 1959, section 7; Lindzen, 1990, section 6.2) is applied to a fluid volume ranging from the ground to the top of the model atmosphere and from the South Pole to some latitude ϕ_1 farther north. The angular momentum component parallel to the axis of the earth is considered in the temporal mean. It follows that the northward flux of relative angular momentum must be balanced by the mountain torque plus the total friction torque, hence

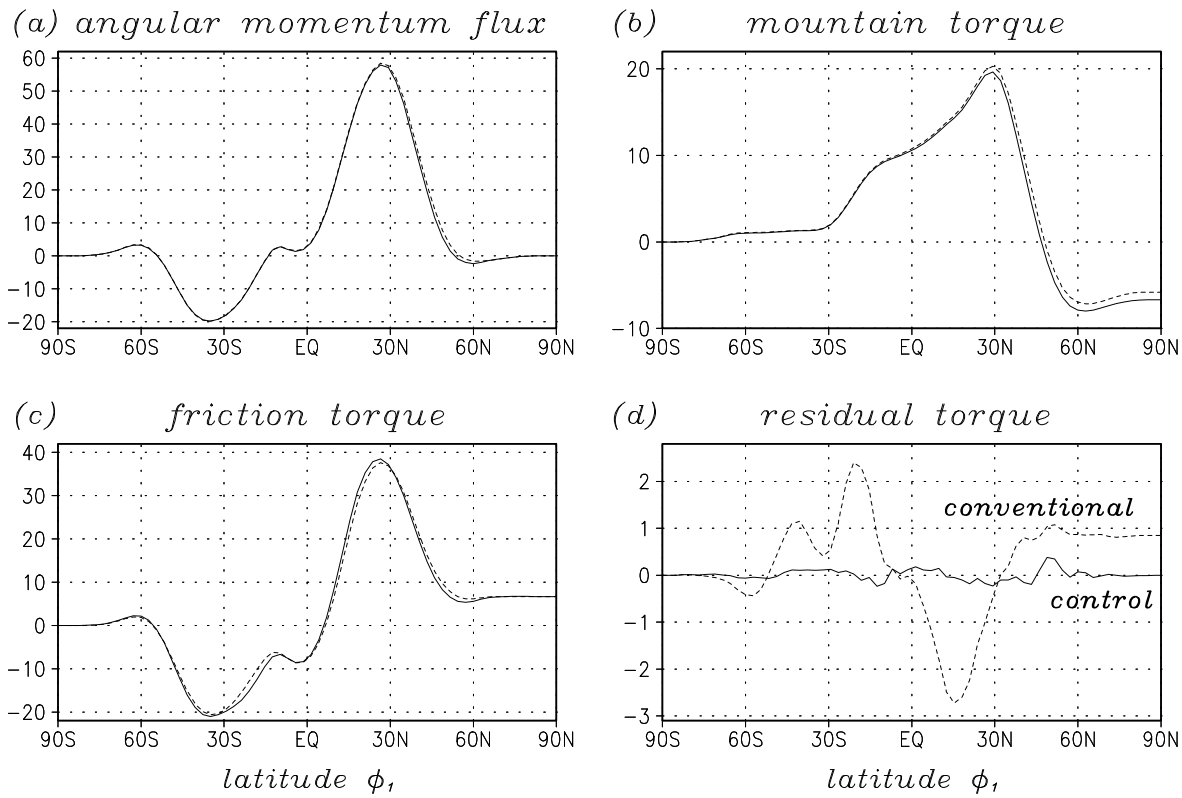

Figure 12: Evaluation of the angular momentum budget (5.9) in the control run (solid lines) and in the conventional run (dashed lines). The unit is 10^{18} Nm.

$$< \Big[(a_e \cos\phi)^2 \int_0^{2\pi} d\lambda \int_{z=z_s}^{\infty} dz\, \rho\, v\, u \Big]_{\phi=\phi_1} > \; = \; < a_e^3 \int_0^{2\pi} d\lambda \int_{-90^0}^{\phi_1} \cos^2\phi\, d\phi\; z_s\, \partial_x p_s >$$

$$+ < a_e^3 \int_{-90^0}^{\phi_1} \cos^2\phi\, d\phi \Big[(-\mathbf{\Sigma}_z\, \mathbf{e}_z) \cdot \mathbf{e}_x \Big]_{z=z_s} > \qquad (5.9)$$

$$+ < \Big[a_e^2 \cos^2\phi \int_0^{2\pi} d\lambda \int_{z=z_s}^{\infty} d\,z\, (\mathbf{\Sigma}_h\, \mathbf{e}_y) \cdot \mathbf{e}_x \Big]_{\phi=\phi_1} > .$$

Time averaging is indicated by the symbol $< \;\; >$. The first term on the rhs of (5.9) is the mountain torque; the second term represents the torque owing to surface friction which must be calculated according to Eqs. (3.6) and (4.6). The torque owing to horizontal momentum diffusion, already discussed in Becker (2001), appears as a third term on the rhs of (5.9). The finite-difference representation of Eq. (5.9) is straightforward.

Figure 12 shows the evaluation of the angular momentum budget for the control run (solid lines) and the conventional run (dashed lines). (Even though the full 10 year time

series are taken into account, it should be noted that almost identical results are obtained if only a few hundred day time series are retained.) The northward angular momentum flux, the mountain torque, and the friction torque are very similar in both runs. The residual torque is defined as the rhs minus the lhs of Eq. (5.9). For the conventional run the third term on the rhs of (5.9) is not defined and must be omitted. This accounts for the strong residual torque if the northward boundary ϕ_1 of the fluid volume lies in the region of the tropical Hadley cells. A significant residuum remains in the conventional simulation also for $\phi_1 \to 90^0$N. In the control run the corresponding deficiency is negligible for all ϕ_1. Considering the exact values for $\phi_1 = 90^0$N, one obtains a residual torque of 8.5×10^{17} Nm in the conventional run versus -5.5×10^{15} Nm in the control run. In relation to the relative angular momentum of the atmosphere (typically 1.5×10^{26} Nms), either value appears to be of minor importance for climate modeling. That is, the time scales by which the relative angular momentum of the atmosphere is artificially generated or removed via the residual torques, 2050 days in the conventional run or 315000 days in the control run, are very long.

The long-term energy budget of the model atmosphere can be analysed analogously to the angular momentum budget. Using the same fluid volume as in (5.9), it follows from the energy conservation law (2.62) supplemented by the no-slip condition that the poleward flux of total enthalpy is balanced by the bulk heating, the surface sensible heat flux, the horizontal diffusion of heat, and the work owing to horizontal momentum diffusion. Thus we have

$$
\begin{aligned}
< \Big[a_e \cos\phi \int_0^{2\pi} d\lambda \int_{z=z_s}^{\infty} dz\, \rho\, v\, (c_p T + g z + \mathbf{v}^2/2) \Big]_{\phi=\phi_1} > \\
= \quad < a_e^2 \int_0^{2\pi} d\lambda \int_{-90^0}^{\phi_1} \cos\phi\, d\phi \int_{z=z_s}^{\infty} dz\, c_p\, \rho\, Q > \qquad (5.10) \\
- < a_e^2 \int_0^{2\pi} d\lambda \int_{-90^0}^{\phi_1} \cos\phi\, d\phi \Big[c_p\, \rho\, K_z \frac{T}{\Theta}\, \partial_z \Theta \Big]_{z=z_s} > \\
+ < \Big[a_e \cos\phi \int_0^{2\pi} d\lambda \int_{z=z_s}^{\infty} dz\, c_p\, \rho\, \frac{K_h}{2}\, \partial_\phi T \Big]_{\phi=\phi_1} > \\
+ < \Big[a_e \cos\phi \int_0^{2\pi} d\lambda \int_{z=z_s}^{\infty} dz\, (\boldsymbol{\Sigma}_h\, \mathbf{e}_y) \cdot \mathbf{v} \Big]_{\phi=\phi_1} > .
\end{aligned}
$$

The finite-difference representation of (5.10) is again straightforward. Figure 13 shows the numerical result analogously to Fig. 12. The sum of the second and third term on the rhs of (5.10) is plotted as the boundary heat flux in panel (c). Here, the horizontal

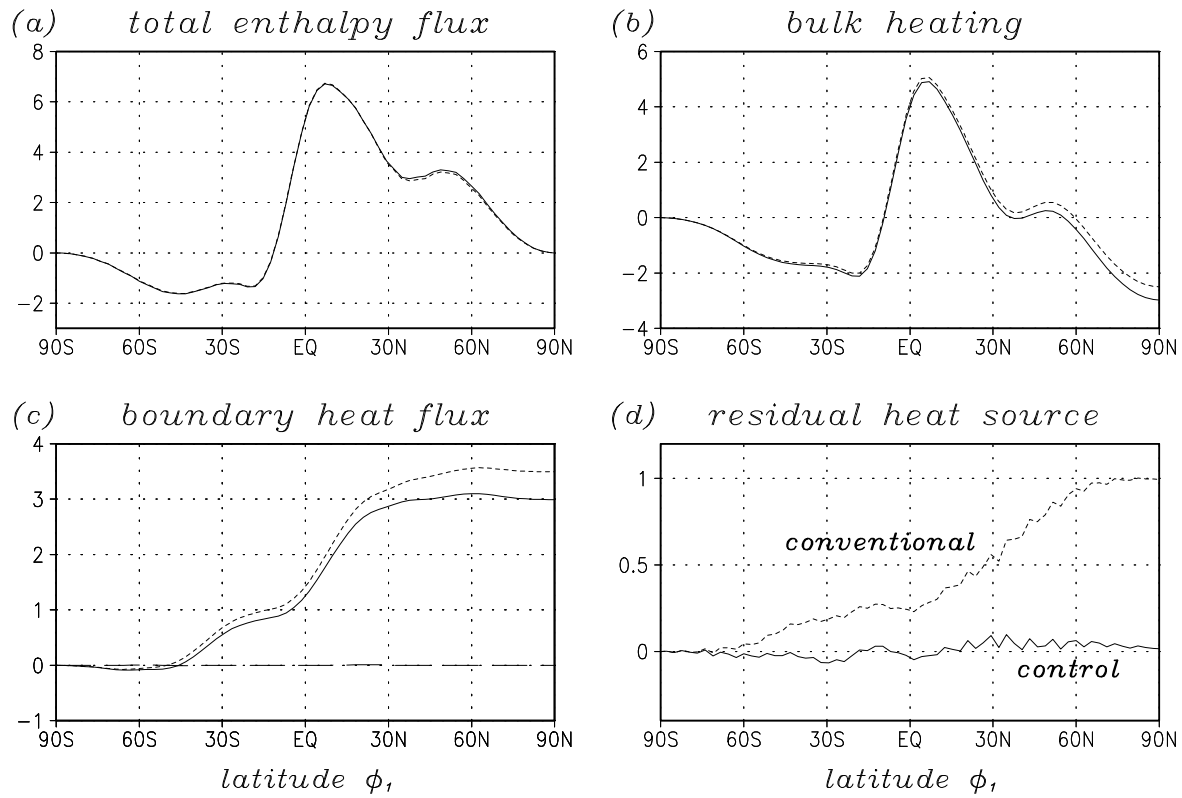

Figure 13: Evaluation of the energy budget (5.10) in the control run (solid lines) and in the conventional run (short-dashed lines). The long-dashed line in panel (c) shows the work done by horizontal momentum diffusion (last term on the rhs of (5.10)) for the control run. The unit is 10^{15} Js^{-1}.

temperature diffusion is negligible. The same holds for the work due to horizontal frictional stress (last term on the rhs of (5.10)) which, for the control run, is indicated by the long-dashed line in panel (c). The residual heat source (panel (d)) is defined as the rhs minus the lhs of (5.10). For $\phi_1 = 90^0$ this residuum solely consists of the bulk heating and the surface sensible heat flux and thus represents the net thermal forcing of the model.

The long-term net thermal forcing should be zero. However, with the conventional model definition a spurious residual heat source of about 1×10^{15} Js^{-1} or, equivalently, 1.95 Wm^{-2} remains. This residuum turns out to be quite robust against tuning of model parameters, and it is obtained as well on the basis of much shorter than 10 year time series. On the other hand, the residual heat source present in the control run appears to be negligible for all ϕ_1. For $\phi_1 = 90^0$ a value of 1.65×10^{13} Js^{-1} (or 0.032 Wm^{-2}) is obtained.

In the conventional case both the bulk heating and the boundary heat flux are al-

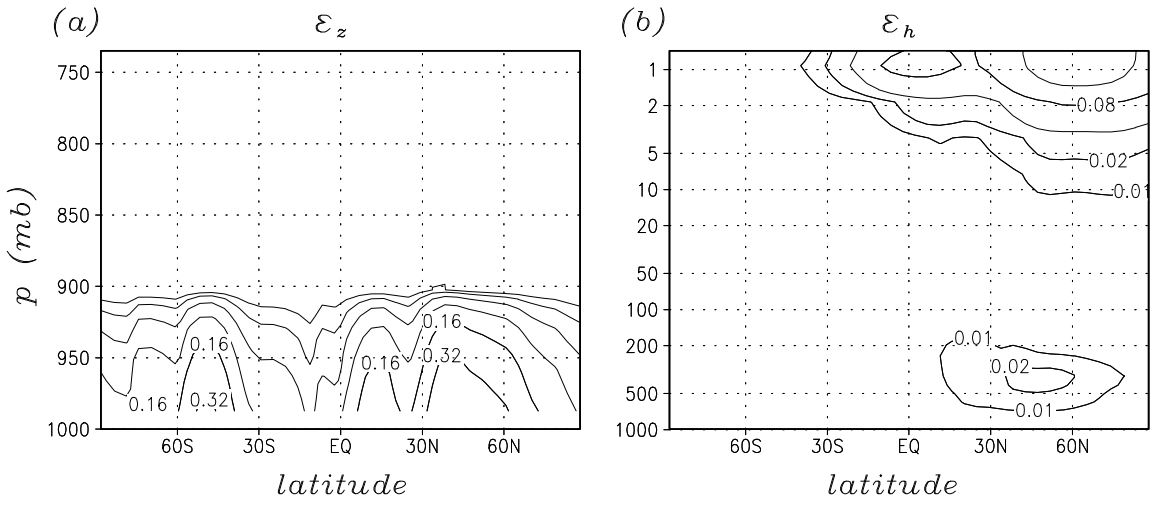

Figure 14: Simulated long-term zonal-mean dissipation rates owing to (a) vertical and (b) horizontal momentum diffusion in the control run. Contours are drawn for $0.01, 0.02, 0.04, 0.08, 0.16$, and 0.32 Kd^{-1}. Zonal averaging has been performed on hybrid surfaces, and the vertical pressure coordinate corresponds to $\eta \times 1013$ mb. The global integrals of the respective dissipation rates give rise to (a) 1.31 and (b) 0.6 Wm^{-2}.

ways greater than in the control run. This bias increases with increasing ϕ_1, presumably because the lack of frictional heating accumulates. Accordingly, a residuum of about 2 Wm^{-2} should be quantitatively consistent with the global integral of the simulated dissipation in the control run. In fact, a globally averaged frictional heating of 1.91 Wm^{-2} can be diagnosed from the control simulation. Figure 14 shows the corresponding climatological zonal means of ϵ_z and ϵ_h. The dissipation due to vertical momentum diffusion is most relevant in the boundary layer. Such a behavior has also been found by Bister and Emanuel (1998) in the simulation of a tropical cyclone. In the present case, typical boundary layer heating dissipation rates are of the order of 0.3 Kd^{-1}. Disregarding the model stratosphere, significant dissipative heating rates due to horizontal momentum diffusion show up in the middle and upper winter troposphere. However, the tropospheric maximum of ϵ_h is not much in excess of 0.02 Kd^{-1}. In the global mean, the vertical dissipation term gives the main contribution of about 1.31 Wm^{-2} while horizontal dissipation accounts for 0.6 Wm^{-2}.

It is noteworthy that a simulated mean dissipation rate of about 1.9 Wm^{-2} fits well within the range of existing estimates based on observational analyses of the general circulation. Oort (1964) finds a value of 2.3 Wm^{-2} (see also Lorenz, 1967, chapter V). Some modern textbooks suggest somewhat lower dissipation rates between 1.8 and 1.9

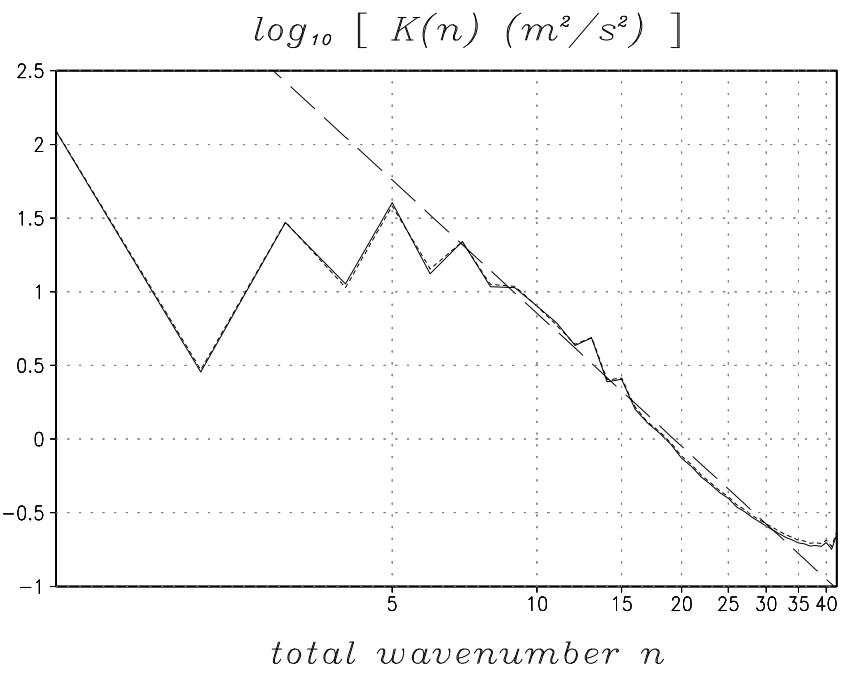

Figure 15: Simulated long-term kinetic energy spectra in the upper troposphere, averaged over the 196, 242, and 296 mb layers. Solid lines correspond to the control run and short-dashed lines to the conventional run. The scaling of the axes is logarithmic, and the straight long-dashed line gives the n^{-3} fit in the range of synoptic wave numbers.

Wm^{-2} (e.g., James, 1994, section 5.3; Prandtl et al., 1990, chapter 8). Thus, with regard to the total kinetic energy typically contained in the atmosphere ($\sim 8 \times 10^{20}$ J or $\sim 1.6 \times 10^6$ Jm^2), a neglect of dissipation in conventional GCMs means that within about 9 days, an equivalent amount of kinetic energy is removed from the flow without being dissipated into heat. It follows that, apart from other uncertainties associated with parameterizations and numerical truncation, conventional GCMs have a systematic imbalance of about 2 Wm^{-2} between the incoming and outgoing radiation.

It has been noted in chapter 3 that state-of-the-art GCMs used for climate prediction or weather forecasting generally utilize higher order than harmonic horizontal diffusion. The reasoning often is that a higher order scale-selective damping is better suited to simulate the synoptic n^{-3} branch of the kinetic energy spectrum in the upper troposphere (e.g., Smagorinsky, 1993). Such a spectrum is predicted by quasi two-dimensional turbulence (e.g., Salmon, 1998, chapter 4), and it is indeed observed for the synoptic scales down to wavelengths about 500-1000 km (Nastrom and Gage, 1985). On the other hand, we have concluded in chapter 3 that one must stick to a harmonic diffusion scheme for the dissipation to be positive definite. The question arises whether the energy spectrum in the free atmosphere can be simulated properly using the proposed second-order horizontal

diffusion scheme.

The definition of the kinetic energy in spectral space is given in appendix A.4 by Eq. (A60). Figure 15 shows corresponding computational results for the control run and the conventional run, averaged over three model layers located around 250 mb in each case. Both simulations yield quite similar results. For high wave numbers, the kinetic energy is slightly higher in the conventional case. In the range of synoptic waves for total wave numbers from about 7 to 25, both simulated energy spectra clearly exhibit the prominent n^{-3} slope. This result demonstrates that harmonic horizontal momentum diffusion is well suited to simulate the kinetic energy spectrum associated with atmospheric macro turbulence. Such a conclusion is also evident from the very high resolution experiments of Koshyk and Hamilton (2001) who have utilized the SKYHI model with the conventional harmonic momentum diffusion scheme.

5.2.3 Additional perturbation runs

Zero trace of the stress tensor

In Becker (2001) it was noted that using the zero-trace horizontal momentum diffusion and dissipation forms (3.12) and (3.13) instead of (3.7) and (3.9) leads to essentially identical results in multiple baroclinic life cycle experiments. This finding does not necessaryly apply in the present control simulation which is more complicated due to planetary waves and a higher horizontal resolution. Indeed, significant differences in the model climatology are obtained if (3.7) and (3.9) are substituted by the corresponding zero-trace forms (3.12) and (3.13). The zonal wind and temperature differences between the corresponding perturbation run and the control run are shown in Fig. 16. Regions where the statistical significance exceeds 99% are shaded. Particularly the zonal wind signal is indicative of enhanced wave activity in the subtropical troposphere. In contrast, both wind and temperature anomalies reveal reduced wave activity in the stratosphere.

Evaluation of (5.9) and (5.10) yields a residual torque of -6.1×10^{16} Nm and a residual heat source of 0.23 Wm^{-2} in the perturbation run. Both values are about one order of magnitude weaker than in the conventional case, but they are nevertheless much stronger than in the control run. A possible explanation is that, when using (3.12), the damping of resolved gravity wave components is only half as strong than with (3.7). This may cause stronger aliasing errors since the divergent part of the flow becomes more and more important at the high wave number end of the kinetic energy spectrum (Koshyk and Hamilton, 2001). The simulated global dissipation in the perturbation run amounts to about 1.74 Wm^{-2}. This value together with the residual heating of 0.23 Wm^{-2} is again close to the simulated dissipation in the control run.

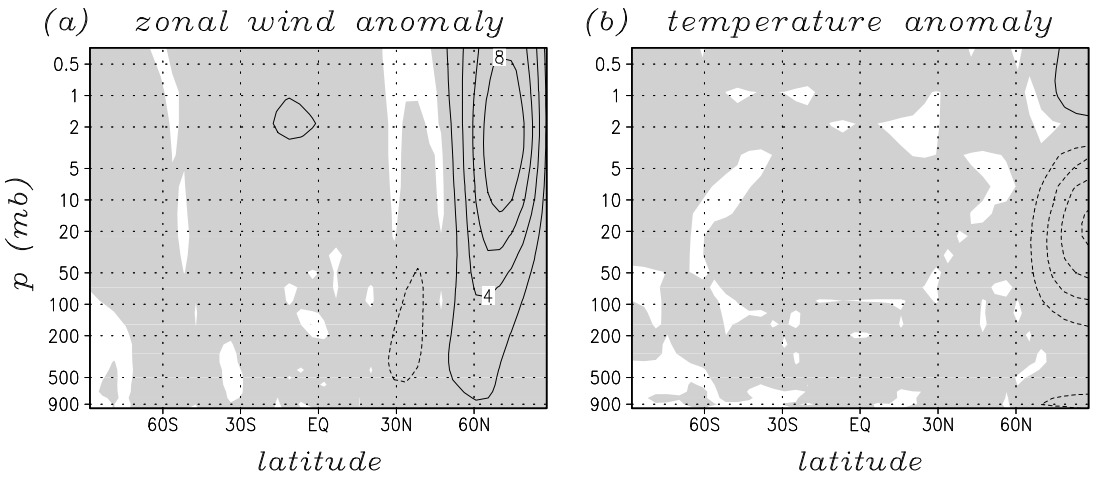

Figure 16: Climatological differences between the perturbation run which employs Eqs. (3.12) and (3.13) and the control run. Shown are the anomalies for zonal-mean zonal wind and temperature (contour intervals 2 ms^{-1} and 1 K). As in Fig. 11, the shading indicates the 99% confidence range based on a Student's t-test, and zero contours are not drawn.

Finite horizontal diffusion in the lower troposphere

One further perturbation run has been performed, using the horizontal diffusion coefficient shown by the dashed line in Fig. 5c while otherwise retaining the model setup of the control run. Figure 17 shows the climatological differences between this second perturbation run and the control run for zonal-mean zonal wind and temperature (including statistical significance levels), as well as for the meridional eddy fluxes of zonal wind and temperature. All anomalies clearly indicate a considerable reduction of wave activity throughout the troposphere and stratosphere. Thus, the usual model design of retaining horizontal diffusion in the lower troposphere can significantly weaken the overall simulated wave activity. Figure 17 reveals that the effect is particularly crucial to the stratospheric circulation.

Evaluation of (5.9) yields a residual global torque of 1.2×10^{17} Nm for the present perturbation run. This value is only a factor 7 weaker than that obtained in the conventional run, and it is about 20 times stronger than the residual torque obtained in the control run. Hence, employing zero horizontal diffusion in the lower troposphere proves to be sufficient to avoid coordinate transformation errors.

A strong spurious heat source in the present perturbation run is not expected. Mainly because the main contribution to the overall dissipation is due to vertical momentum diffusion and, to some extent, due to horizontal momentum diffusion in the upper troposphere (Fig. 14). Accordingly, a residual heating of 1.56×10^{13} Js^{-1} is obtained which is

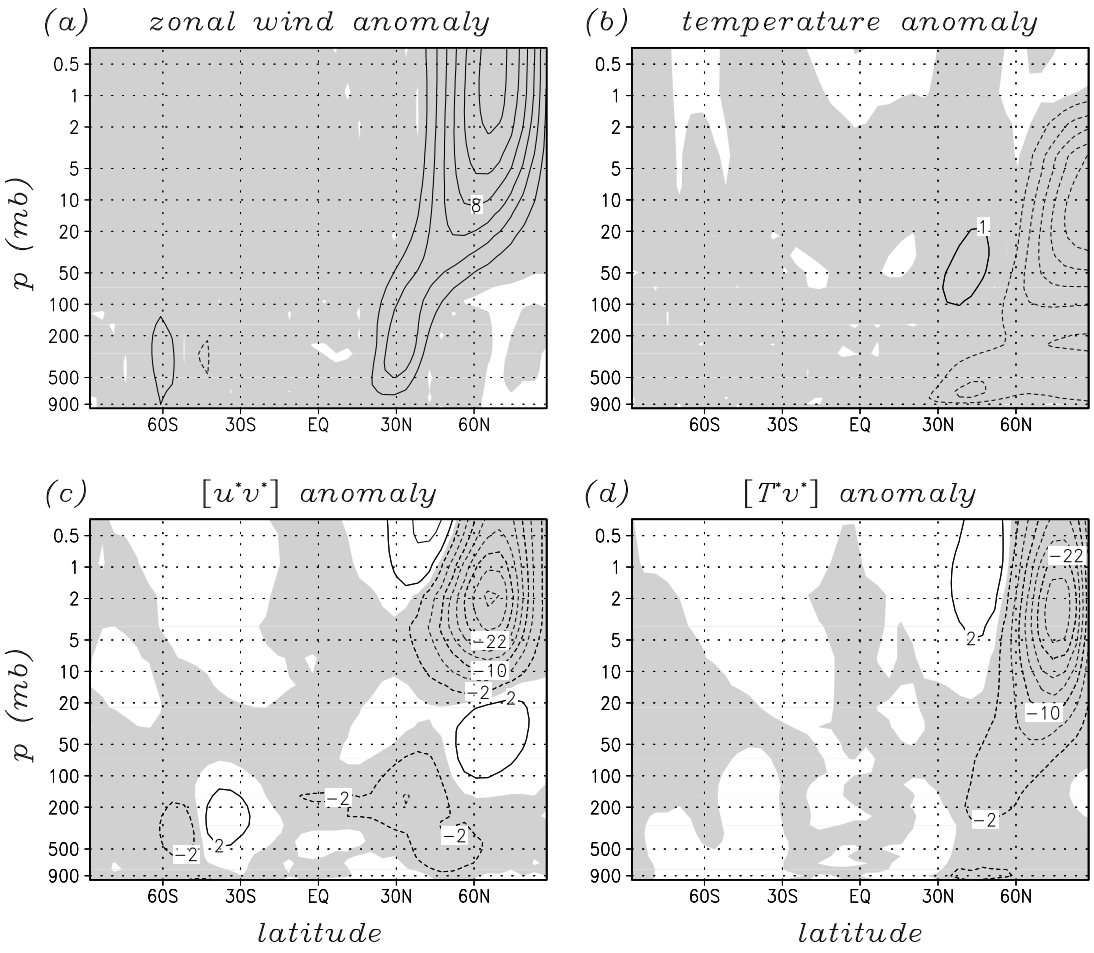

Figure 17: Climatological differences between the perturbation run with finite horizontal diffusion in the boundary layer and the control run. Shown are the anomalies for (a) zonal-mean zonal wind (contour interval 2 ms^{-1}), (b) temperature (contour interval 1 K), (c) eddy momentum flux (contours $\pm 2, \pm 6, -10, -14, \ldots$ m^2s^{-2}), and (d) eddy heat flux (contours $\pm 2, -6, -10, -14, \ldots$ Kms^{-1}). Zero contours are not drawn. The shading in (a),(b) indicates the 99% confidence range based on a Student's t-test. The shading in (c),(d) indicates negative values.

close to that of the control run. However, the global mean frictional heating amounts to 1.64 Wm^{-2} which is 0.27 Wm^{-2} weaker than in the control run. This effect can be attributed to the weaker wave activity in the present perturbation run (Figs. 17c,d). Since less kinetic energy is generated by conversion of available potential energy, the overall dissipation must decrease by the same amount.

Chapter 6

Numerical experiments including parameterization of internal gravity waves

With regard to gravity wave breakdown and turbulent stress, new forms of the planetary-scale heat and energy budgets have been proposed in section 2.4. In this chapter we quantitatively assess the local heat budget in the MLT by analysing permanent January model runs. In particular, computational estimates of the climatological-mean frictional heating owing to gravity wave wind shear, first presented by Becker and Schmitz (2002), are derived. In this context we also address the important question to what extent the dissipation of gravity wave kinetic energy is balanced by adiabatic conversion of mean enthalpy. Furthermore, the entropy flux generated by the IGWs themselves is assessed. As the basis of these model estimates we apply the simple GCM *KMCM* introduced in the previous chapter. The model is employed with an extended vertical resolution, and it is supplemented by an appropriate gravity wave parameterization based on the concept of Lindzen (1981).

In the following section we extend Lindzen's gravity wave saturation theory by the derivation of all gravity wave effects mentioned in section 2.4. Then, after a brief description of the modified version of *KMCM*, we inspect a long-term control simulation with particular emphasis on the heat budget in the MLT. In addition, we assess the model sensitivity to the choice of the effective Prandtl number which, according to the analysis to be proposed, should not exceed a value of 2. Finally, possible north-south asymmetries in the MLT are estimated by comparing the control simulation against the corresponding aquaplanet model run.

6.1 Gravity wave saturation theory

6.1.1 Linear wave analysis with turbulent diffusion

Let us consider the linear propagation of internal gravity waves (IGWs) in an isothermal background atmosphere. To simplify the notation, the horizontal direction of wave propagation is assumed to be in the x-direction, and the corresponding background horizontal wind component is $u(z)$. $\mathcal{D}$ denotes the turbulent diffusion coefficient. Assuming the Boussinesq approximation and hydrostatic balance for the wave perturbations, the governing equations are

$$\begin{aligned}
(\,\partial_t + u\,\partial_x - \mathcal{D}\,\partial_z^2\,)\,u' &= -\rho^{-1}\,\partial_x\,p' && (6.1)\\
(\,\partial_t + u\,\partial_x - \mathcal{D}\,\partial_z^2\,)\,\Theta' &= -w'\,\partial_z\,\Theta && (6.2)\\
\rho^{-1}\,\partial_z\,p' &= g\,\Theta'\,\Theta^{-1} && (6.3)\\
\partial_x\,u' + \partial_z\,w' &= 0\,. && (6.4)
\end{aligned}$$

The system (6.1)-(6.4) differs from that given by Holton (1992, section 7.4) by the explicit inclusion of turbulent diffusion and by the assumption of hydrostatic balance for the IGWs. Note that the latter assumption is inherent in present-day gravity wave parameterizations (e.g., Holton, 1983; Hines, 1997). After some standard manipulations and assuming that the background wind varies very slowly with height, we can derive from (6.1)-(6.4) a single differential equation for the vertical wind perturbation:

$$\{\,(\,\partial_t + u\,\partial_x\,)^2 - 2\,(\,\partial_t + u\,\partial_x\,)\,\mathcal{D}\,\partial_z^2\,\}\,\partial_z^2\,w' + N^2\,\partial_x^2\,w' = 0\,. \qquad (6.5)$$

Here, a term nonlinear in $\mathcal{D}$ is neglected, and $N^2 = g\,\partial_z\Theta\,/\,\Theta$ is the Brunt-Väisälä frequency squared of the mean state. Equation (6.5) is solved by the wave ansatz

$$w' = \tilde{w}(z)\exp\{\,\frac{z}{2\,H} + i\,k\,(\,x - c\,t\,)\,\}\,, \qquad (6.6)$$

where $H = RT/g$ is the scale height. $k > 0$ and $c > 0$ denote the horizontal wave number and the phase speed of the wave. $\tilde{w}$ satisfies the differential equation

$$d_z^2\,\tilde{w} + \lambda_r^2\,\tilde{w} + i\,\frac{2\,\mathcal{D}}{k\,(\,u - c\,)}\,d_z^4\,\tilde{w} = 0\,, \qquad (6.7)$$

where

$$\lambda_r := \frac{N}{u - c} \qquad (6.8)$$

is the real part of the vertical wave number. Since we wish to consider only gravity waves with downward phase propagation or, equivalently, with upward energy flux, we must

require that $\lambda_r < 0$, hence $c \geq u$. For weak vertical diffusion, Eq. (6.7) has the WKB solution

$$\tilde{w} \;=\; B \sqrt{\frac{c-u(z)}{c-u_0}} \exp\{\, i \int_{z_0}^{z} \lambda_c \, dz' \,\} \quad \text{with} \quad \lambda_c := \lambda_r + i\,\lambda_i \,. \tag{6.9}$$

Here, z_0 represents the level of gravity wave excitation and $u_0 := u(z_0)$ such that B is the wave amplitude at that level. The imaginary part λ_i of the complex vertical wave number λ_c describes the damping of the wave amplitude owing to vertical diffusion. Inserting (6.9) into (6.7), we find (see also Holton, 1982, Eq. (26))

$$\lambda_i = \frac{\mathcal{D}\, N^3}{k\,(u-c)^4} \,. \tag{6.10}$$

With the aid of (6.4) the general form of the vertical flux of horizontal momentum is

$$\rho\, \overline{\mathrm{Re}\,(u')\,\mathrm{Re}\,(w')} = -\,\frac{\rho\,\lambda_r}{k}\,\overline{(\,\mathrm{Re}\,(w')\,)^2}\,. = -\,\frac{\rho\,\lambda_r}{2\,k}\,\overline{w'\,w'^*}\,. \tag{6.11}$$

The complex conjugate is indicated by an asterisk. As in section 2.3, the average extends over the horizontal and temporal scales of the wave. Inserting (6.6) and (6.9) into (6.11), introducing Holton's abbreviation

$$\tilde{u}^3 := B^2\, N^2\, k^{-2}\,(\,c-u_0\,)^{-1} > 0\,, \tag{6.12}$$

and defining ρ_{00} as the surface density of the background state, the momentum flux becomes

$$\rho\, \overline{\mathrm{Re}\,(u')\,\mathrm{Re}\,(w')} = \frac{\rho_{00}\, k\, \tilde{u}^3}{2\,N} \exp\{-2 \int_{z_0}^{z} \lambda_i \, dz' \,\}\,. \tag{6.13}$$

This expression illustrates that, given the horizontal wave number k, Holton's wave parameter $\tilde{u}$ determines the wave momentum flux at the initial level. Furthermore, the momentum flux (6.13) is constant in the absence of turbulent diffusion, and this is in accordance with the second theorem of Eliassen and Palm (Lindzen, 1990, chapter 8).

Remembering Eq. (3.10), the frictional heating associated with the wave's vertical wind shear can be calculated in the same fashion as the momentum flux:

$$\mathcal{D}\,\overline{(\,\partial_z \mathrm{Re}\,(u')\,)^2} = \frac{\mathcal{D}\,\lambda_r^4}{2\,k^2}\,\overline{w'\,w'^*} = \frac{\mathcal{D}\,|\lambda_r|^3\,\tilde{u}^3}{2\,N} \exp\{\,\frac{z}{H} - 2\int_{z_0}^{z} \lambda_i \, dz' \,\}\,. \tag{6.14}$$

In order to assess the vertical flux of entropy we write

$$\Theta' = \zeta(z)\, w'\,, \tag{6.15}$$

where the approximate form of the function ζ follows from (6.2),(6.6),(6.9) for $|\lambda_i| \ll |\lambda_r|$

$$\zeta(z) = \frac{-\partial_z\,\Theta}{\mathcal{D}\,\lambda_r^2 + i\,k\,(\,u-c\,)} \approx -\,\frac{\partial_z\,\Theta}{k\,(\,c-u\,)}\left(i + \frac{\mathcal{D}\,\lambda_r^2}{k\,(\,c-u\,)}\right). \tag{6.16}$$

Accordingly we get for the entropy flux

$$\begin{aligned} \frac{c_p}{\Theta}\,\overline{\mathrm{Re}\,(\Theta')\,\mathrm{Re}\,(w')} &= \frac{c_p}{4\,\Theta}\,(\,\zeta^* + \zeta\,)\,\overline{w'\,w'^*} \\ &= -\,\mathcal{D}\,\frac{c_p\,\tilde{u}^3\,\partial_z\,\Theta}{2\,\Theta\,(\,c-u\,)^3}\exp\{\,\frac{z}{H} - 2\int_{z_0}^{z}\lambda_i\,dz'\,\}\,. \end{aligned} \tag{6.17}$$

As expected, (6.17) vanishes in the case of conservative wave propagation, that is, for $\mathcal{D} = 0$.

The wave pressure flux follows immediately from the first theorem of Eliassen and Palm (Lindzen, 1990, Eq. (8.14)):

$$\overline{\mathrm{Re}\,(p')\,\mathrm{Re}\,(w')} = (\,c-u\,)\,\rho\,\overline{\mathrm{Re}\,(u')\,\mathrm{Re}\,(w')}\,. \tag{6.18}$$

In Lindzen's book this theorem is derived for frictionless wave propagation. It is readily shown that the theorem holds as well in the more general case with vertical diffusion.

6.1.2 Lindzen's saturation assumption

Between the level of wave excitation and the breaking level z_b the wave is assumed to propagate conservatively, that is, $\mathcal{D} = 0$ for $z_0 \le z < z_b$. The breaking level itself is implicitly defined by the condition that the background state plus the wave reach static instability, hence

$$|\,\lambda_r\,\Theta'\,| = \partial_z\,\Theta \quad \text{for} \quad z = z_b\,. \tag{6.19}$$

Inserting Θ' from (6.15) and (6.16), retaining only the leading term from (6.16), and dividing by $\partial_z\,\Theta$, the criterion (6.19) can be written as

$$\frac{B\,|\lambda_r|}{k\,\sqrt{(c-u)(c-u_0)}}\exp\{\frac{z}{2\,H}\} = 1 \quad \text{for} \quad z = z_b\,. \tag{6.20}$$

Using the definition (6.12) we get

$$z - 3\,H\ln\{\,(\,c-u\,)\,/\tilde{u}\,\} = 0 \quad \text{for} \quad z = z_b, \tag{6.21}$$

which is identical with Eq. (21) in the paper of Holton (1982).[1] Lindzen's saturation assumption states that the turbulent diffusion generated above z_b keeps the background

[1] In Holton (1982) as well as in Lindzen (1981), the stability criterion is defined as $|\,\lambda_r\,T'\,| = g/c_p$. This means, the wave pressure perturbation p' is ignored. Then, both authors invoke the enthalpy equation in the form $(\,\partial_t + u\,\partial_x\,)T' = -w'\,g/c_p$ in order to compute T' from w' . Here, the pressure perturbation is ignored once again such that the final stability criterion is correct. Note however that (6.19) can be expressed in terms of T' and p' yielding $|\,\lambda_r\,(\,T' - \frac{p'}{c_p\,\rho}\,)\,| = g/c_p$, and that the correct enthalpy equation corresponding to (6.2) is $(\,\partial_t + u\,\partial_x\,)\,(\,T' - \frac{p'}{c_p\,\rho}\,) = -w'\,g/c_p + T\,\Theta^{-1}\,\mathcal{D}\,\partial_z^2\,\Theta'$.

state plus the wave at marginal static instability. Assuming that the wave is finally 'swallowed' at the critical level z_c where $u = c$, Eq. (6.20) can be generalized as

$$\frac{B\,|\lambda_r|}{k\,\sqrt{(c-u)(c-u_0)}}\,\exp\{\frac{z}{2\,H}\,-\int_{z_0}^{z}\lambda_i\,dz'\,\}=1\quad\text{for}\quad z_b\le z<z_c \tag{6.22}$$

or, with regard to the definition (6.12), as

$$\exp\{-2\int_{z_0}^{z}\lambda_i\,dz'\,\}=\frac{(\,c-u\,)^3}{\tilde{u}^3}\,e^{-z/H}\quad\text{for}\quad z_b\le z<z_c\,. \tag{6.23}$$

The saturation condition (6.23) allows to compute the wave momentum flux, the wave-induced diffusion coefficient, the dissipation of gravity wave kinetic energy, and the wave entropy flux from (6.13), (6.10), (6.14), and (6.17). One finds the following expressions for $z_b \le z < z_c$:

$$\rho\,\overline{\mathrm{Re}\,(u')\,\mathrm{Re}\,(w')} = \frac{k\,\rho}{2\,N}\,(\,c-u\,)^3 \tag{6.24}$$

$$\mathcal{D} = \frac{k\,(\,c-u\,)^3}{2\,N^3}\,\{\,\frac{c-u}{H}+3\,\partial_z u\,\} \tag{6.25}$$

$$\mathcal{D}\,\overline{(\,\partial_z\mathrm{Re}\,(u')\,)^2} = \frac{1}{2}\,\mathcal{D}\,N^2 \tag{6.26}$$

$$\frac{c_p}{\Theta}\,\overline{\mathrm{Re}\,(\Theta')\,\mathrm{Re}\,(w')} = -\frac{c_p}{2\,\Theta}\,\mathcal{D}\,\partial_z\,\Theta\,. \tag{6.27}$$

Equations (6.24) and (6.25) are well known from Lindzen (1981). The dissipation rate (6.26) has already been mentioned by Becker and Schmitz (2002), whereas the gravity wave entropy flux (6.27) has been ignored in previous studies.

Equation (6.27) implies that the entropy flux convergence associated with nonconservative gravity wave propagation formally corresponds to a vertical diffusion of the mean stratification, involving the wave-induced diffusion coefficient with a Prandtl number of 2. Hence, even if we disregard the action of the wave-induced turbulent diffusion on the mean stratification, the wave-mean flow interaction implies such a diffusion. Stated otherwise, if we formally incorporate the wave entropy flux in the vertical diffusion term of Eq. (2.56), the present analysis imposes an upper bound of 2 for the effective Prandtl number in the MLT. This result goes beyond previous experimental and theoretical estimates suggesting a quite wide range for the Prandtl number (for reviews see: Thomas, 1996; Hocking, 1999). Note also that (6.27) has been derived by assuming that the turbulent Prandtl number is equal 1 at the scales of the IGWs, which is customary in saturation theory.

It can be proven that the system (6.13),(6.14),(6.17),(6.18) is fully consistent with Eq. (2.60). This is, of course, also true for the system (6.24)-(6.27) where the diffusion

coefficient has been specified. For a single gravity wave, the energy deposition yields with regard to (6.18),(6.24),(6.25)

$$E = -\frac{c-u}{\rho}\,\partial_z\,(\,\rho\,\overline{\mathrm{Re}\,(u')\,\mathrm{Re}\,(w')}\,) = \mathcal{D}\,N^2 \geq 0 \quad \text{for} \quad z_b \leq z < z_c\,. \tag{6.28}$$

Equation (6.28) reveals that the energy deposition is exactly twice as strong as the dissipation ϵ_{igw} given by (6.26). Furthermore we have $E = 0$ for conservative wave propagation, as it should be. Note that this holds neither for the pressure flux convergence nor for the residual work W_{res} (see Eq. (2.57)). Both terms can be different from zero whether the momentum flux changes with height or not. This paradox was already noted by Hines and Reddy (1967) or Lindzen (1973) and has been further discussed by Becker and Schmitz (2002). With the help of (6.27) and the identity $N^2 = \Theta^{-1} g\,\partial_z\,\Theta$ we can compute the entropy flux term on the rhs of (2.60), yielding

$$-g\,c_p^{-1}\,F_s = -\frac{g}{\Theta}\,\overline{\mathrm{Re}\,(\Theta')\,\mathrm{Re}\,(w')} = \frac{g}{2\,\Theta}\,\mathcal{D}\,\partial_z\,\Theta = \frac{1}{2}\,\mathcal{D}\,N^2\,. \tag{6.29}$$

It thus follows that the approximations introduced in sections 2.3 and 2.4 for the energetics of internal gravity waves are perfectly fulfilled by quasi-linear wave theory in association with Lindzen's saturation assumption, provided that all wave-mean flow interaction terms and the frictional heating term are consistently taken into account.

6.2 A simple GCM from the boundary layer up to the mesopause

In order to simulate the dynamics of the middle atmosphere up to the mesopause, we utilize *KMCM* with a reduced horizontal and an increased vertical resolution, i.e. T29 and 60 hybrid layers from 990 to 0.0003 mb. Other modifications of this T29/L60 model configuration are as follows.

In the middle atmosphere we employ a more realistic equilibrium temperature (see white contours in Fig. 20a) which resembles the radiatively determined state proposed by Shine (1987). Furthermore, vertically extended profiles for the relaxation time and the horizontal diffusion coefficient are introduced (Fig. 18). The relaxation time τ is 17 days in the troposphere, it increases to 45 days around the 100 mb level and slopes down to 7 days in the upper stratosphere and mesosphere. This profile differs from that used in Becker and Schmitz (2002) by including a considerably long relaxation time in the lower stratosphere. Such a feature is known from radiation model calculations (e.g., Gille and Lyjak, 1986) and it has also been accounted for by Dunkerton (1991) within an idealized model. The modification leads to somewhat enhanced transient planetary wave activity

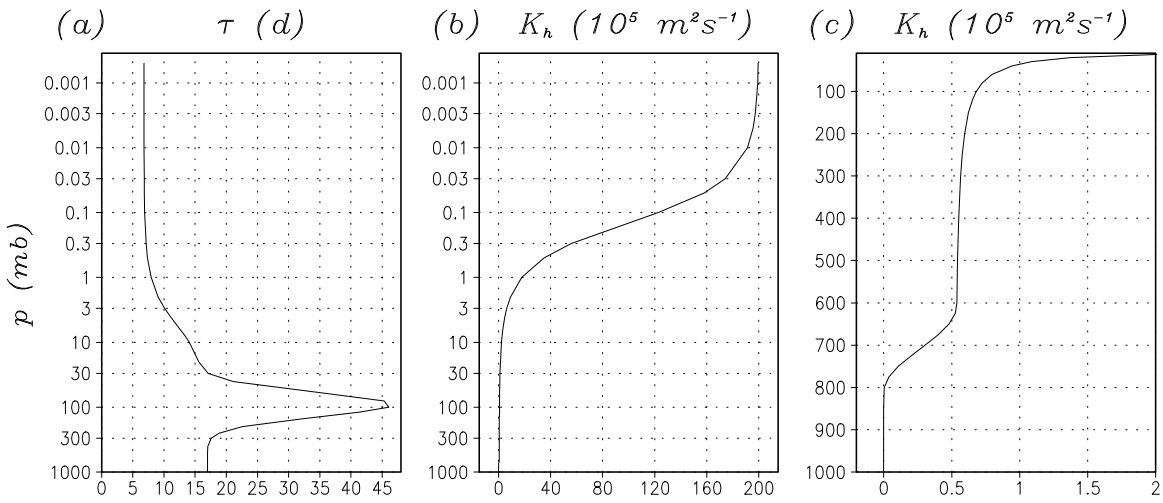

Figure 18: (a) Relaxation time τ and (b) horizontal diffusion coefficient K_h as functions of $\eta\times 1013$ mb for the T29/L60 model configuration. The extra panel (c) shows the tropospheric and lower stratospheric branch of K_h.

in the middle atmosphere. The horizontal diffusion coefficient is about 0.55×10^5 m^{2}s^{-1} in the upper troposphere and amounts to 2×10^7 m^{2}s^{-1} in the MLT.

Gravity wave effects are parameterized according to saturation theory as described in the previous section. We assume a family of $j_0 = 14$ individual gravity waves. For simplicity, wave-wave interactions are neglected. The vertical flux of horizontal momentum owing to IGWs, the associated pressure flux, and the wave-induced turbulent diffusion coefficient are written as

$$\mathbf{F} := j_0^{-1} \sum_{j=1}^{j_0} F_j \, \mathbf{e}_{\alpha_j} \quad \text{with} \quad \mathbf{e}_\alpha := \cos\alpha \, \mathbf{e}_x + \sin\alpha \, \mathbf{e}_y \tag{6.30}$$

$$F_p = j_0^{-1} \sum_{j=1}^{j_0} (c_j - \bar{u}_j) \, F_j \quad \text{with} \quad \bar{u}_j := \mathbf{v} \cdot \mathbf{e}_{\alpha_j} \tag{6.31}$$

$$K_{z\,igw} := j_0^{-1} \sum_{j=1}^{j_0} \mathcal{D}_j + \nu_{bg}(\eta) \, . \tag{6.32}$$

The α_j denote the individual azimuths of propagation. The corresponding horizontal phase speeds are $c_j > 0$. Then, $j_0^{-1} F_j \mathbf{e}_{\alpha_j}$ and $j_0^{-1} \mathcal{D}_j$ are the individual wave contribution to the momentum flux and the diffusion coefficient. The pressure flux (6.31) follows from the first theorem of Eliassen and Palm (6.18). For the sake of completeness, the definition (6.32) also includes an additional background diffusion similar to the profile used by Becker and Schmitz (1999, their Fig. 3). In the MLT, this additional term is negligible against the IGW-induced diffusion coefficient.

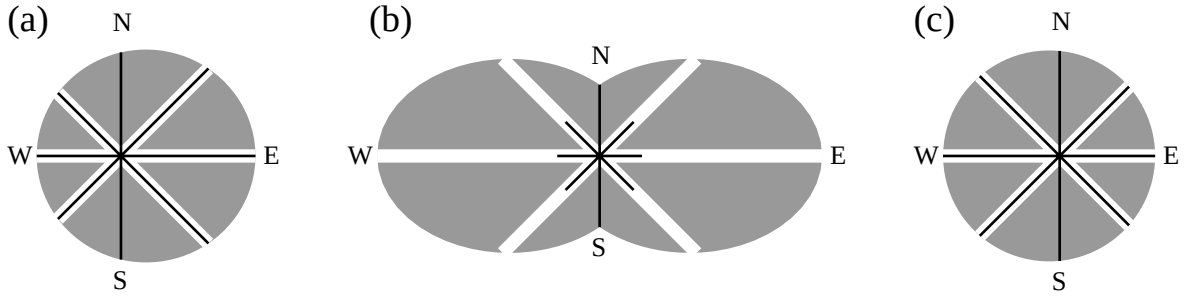

Figure 19: Graphical representation of gravity wave parameters: (a) Horizontal wave numbers k_j, (b) phase speeds c_j, and (c) amplitudes $\tilde{u}_j$. The source spectrum consists of 14 individual waves each of which is represented by either a thin black line or a thick white line. These waves are distributed over 8 equidistant different azimuths. Each one wave propagates northward and southward while each two waves propagate in the other directions. The scaling is such that maximum components in (a), (b), and (c) are 1.63×10^{-5} m^{-1}, 32.8 ms^{-1}, and 1.04 ms^{-1}, respectively.

Chapter 4 has already provided the general finite-difference scheme to incorporate any such gravity wave parameterization in a hybrid coordinate model. We emphasize that the energy deposition must not be computed from (6.28) if a precise energy conservation is desired. For the present hybrid coordinate model, $\mathbf{F}$ and $K_{z\,igw}$ are specified on half model layers. The pressure flux (6.31) is defined on half layers using $\mathbf{v}_{l+1/2} := (\,\mathbf{v}_{l+1} + \mathbf{v}_l\,)/2$.

In accordance with the analysis of the previous section we account for the wave entropy flux by means of the vertical diffusion term μ_z. We assume an effective Prandtl number of 1 for the combined entropy flux owing to the gravity waves themselves and the wave-induced turbulent diffusion of the mean flow. That is, the vertical diffusion coefficient K_z in Eqs. (4.11)-(4.13) is the sum of (A38) and (6.32).

The gravity waves are launched at the initial half level z_0 which is located around 170 mb. Writing the height argument in brackets, we have from (6.13)

$$F_j[z_0] = \frac{k_j\,\rho_{00}}{2\,N[z_0]}\;\tilde{u}_j^3 =: F_{j\,0} \;>\; 0\,. \tag{6.33}$$

Here, ρ_{00} and N are a surface reference density and the Brunt-Väisälä frequency of the model's reference state defined in appendix A.2. The velocities $\tilde{u}_j > 0$ and the horizontal wave numbers $k_j > 0$ are gravity wave parameters.

Critical levels z_{cj} are implicitly defined by $\bar{u}_j - c_j = 0$ above which we have $F_j = 0$. Since the real part of the vertical wave numbers must be negative for upward energy flux, individual waves with $\bar{u}_j - c_j \;>\; 0$ are also removed from the spectrum. If the

condition $\bar{u}_j - c_j \geq 0$ is not fulfilled somewhere above the initial level, z_{cj} is identified with the half layer between the uppermost two full model layers.

Below the critical levels, the IGWs may reach static instability at the breaking levels z_{bj} implicitly defined via Eq. (6.21). To solve (6.21) for the breaking levels, we assume a scale height of $H = 6.44$ km which corresponds to a background temperature of 220 K in the middle atmosphere consistent with the model's reference state (Fig. 32a). If the lhs of (6.21) does not change sign between z_0 and z_{cj} for an individual wave, we formally set $z_{bj} = z_{cj}$.

Between z_{bj} and z_{cj}, the wave momentum fluxes can be calculated according to (see Eq. (6.24))

$$F_{bj} := \rho\, k_j\, (\, 2\, N\,)^{-1}\, (\, c_j - \bar{u}_j\,)^3\,. \tag{6.34}$$

In a 3D dynamical model, F_{bj} may increase with height even at or above the breaking level z_{bj} . In this case it is appropriate to keep F_j constant with height and to neglect the individual wave contributions to the diffusion coefficient (e.g., McFarlane, 1987). Letting Δz be the height increment between adjacent half model layers, the present implementation of the Lindzen scheme can be summarized as:

$$F_j[z] = \begin{cases} 0 & \text{for } z < z_0 \\ F_{j0} & \text{for } z_0 \leq z \leq z_{bj} \\ F_{bj} & \text{for } z_{bj} < z < z_{cj} \text{ and } F_{bj}[z] \leq F_j[z-\Delta z] \\ F_j[z-\Delta z] & \text{for } z_{bj} < z < z_{cj} \text{ and } F_{bj}[z] > F_j[z-\Delta z] \\ 0 & \text{for } z \geq z_{cj}. \end{cases} \tag{6.35}$$

$$\mathcal{D}_j[z] = \begin{cases} 0 & \text{for} \quad z \geq z_{cj} \\ \\ F_{bj} \times (\,(\,c - \bar{u}_j\,)\,/\,H \,+\, 3\,\partial_z\,\bar{u}_j\,)\,/\,(\,\rho\, N^2\,) & \\ \qquad \text{for} \quad z_{bj} \leq z < z_{cj} \quad \text{and} \quad F_{bj}[z] \leq F_j[z-\Delta z] & \\ \\ 0 \qquad \text{for} \quad z_{bj} \leq z < z_{cj} \quad \text{and} \quad F_{bj}[z] > F_j[z-\Delta z] & \\ \\ \mathcal{D}_j[z_{bj}] \times \exp\{\,(\,z - z_{bj}\,)\,/\,3\,H\,\} & \\ \qquad \text{for} \quad z_0 \leq z < z_{bj} & \\ \\ 0 \qquad \text{for} \quad z < z_0\,. \end{cases} \tag{6.36}$$

This implementation differs from that used in Becker and Schmitz (2003) by a sharper decay of $\mathcal{D}_j$ below the breaking level (Holton, 1982). Figure 19 summarizes the actual choices for k_j, c_j, and $\tilde{u}_j$. The 14 individual waves propagate in 8 equidistant azimuths. In each of the azimuths 0^0, 45^0, 135^0, 180^0, 225^0, and 315^0 there are two waves that differ

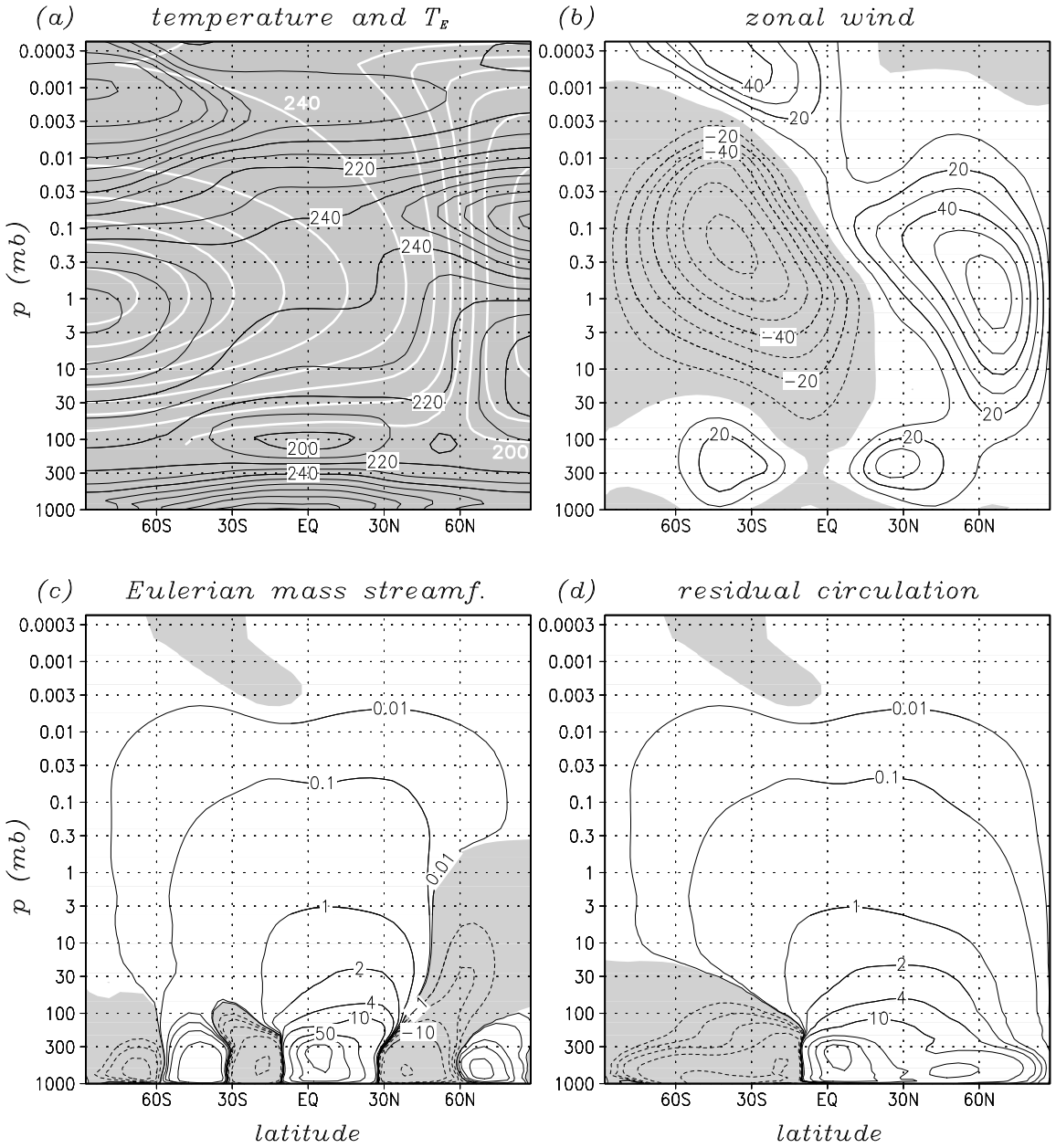

Figure 20: Zonal-mean climatology of the T29/L60 version of *KMCM* (a) Temperature (black contours, interval 10 K) and equilibrium temperature T_E (white contours, interval 10 K, only the 200 and 240 K contours are labeled). (b) Zonal wind (contour interval 10 ms^{-1}). (c) Eulerian mass streamfunction (contours $0.01, 0.1, \pm 1, \pm 2, \pm 4, \pm 10, \pm 50, 100, 150 \times 10^9$ kgs^{-1}). (d) Same as (c), but for the residual mass streamfunction. In panels (b)-(d), zero contours are not drawn, and negative values are shaded.

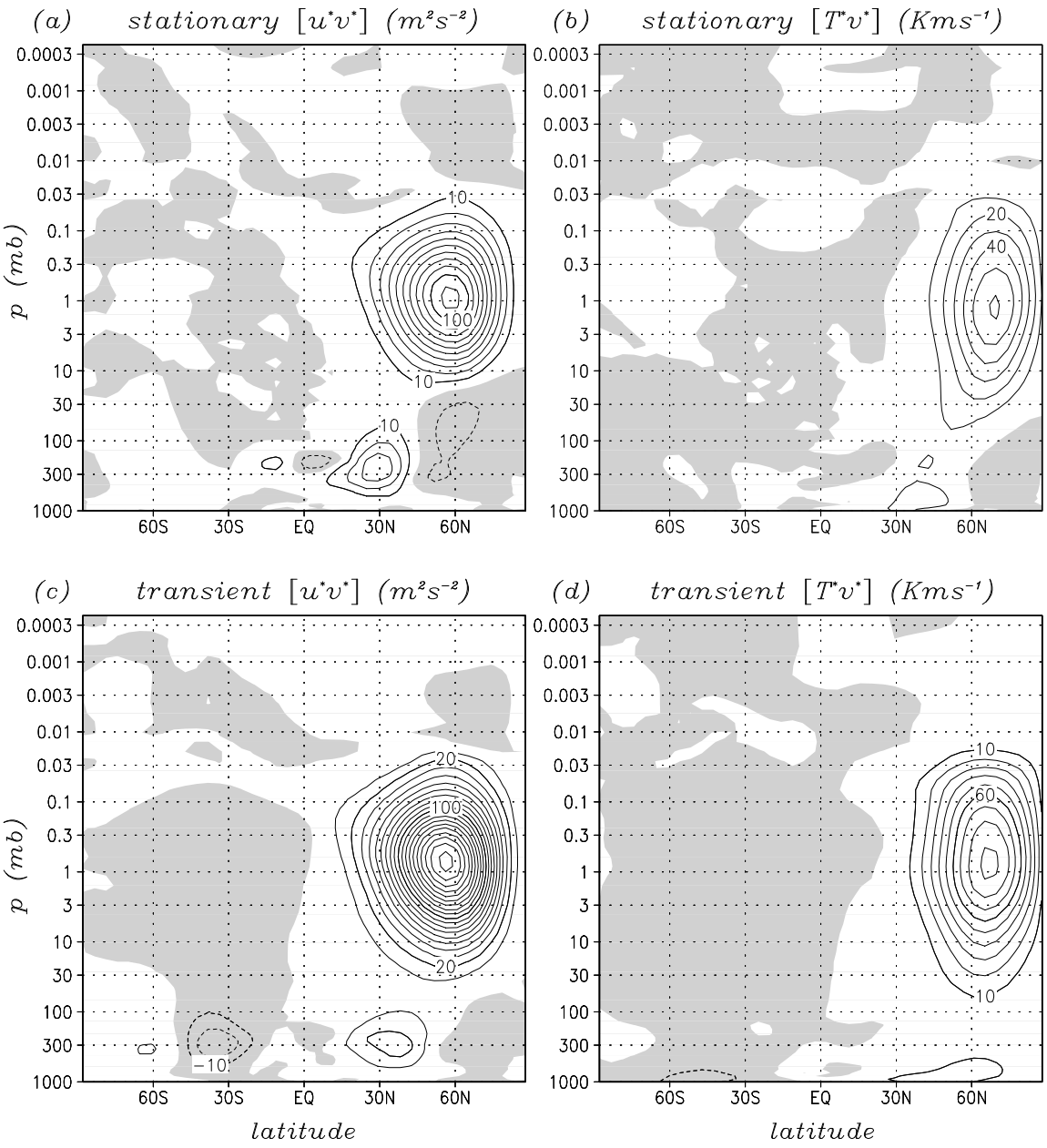

Figure 21: Zonal-mean climatology of the T29/L60 version of *KMCM*. (a) Stationary eddy momentum flux (contour interval 10 m^2s^{-2}). (b) Stationary eddy heat flux (contour interval 10 Kms^{-1}). (c),(d) Same as (a),(b) but for the transient wave fluxes. Zero contours are not drawn, and negative values are shaded.

with respect to their phase speeds c_j while having the same horizontal wave numbers k_j and initial amplitudes $\tilde{u}_j$. Each of the azimuths 90^0 and 270^0 contains one wave. Note that the scaling factor j_0^{-1} can as well be avoided by redefining the horizontal wave numbers as $j_0^{-1}k_j$. In fact, each gravity wave effect (momentum deposition, energy deposition, turbulent diffusion coefficient) proves to be proportional to any efficiency factor applied to the horizontal wave numbers.

At present it is hardly known how the excitation of IGWs depends in detail on the large-scale atmospheric flow. Therefore, it is suitable to employ a fixed and horizontally uniform source spectrum.

In the following we inspect a long-term model run (1200 day time series) including full forcing of planetary waves by orography and the heating functions Q_c and Q_m (Becker and Schmitz, 2003). As in the previous chapter, this simulation is referred to as *control* run. The zonal-mean climatology of the control run is documented in Figs. 20 and 21. The longitudinal distributions of stationary and transient waves in the troposphere and stratosphere are similar to those obtained in the T42/L24 model version (Fig. 10) and are therefore not shown.

6.3 Dynamical aspects of the heat budget in the middle atmosphere

Let us concentrate on the simulated heat budget of the mesosphere in the climatological zonal mean. Figure 22 shows a corresponding graphical representation. First of all we compare the dynamic heating (panel f) with the parameterized heating (panel e). The former is defined as adiabatic heating plus advection by the resolved flow, while the latter represents the sum of temperature relaxation, dissipation of the mean flow, energy deposition owing to IGWs, and diffusion. The satisfactory balance between dynamic heating and parameterized heating indicates that the model's aliasing errors are small. The diabatic heating by temperature relaxation (panel (a)) is quantitatively consistent with other estimates for the radiative heating in the middle atmosphere during the solstices (Gille and Lyjak, 1986; Berger and von Zahn, 1999). Figures 22a-d reveal that, in the upper mesosphere, the parameterized heating is a residual of several contributions. Particularly in the region of gravity wave breaking, diffusion of heat and energy deposition (Figs. 22c,d) are of the same order of magnitude as temperature relaxation.

The energy deposition (Fig. 22c) is reminiscent of the observed asymmetry between the summer and the winter mesosphere as deduced from rocket-borne measurements (Lübken, 1997a,b); it reflects corresponding summer-winter differences in gravity wave saturation as anticipated by Lindzen (1981). Note that the energy deposition does not represent

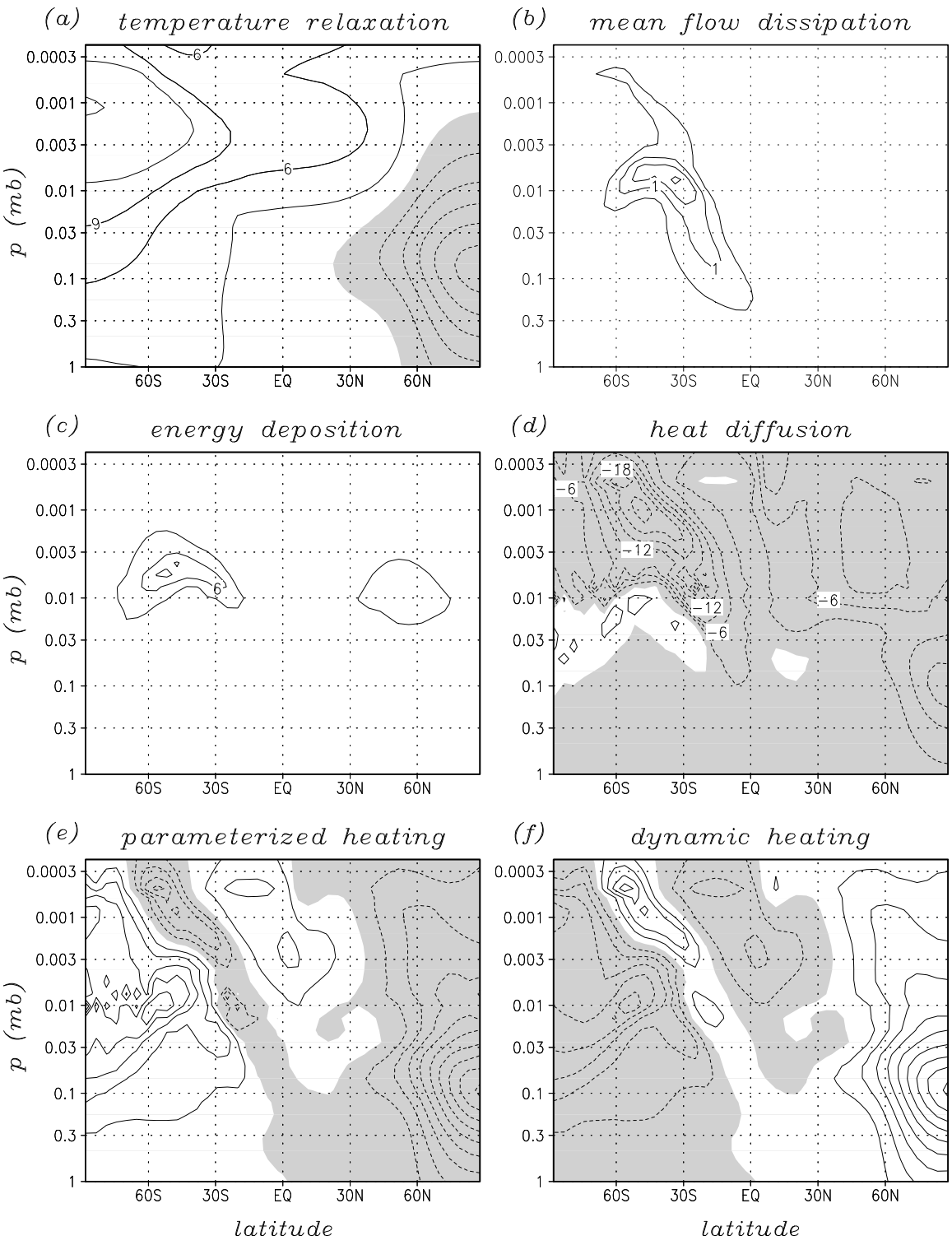
(a) temperature relaxation
(b) mean flow dissipation
(c) energy deposition
(d) heat diffusion
(e) parameterized heating
(f) dynamic heating
p (mb)
0.0003
0.001
0.003
0.01
0.03
0.1
0.3
1
60S
30S
EQ
30N
60N
latitude
-6
6
-9
1
-18
-12

Figure 22 (previous page): Simulated heat budget of the mesosphere in the climatological zonal mean. (a) Radiative heating as mimicked by temperature relaxation. (b) Dissipation due to vertical and horizontal momentum diffusion of the mean flow, i.e. $\epsilon_z+\epsilon_h$. (c) Energy deposition (Eq. (2.57)). (d) Heat diffusion (see Eq. (2.56)). (e) Net parameterized heating defined as the sum of (a)-(d). (f) Adiabatic heating plus advection due to the resolved planetary-scale flow, abbreviated as *dynamic heating*. The contour interval is 0.5 Kd^{-1} in panel (b) and 3 Kd^{-1} in all other panels. Zero contours are not drawn, and negative values are shaded.

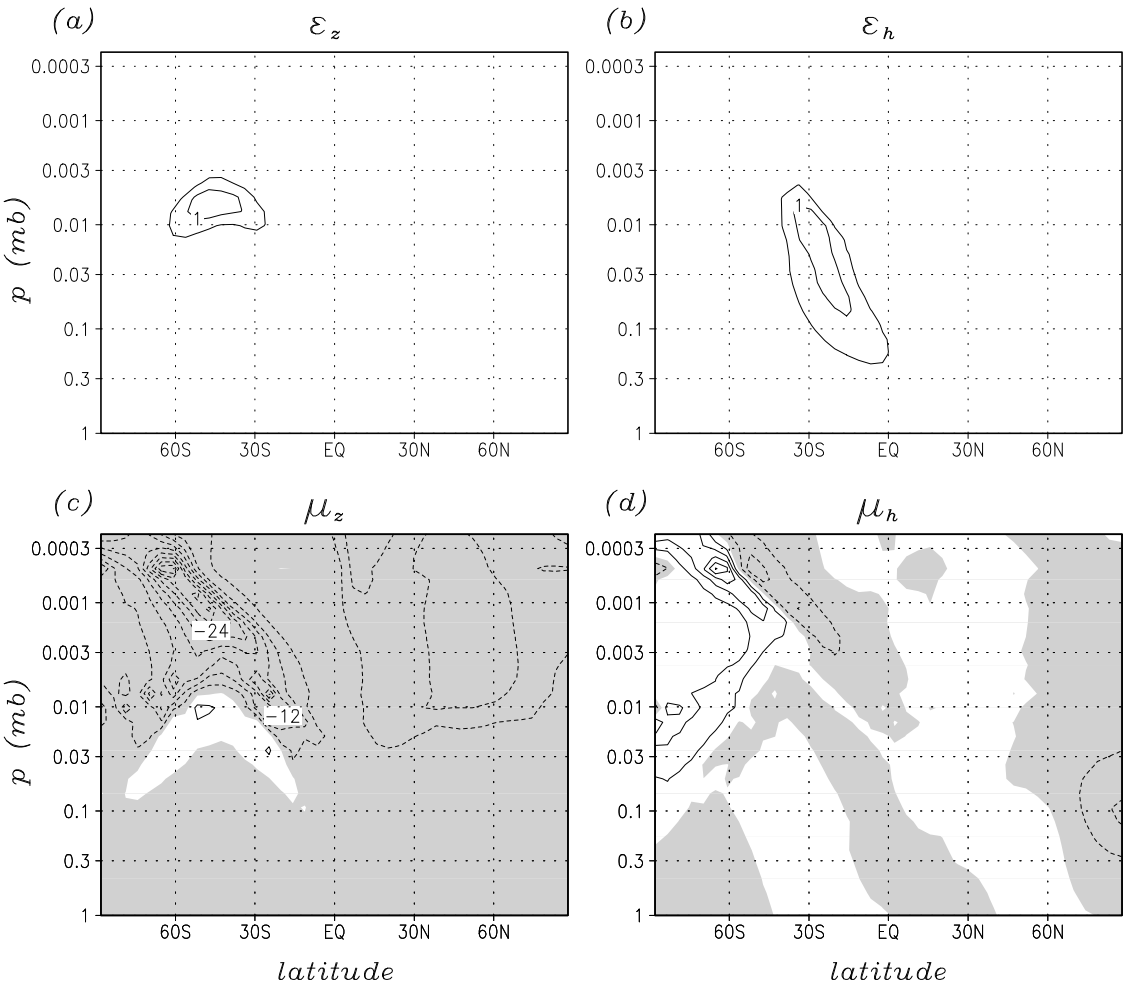

Figure 23: Specific contributions to the heat budget of the mesosphere owing to turbulent diffusion of the mean flow in the climatological zonal mean. (a),(b) Dissipation owing to vertical and horizontal momentum diffusion (see Eqs. (3.10),(3.9), contour interval 0.5 Kd^{-1}). (c) Vertical diffusion of potential temperature and (d) horizontal diffusion of temperature (see Eq. (2.56), contour interval 4 Kd^{-1}). Zero contours are not drawn, and negative values are shaded.

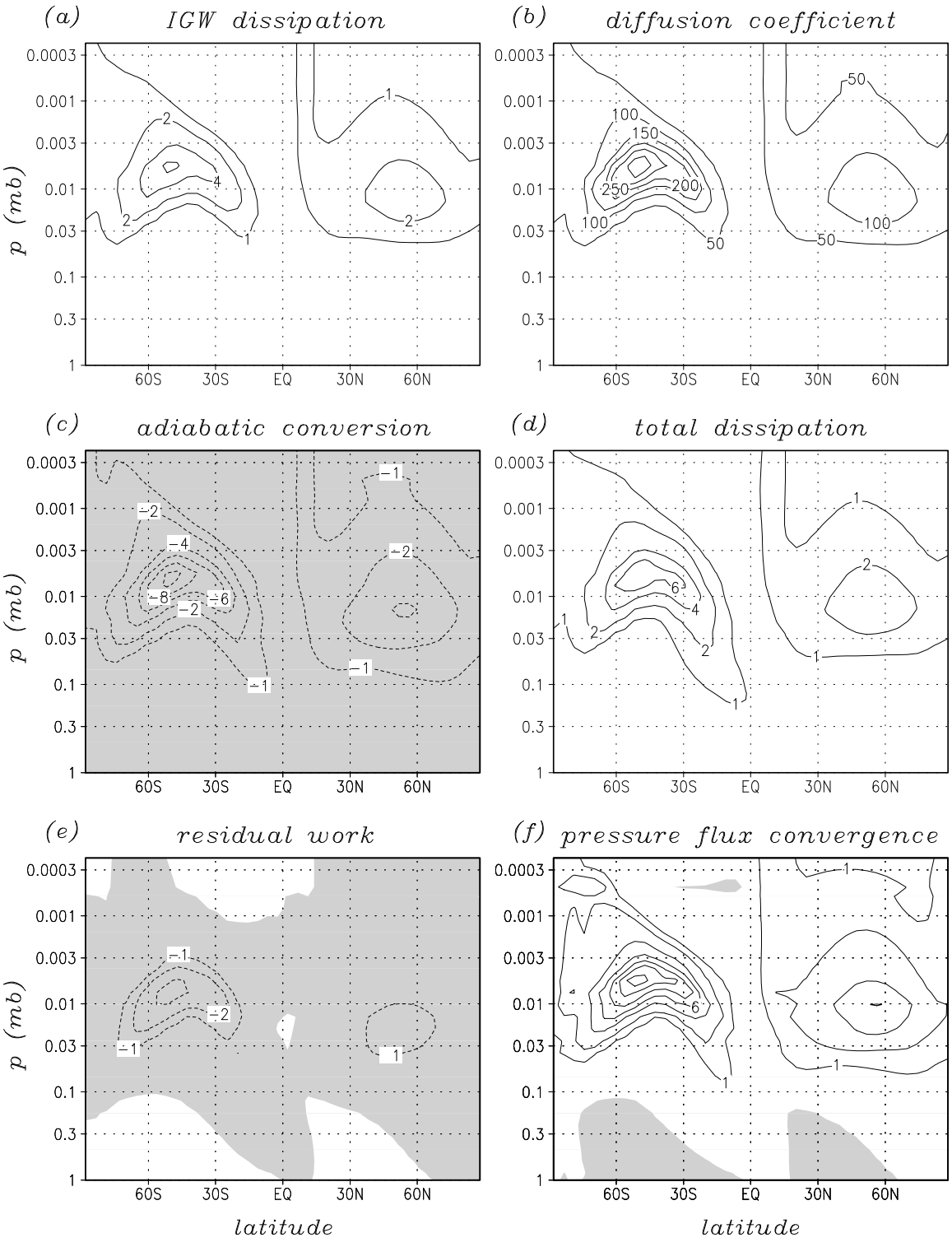
(a) IGW dissipation
(b) diffusion coefficient
(c) adiabatic conversion
(d) total dissipation
(e) residual work
(f) pressure flux convergence
p (mb)
0.0003
0.001
0.003
0.01
0.03
0.1
0.3
1
60S
30S
EQ
30N
60N
latitude

Figure 24 (previous page): Specific IGW contributions to heat budget of the mesosphere in the climatological zonal mean. (a) Dissipation of IGW kinetic energy (6.37). (b) IGW-induced vertical diffusion coefficient (6.32). (c) Adiabatic conversion of mean enthalpy into IGW kinetic energy. (d) Total dissipation (defined as the sum of Figs. 22b and 24a). (e) Residual work (second Eq. (2.57)). (f) Pressure flux convergence. Contours are drawn for $\pm 1, \pm 2, \pm 4, \pm 6, \ldots$ Kd^{-1}, and negative values are shaded.

the turbulent dissipation even though such an interpretation is sometimes suggested as already mentioned in section 1.3.

The dissipation and the heat diffusion of the mean flow consist of two terms each. These are due to vertical and horizontal diffusion (section 2.4). Figure 23 depicts these individual parts of the heat budget (note the different contour intervals in the upper and lower panels). The vertical and horizontal contributions to the dissipation of the mean flow have similar magnitudes. According to Fig. 23c, vertical diffusion of potential temperature μ_z cools the MLT. This is expected for a statically stable stratification. There is also heating due to μ_z between about 0.1 and 0.01 mb (60 to 80 km) in the summer MLT. This heating marks a sharp spatial concentration of the breaking levels. In the northern winter mesosphere, such a diffusive heating is generally not visible because the breaking levels are distributed over a wider altitude range (Becker and Schmitz, 2003). For the present choice of an effective Prandtl number 1, μ_z dominates the direct IGW heating rates that are explicitly accounted for in the model. We obtain maximum cooling rates of more than -30 Kd^{-1} in summer and about -10 Kd^{-1} in winter (Fig. 23c). Horizontal diffusion of temperature, μ_h (see Eq. (2.56)), gives maximum contributions of about ± 10 Kd^{-1} around the summer mesopause (Fig. 23d).

The maximum dissipation associated with momentum diffusion of the mean flow is about 2 Kd^{-1} (Fig. 22b). This value is consistent for instance with Fritts and Luo (1995, see also references therein) who noted that typical dissipation values of about 2 Kd^{-1} in the summer MLT lie well within the wide range of experimental and theoretical estimates. Nevertheless, the simulated dissipation is too weak by almost one order of magnitude in comparison with the more recent observational results of Lübken (1997a). This apparent discrepancy has been anticipated in section 2.4, where it has been stressed that the dissipation of gravity wave kinetic energy ϵ_{igw} is not explicitly accounted for in the thermodynamic equation of the model. Rather, the model includes the residuum of ϵ_{igw} and the wave-generated adiabatic conversion of mean enthalpy into wave kinetic energy. Hence, we have not proven yet whether the model simulation is consistent with in-situ measurements of Lübken, that is, whether the model can reproduce the observed frictional heating in the mesosphere.

An essential element of Lindzen's saturation theory is that the IGW-induced turbulent diffusion coefficient and the wave-mean flow interactions are unambiguously linked together. Such a relationship is not provided by other gravity wave theories like that of Hines (1997) for instance. Moreover, since Lindzen's theory explicitly describes the dynamics of the individual gravity waves, the frictional heating generated by these waves can be calculated. According to (6.26) and neglecting wave-wave interactions, the dissipation of gravity wave kinetic energy yields for the present parameterization

$$\epsilon_{igw} \;=\; \frac{1}{2}\, K_{z\,igw}\, N^2 \,. \tag{6.37}$$

Figure 24a shows the model estimate of (6.37). The dissipation of gravity wave kinetic energy reflects the turbulent vertical diffusion coefficient $K_{z\,igw}$ which is shown in Fig. 24b. Figures 24a and 22c are roughly consistent with the theoretical relationship $E = 2\,\epsilon_{igw}$ derived in section 6.1.2. Comparing Fig. 24a to Figs. 23a,b yields that, in the MLT, (6.37) gives the dominant contribution to the total dissipation $\epsilon_{igw} + \epsilon_h + \epsilon_z$. The model estimate of the total dissipation (Fig. 24d) amounts to 7 Kd^{-1} in summer. Such a value is too weak by about a factor of 2 in comparison with results of Lübken (1997a,b) for the average of observed summer MLT dissipation rates. Nevertheless, both experimental and model estimate are of same order of magnitude.[2]

It is worthwhile to emphasize that the computational result of the total dissipation has been obtained without adjusting the direct heating rates associated with gravity wave breaking by additional parameters. With the setting of gravity wave parameters we have specified the individual wave momentum fluxes (or equivalently the energy fluxes) launched around the tropopause, but nothing else.[3] (The only additional parameter of the present gravity wave parameterization is the effective Prandtl number. The model sensitivity to the choice of this parameter will be addressed in the next section.) As usual, the IGW source has been tuned such that the model generates a reasonable IGW-driven residual circulation in the mesosphere, including the reversal of the zonal-mean zonal wind in both hemispheres and the generation of a cold summer mesopause (Fig. 20). As soon as these objectives are achieved, the dissipation of gravity wave kinetic energy is found to be of the order of magnitude predicted by the aforementioned observational results of Lübken.

According to the analysis presented in chapter 2, also the adiabatic conversion of mean enthalpy into gravity wave kinetic energy (see Eq. (2.58)) can be assessed. The convention

[2]In Becker and Schmitz (2002), stronger dissipative heating rates were predicted by the model. I have recognized that the former result was due to overestimating the wave-induced diffusion coefficient $K_{z\,igw}$ via the vertical discretization method. This part of the code has been improved.

[3]Additional 'fudge factors' are introduced in the scheme of Hines (1997) for instance in order to tune the energy deposition and the diffusion coefficient independently from the momentum deposition.

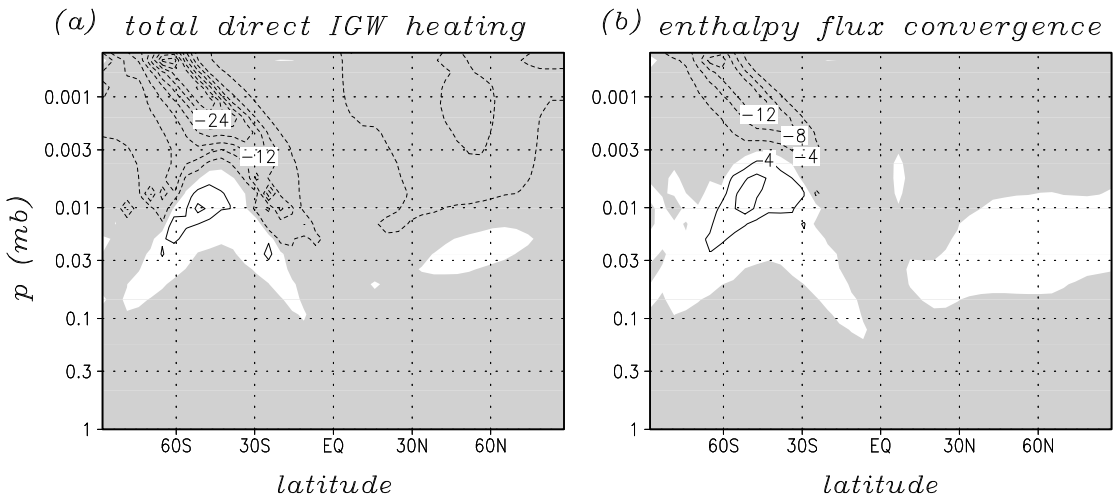

Figure 25: (a) Sum of all direct heating rates owing to gravity waves, $E + \mu_z + \epsilon_z$, and (b) the wave enthalpy flux convergence (contour interval 4 Kd^{-1}, zero contours are not drawn, negative values are shaded). The latter is equal to the pressure flux convergence (Fig. 24f) plus the entropy flux convergence (see Eq. (2.37)) which, for the present choice of an effective Prandtl number 1, is given by $\frac{1}{2}\,\mu_z$.

is such that the conversion is negative if gravity kinetic energy is generated. Figure 24e shows the residual work, which together with the pressure flux convergence (Fig. 24f) gives rise to the energy deposition (Fig. 22c). It has been anticipated in Becker and Schmitz (2002) that the residual work is generally negative in the MLT. This is confirmed by Fig. 24e. Hence, the adiabatic conversion term, $W_{res} - \epsilon_{igw}$ (Fig. 24c), overcompensates the dissipation. This relationship provides a reasonable explanation to the question raised by Lübken (1997a), namely what process balances the observed strong dissipative heating in the summer MLT.

Since the wave entropy flux convergence behaves like a mean flow diffusion, it generates heating around the breaking levels and cooling farther above, at least in the summer MLT (see Fig. 23c). Also the total simulated heating rate owing to gravity waves (Fig. 25a) or the wave enthalpy flux convergence (Fig. 25b, calculated according to Eq. (2.46)) resemble this structure, with the regions of heating being more pronounced due to the pressure flux convergence. Hence, the heating/cooling pattern shown in Fig. 25a is dominated by the vertical entropy flux generated by the waves and by the wave-induced turbulent diffusion.

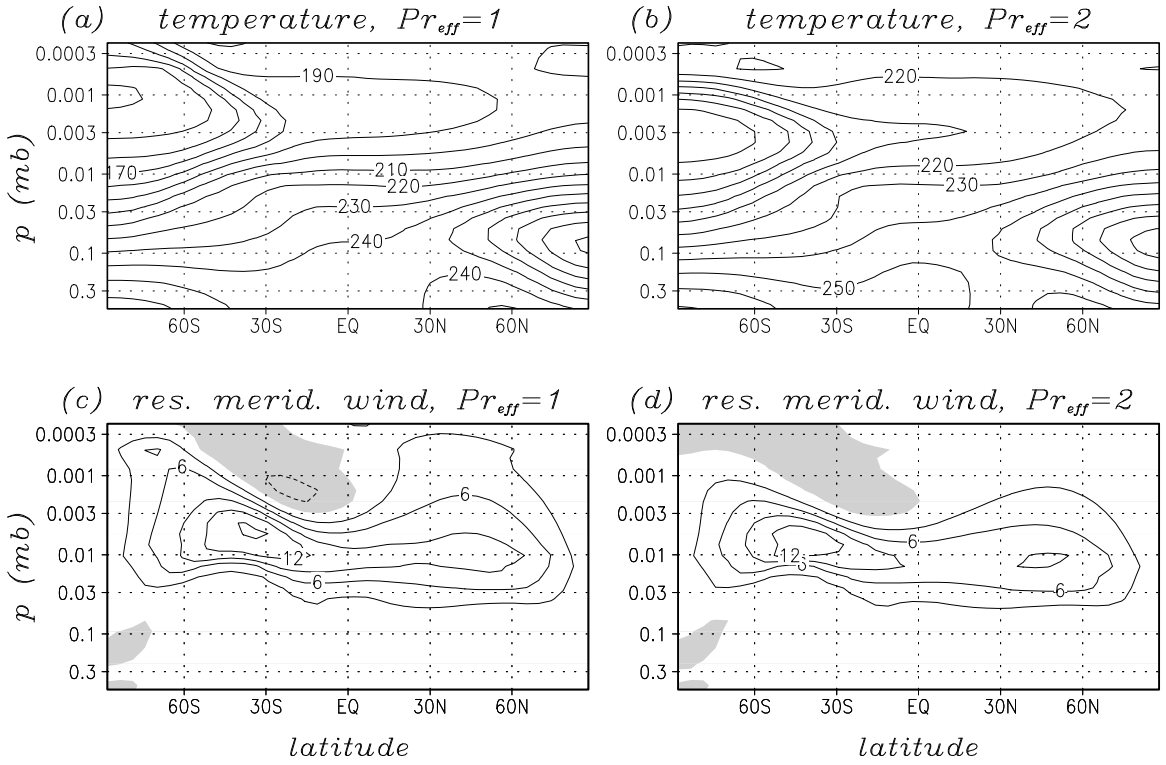

Figure 26: Zonal-mean temperature and residual meridional wind in the control run (a,c) and in the perturbation run with an effective Prandtl number of 2 assumed for vertical diffusion in the MLT (b,d). The contour intervals are 10 K (a,b) and 3 ms^{-1} (c,d). Zero contours are not drawn, and negative values are shaded.

6.4 Sensitivity experiments

6.4.1 Role of the effective Prandtl number

The Prandtl number for vertical diffusion of potential temperature in the MLT has long been the most ambiguous parameter of IGW parameterizations. All other parameters are more constrained in order to achieve a reasonable model climatology with regard to the zonal-mean zonal wind and the residual circulation. Within the framework of Lindzen's saturation theory it has been shown that the effective Prandtl number assumed for the planetary-scale flow should not exceed a value of 2 (section 6.1). This result comes about because the entropy flux convergence owing to gravity wave-mean flow interaction – a term that is usually ignored – is indeed important and formally corresponds to a vertical diffusion with a Prandtl number of 2. It thus follows that the effective Prandtl number which scales the combined entropy flux owing to the gravity waves themselves and the wave-induced turbulence must lie between $\frac{2}{3}$ and 2. If the lower bound is used,

both the action of the wave-induced turbulence on the background stratification and the wave entropy flux are fully included; if the effective Prandtl number is equal 2, only the wave entropy flux is accounted for. In the control simulation we have assumed an intermediate effective Prandtl number of 1. It appears however worthwhile to assess the model sensitivity to the choice of this parameter. Therefore, an additional long-term integration has been performed, employing an effective Prandtl number of 2 for vertical diffusion in the MLT. More precisely, the vertical diffusion coefficient in Eq. (4.13) has been set equal to the sum of (A38) and $K_{z\,igw}/2$. The model setup of the control run has been maintained otherwise.

Figure 26 shows the MLT temperatures and residual meridional winds in the control run (lhs panels) and in the perturbation run with the higher effective Prandtl number (rhs panels). Figures 26a,b indicate that, due to a doubling of the Prandtl number, the summer mesopause is heated up by about 30 degrees and shifted to lower altitudes. Furthermore, its vertical slope with latitude (e.g., Berger and von Zahn, 1999) flattens. Temperatures also rise throughout the winter mesosphere with an averaged signal of about 20 degrees. These temperature changes reflect mainly the lower diabatic cooling by vertical diffusion of potential temperature. However, Figs. 26c,d reveal that also the gravity wave-driven residual circulation in the MLT is significantly reduced, indicating that gravity effects become generally weaker if we simply increase the Prandtl number. As a result, the present perturbation run yields a somewhat weaker diffusion coefficient and a somewhat weaker total dissipation rate with a maximum of 6 Kd^{-1} in the summer MLT (not shown). For the larger effective Prandtl number we would have to adjust the gravity wave source in order to maintain the strength of the IGW-driven residual circulation and a cold summer mesopause. This would in turn reestablish stronger dissipation rates.

6.4.2 Impact of orography and land-sea heating contrasts

It has been mentioned in section 1.2 that the IGW-controlled general circulation of the mesosphere is highly sensitive to the forcing of planetary-scale waves in the troposphere. The mechanism behind this at first sight unexpected sensitivity can be investigated on the basis of the present model in the following way. First we define the corresponding aquaplanet model by substituting the heating functions Q_c and Q_m (see section 5.2), and orography Φ_s by their zonal averages $[Q_c]$, $[Q_m]$, and $[\Phi_s]$.[4] Then, the remote effects of orography and land-sea heating contrasts on the general circulation of the middle atmosphere can systematically be assessed by comparing the control run to the aquaplanet run. We furthermore assume that the control and the aquaplanet simulation approxi-

[4] The zonal means of Φ_s and Q_m formally deviate from aquaplanet conditions. However, their effects are hardly visible in the climatology of the aquaplanet simulation.

mately represent the middle atmospheric general circulation during boreal and austral winter, respectively. This will allow for some instructive comparison of present model results with recent observational data for the northern and southern summer MLT.

Orography and land-sea heating contrasts in the winter troposphere strongly induce the activity of planetary-scale Rossby waves, particularly in the stratosphere. As a result, the stratospheric westerly jet becomes weaker, more variable, and warmer. Such features are well known from the observed north-south asymmetry between boreal and austral winter. Also the differences in the control run from the aquaplanet run reasonably reproduce this behavior. This is demonstrated in Figs. 27 and 28. Figure 27 shows the zonal-mean zonal wind and temperature in the aquaplanet run together with the differences between the control run and the aquaplanet run. Figure 28 shows the standard deviations of the zonal-mean zonal winds for both model experiments. In the control case, the variability is quantitatively consistent with boreal winter observations (Randel, 1992).

As a result of the more variable and reduced polar night jet in the control run, gravity wave saturation is distributed over a greater depth and drops on average in altitude. Hence, gravity wave drag, turbulent diffusion, and energy deposition in the winter mesosphere are strongly diminished as a remote effect of stationary wave forcing in the lower troposphere. This mechanism has been discussed in detail by Becker and Schmitz (2003). The reduced gravity wave forcing is balanced by a weaker residual circulation in the winter mesosphere. This accounts for the lower polar night temperatures above and around the stratopause in the control run, as is visible in Fig. 27c for the altitude range between about 1 and 0.01 mb. The model also reveals that the entire summer-to-winter-pole residual circulation is reduced (Fig. 29). Thus, stationary wave forcing in the winter troposphere can remotely affect winds and temperatures around the summer mesopause (see Figs. 27c,d).

North-south asymmetries in the summer MLT region have been investigated by Huaman and Balsley (1999) and by Dowdy et al. (2001) on the basis of observations. These authors find meridional wind asymmetries which are fully consistent with Fig. 29 (see Dowdy et al., 2001, Fig. 2). Furthermore, the zonal wind asymmetries obtained by Huaman and Balsley (Fig. 4 in their paper) are consistent with Fig. 27d (see also Becker and Schmitz, 2003, Fig. 11). Huaman and Balsley also suggested that the austral summer mesopause is a few degrees warmer than its boreal summer counterpart. Such a hypothesis is supported if we compare Fig. 20a to Fig. 27a. Note, however, that Lübken et al. (1999) found no significant differences in the temperature profiles observed in the austral and boreal summer MLT. Therefore, at present there appears to be no observational evidence for a significant north-south asymmetry in summer MLT temperatures.

Nonetheless we can conclude that the summer mesospheric heat budget in the con-

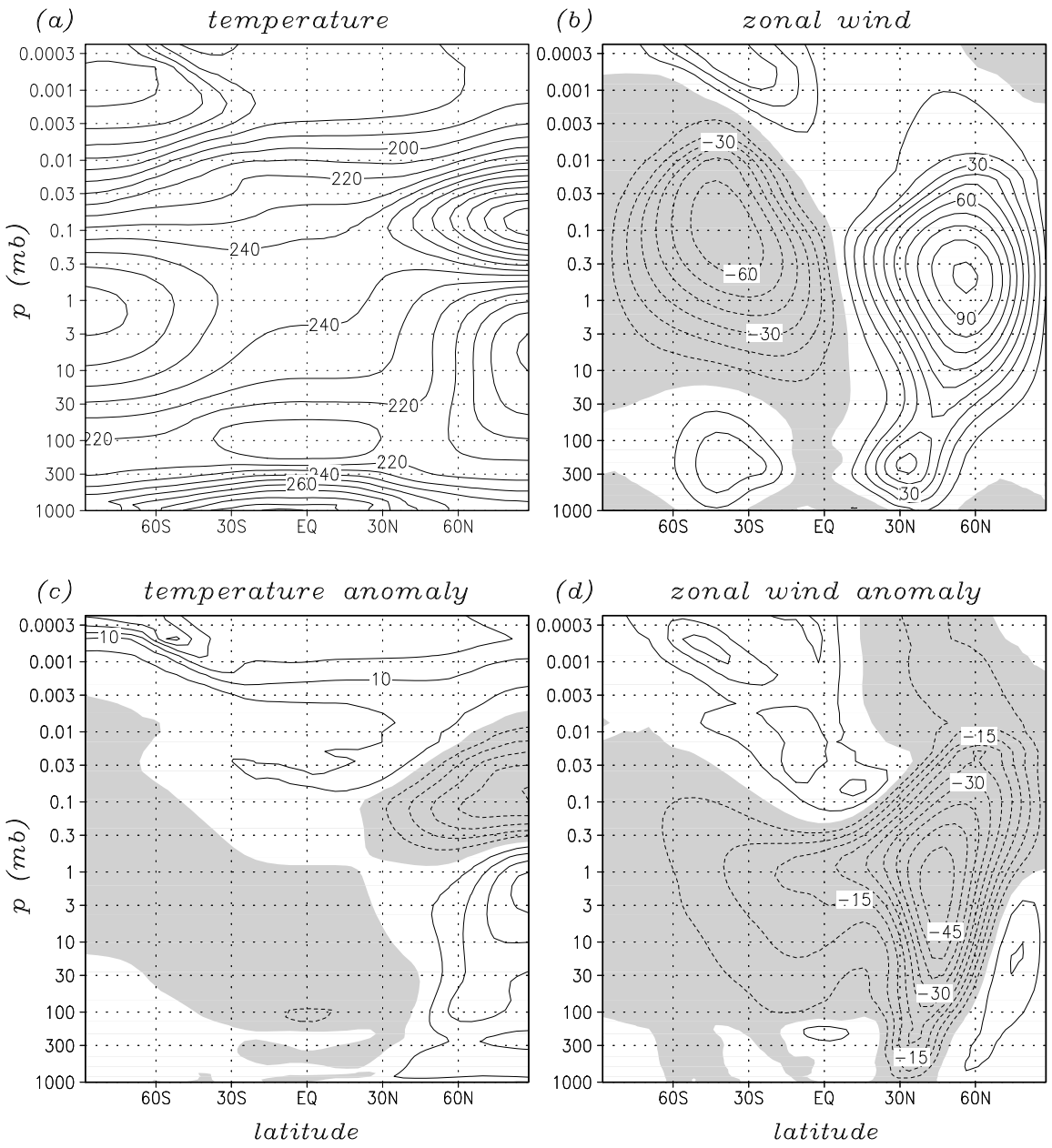

Figure 27: (a),(b) Climatological zonal-mean temperature and zonal wind in the aquaplanet simulation (contour intervals 10 K and 10 ms^{-1}). (c),(d) Corresponding differences in the control run from the aquaplanet run (contour intervals 5 K and 5 ms^{-1}). Zero contours are not drawn, and negative values are shaded.

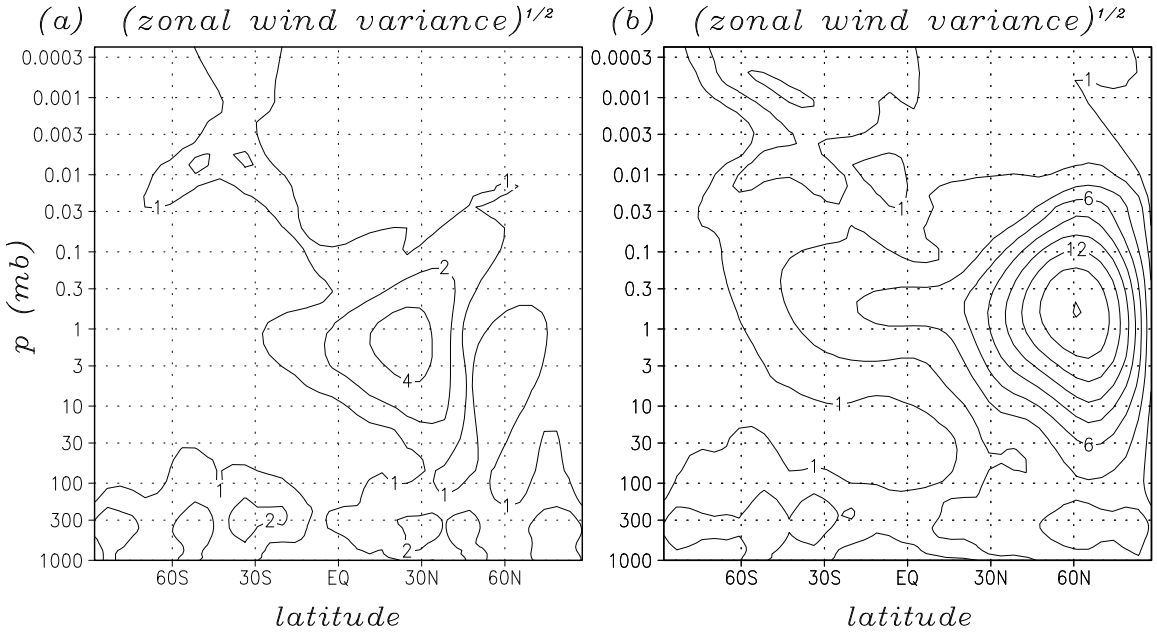

Figure 28: Standard deviation of the zonal-mean zonal wind (contours $1, 2, 4, 6, 8, \ldots$ ms^{-1}) in the aquaplanet experiment (a) and in the control run (b).

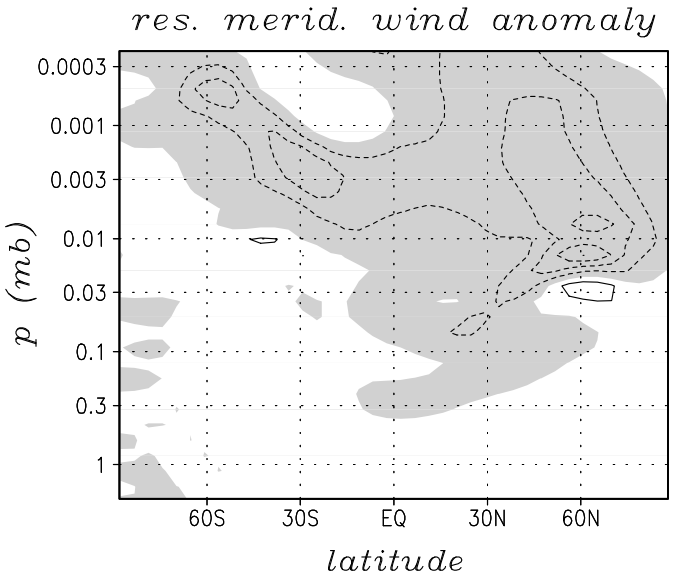

Figure 29: Difference of the residual meridional wind in the control run from the aquaplanet run (contour interval 2 ms^{-1}). The zero contour is not drawn, and negative values are shaded.

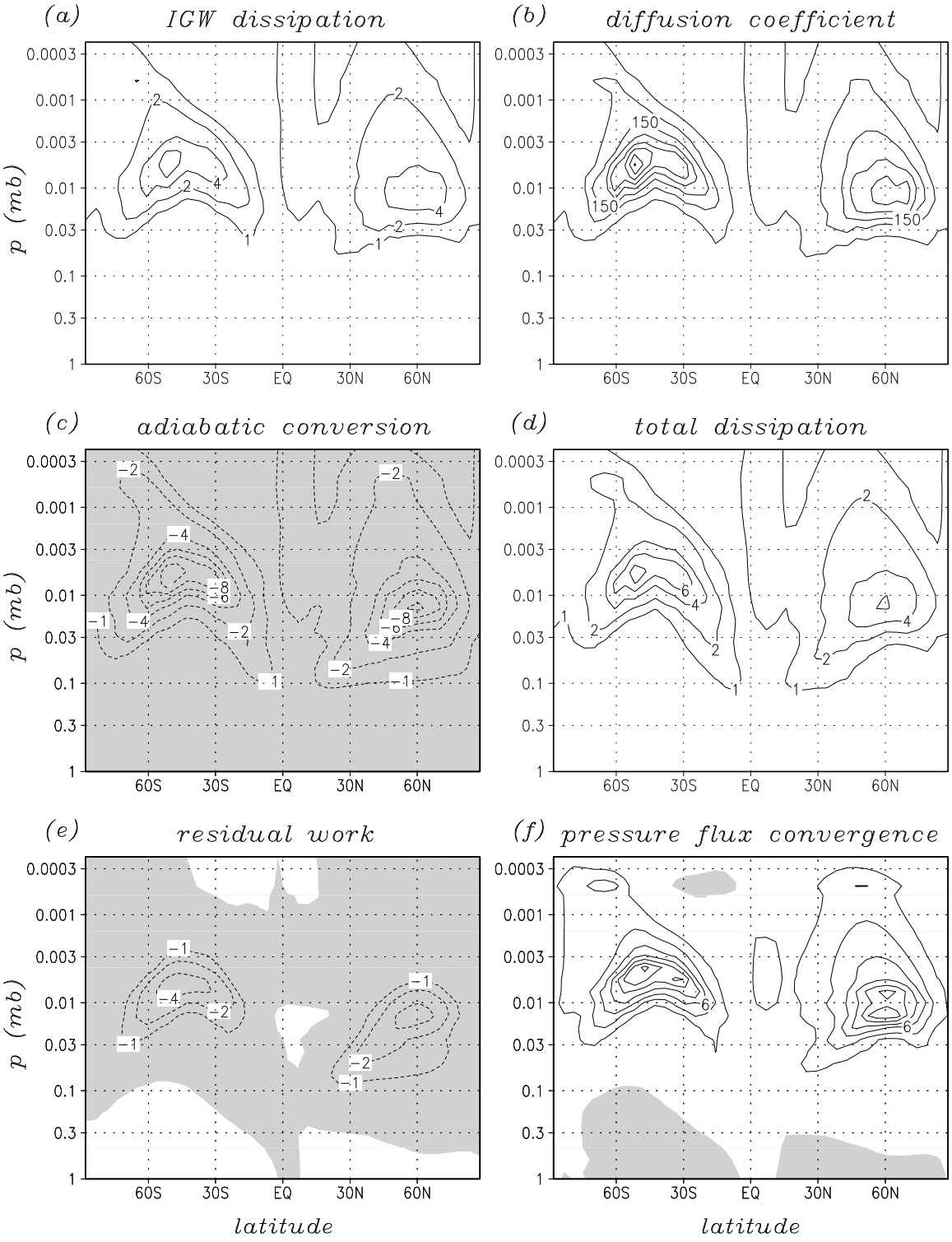

Figure 30: Same as Fig. 24, but for the model configuration with zonally symmetric orography and zonally symmetric heating functions (aquaplanet run). The model setup is otherwise identical to that of the control run.

trol run is representative for the austral summer mesosphere and that the corresponding aquaplanet result is representative for boreal summer. Therefore, since the aforementioned rocket-borne in-situ measurements of turbulent parameters correspond to boreal summer conditions, they should be compared to the summer MLT results obtained with the aquaplanet model configuration. Figure 30 shows corresponding contributions to the heat budget of the MLT analogously to Fig. 24. Figures 30a,b,d may be compared to Figs. 24a,b,d. It follows that stationary wave forcing in the winter troposphere weakly affects turbulent parameters in the summer MLT, resulting in somewhat stronger total dissipation rates up to $\sim 8\mathrm{Kd}^{-1}$ in the aquaplanet run. We therefore expect no significant north-south asymmetry for the measurement of turbulent parameters in summer. In contrast, the model predicts a very strong north-south asymmetry in the winter MLT. Stated otherwise, the control and aquaplanet simulations qualitatively reproduce the prominent winter-summer asymmetry in gravity wave effects and turbulent dissipation rates that are known for the northern MLT (Lübken, 1997a), while a much weaker winter-summer asymmetry is predicted for the southern MLT. Recall however that the gravity wave source is prescribed in the present simulations. Therefore, our sensitivity experiment can capture only those effects that are due to the modulation of gravity wave propagation and saturation. Competing effects that result from variations in the gravity wave source are excluded.

Figure 31 summarizes the above discussion by comparing Lübken's averaged observational estimates of the turbulent dissipation at Andøya (69^0N) against some selected vertical cuts of Figs. 24d and 30d. The resulting model estimate of the total dissipation for boreal summer is somewhat in excess of $\sim 8\ \mathrm{Kd}^{-1}$ around 52^0. This value is too weak by about a factor of 1.7 in comparison with the observation. Conversely, the model predicts stronger dissipation rates than observed for boreal winter, and the simulated dissipation is generally concentrated at lower altitudes. Note again that no attempt has been made to tune the gravity wave parameters, the equilibrium temperature, or the relaxation time in such a manner that the simulated dissipation is in better agreement with observations.

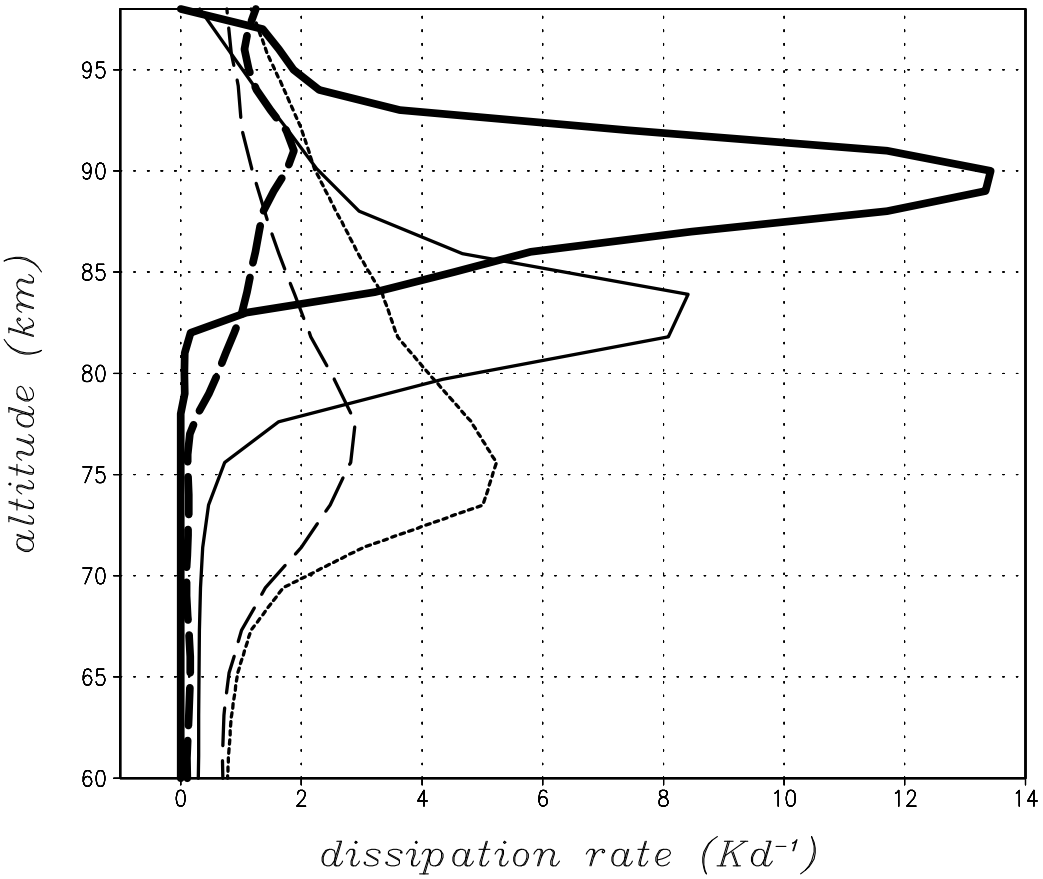

Figure 31: Comparison of averaged observed dissipation rates (thick curves, data taken from Tabs. 3,4 in the paper of Lükben (1997a)) against simulated mean dissipation rates (thin curves). The thick curves were obtained from several rocket flights at Andøya (69^0N) during the summer (solid) and winter (dashed) seasons. The thin solid curve is taken from the aquaplanet simulation at 52^0S (Fig. 30d) and corresponds to boreal summer conditions. The thin dashed curve is taken from the control run at 52^0N (Fig. 24d) and corresponds to boreal winter conditions. In addition, the thin dotted curve, taken from the aquaplanet run at 52^0N, indicates the model estimate for austral winter conditions.

Chapter 7

Summary and concluding remarks

This study has aimed to provide a hydrodynamically consistent view of the planetary-scale heat and energy budgets in presence of gravity wave breakdown. It has been stressed that this task requires the simultaneous representation of both internal gravity waves and small-scale turbulence. In order to set the basis for the treatment of nonconservative gravity wave propagation, we have given much room to revisit the energetics of turbulent motion and to formulate corresponding parameterization schemes for global or mesoscale circulation models in accordance with these basic concepts. Then, as a second step and as an analogy as well, the same concepts have been applied to assess the action of gravity wave perturbations on the planetary-scale flow.

In chapter 2 we have recapitulated the well-known formalism of averaging over turbulent motions. It has been shown that, according to the energy conservation law, the frictional heating owing to Reynolds stresses (rhs of Eq. (2.33)) cannot be omitted in the thermodynamic equation of motion. Rather, to a first approximation, the rate of change of turbulent kinetic energy may be neglected.

A comprehensive formulation of anisotropic turbulent momentum diffusion and the associated dissipation for application in GCMs has been given in chapters 3 and 4. It has been noted that conventional methods to account for horizontal momentum diffusion are not consistent with the Eulerian law of angular momentum conservation. Hence, the associated dissipation cannot even be defined. In order to solve this problem, we have analysed the anisotropic turbulent analogue of the molecular stress tensor. Then those terms proportional to the horizontal diffusion coefficient which give rise to stress at horizontally aligned Eulerian sectional planes have been eliminated. By this method we have arrived at a suitable symmetric stress tensor formulation for harmonic (Nabla square) horizontal momentum diffusion (Eqs. (3.5),(3.7),(3.9)). The analysis can be generalized to arbitrary orders, revealing that the dissipation is positive definite in the harmonic case only. Therefore, biharmonic and higher order horizontal momentum diffusion schemes

are not consistent with the second law of thermodynamics even if the stress tensor is symmetric. Grid-point models often involve filter algorithms instead of an explicit horizontal diffusion. The compatibilities of such filter algorithms with the constraints of a symmetric stress tensor, energy conservation, and thermodynamic irreversibility need to be investigated.

The numerical treatment of subscale vertical momentum fluxes has been addressed in chapter 4. New finite-difference forms for the frictional heating associated with vertical momentum diffusion and the residual work owing to gravity wave-mean flow interaction have been derived. These forms rest on the general constraint that, according to the no-slip condition, surface friction must not affect the energy budget of the atmosphere.

Utilizing a troposphere-stratosphere version of the *Kühlungsborn Mechanistic general Circulation Model (KMCM)* (see appendix A; model details are also given in Becker et al. (1997), Becker and Schmitz (2001), and Becker (2003)), the proposed stress tensor formulations of momentum diffusion and dissipation (control case) have been tested against the corresponding conventional methods. First, we have reinvestigated the dynamics of a baroclinic life cycle in a thermally and mechanically isolated model atmosphere (Simmons and Hoskins, 1978). Using the conventional horizontal diffusion scheme, significant losses of total angular momentum and total energy occur around the life cycle maximum. While the first shortcoming arises from the asymmetry of the stress tensor, the latter is due to the lack of frictional heating. The loss of total energy during the life cycle is of the same magnitude as the kinetic energy of the atmosphere. On the other hand, angular momentum and total energy are precisely conserved in the control case, as it should be.

Analogous shortcomings of the conventional model design have been found in perpetual January runs where the model setup has been completed by idealized parameterizations for radiative and condensational heating (section 5.2), as well as by a standard boundary layer diffusion scheme. In the control case, the boundary layer scheme has been completed by the dissipation owing to vertical momentum diffusion as proposed in chapter 4. For the conventional momentum diffusion and with the dissipation being ignored, spurious sources in the global budgets of angular momentum and energy are found (Figs. 12,13). These deficiencies are reduced by about two orders of magnitude in the control case. While the spurious torques appear to be less important in either case, the spurious net thermal forcing amounts to 2 Wm^{-2} for the conventional model setup. This value is obtained as well as the global average of the simulated dissipation in the control case. Hence we can conclude that, due to the lack of frictional heating, conventional comprehensive GCMs must have a systematic imbalance of about 2 Wm^{-2} between the incoming and outgoing radiation. The spatial distribution of the simulated frictional heating (Fig. 14) furthermore suggests that this bias is in the main due to the lack in boundary layer

dissipation.

These conclusions may have important implications for climate change simulations for the following reasons. The net radiative forcing associated with a doubling of the pre-industrial carbon dioxide concentration in the atmosphere is about 4 Wm^{-2} (IPCC, 1994). This value is of the same order of magnitude as the dissipation of the resolved flow. Furthermore, climate change simulations with higher greenhouse gas concentrations yield significant reductions in sea ice coverage and increased near-surface temperatures (e.g., Mitchell, 1991), hence also stronger boundary layer mixing. Since the tropospheric dissipation is strongest in the boundary layer, it may feed back on the increase of near-surface temperatures. It is thus obvious that hydrodynamically consistent parameterizations of turbulent friction and dissipation are necessary to confirm the reliability of climate change simulations.

The simulated angular momentum budget has shown that the horizontal diffusion coefficient should be zero in the lowermost troposphere. This is required to avoid coordinate transformation errors that result from applying the proposed stress tensor formulation of horizontal momentum diffusion directly in the hybrid coordinate system. A further side constraint is that the hybrid surfaces resemble pressure surfaces in the middle troposphere and farther above. Other terrain-following vertical coordinates, such as sigma or log pressure, follow the topographic elevations in every model layer. These coordinate systems should generally be avoided to allow for angular momentum conservation of the proposed horizontal diffusion scheme. The simple idea to neglect horizontal diffusion entirely in the lower troposphere contrasts with correction terms that are commonly used in order to apply conventional horizontal diffusion schemes in regions of steep orography (eg. Kiehl et al., 1996, p. 25). In addition, we have shown that retaining horizontal diffusion in the lower troposphere efficiently damps the overall wave activity. In particular, the polar night jet is enhanced by $\sim$10 ms^{-1}, and stratospheric polar night temperatures drop by $\sim$5 K.

The present harmonic horizontal diffusion scheme can be applied with two different traces of the stress tensor. If the trace is $2\,D$ (Eq. (3.5)), where D is the horizontal divergence, the damping of the divergent flow is two times stronger than in the alternative case with zero trace (Eq. (3.11)). In the latter case, larger spurious angular momentum and heat sources are obtained. These result presumably from larger aliasing errors associated with the divergent part of the flow. Therefore, the tensor (3.5) may be better suited for practical use in GCMs.

The representation of atmospheric turbulence by diffusion is generally complicated by the fact that subscale circulation or wave systems which are not resolved by the model must be parameterized as well. For the troposphere it is well known that mesoscale

convection for instance accounts for adiabatic conversion of available potential energy into kinetic energy. A similar mechanism is likely to exist in the upper mesosphere due to the breakdown of internal gravity waves (IGWs). Rocket-borne in-situ measurements of turbulence in the region of the cold summer mesopause (Lübken 1997a,b) have revealed averaged frictional heating rates of about 10-20 Kd^{-1}. Assuming that such heating rates are representative, traditional views of the planetary-scale heat budget of the MLT (e.g., Chandra, 1980; Lübken et al., 1993) cannot consistently explain the observations. In the present study, a thermodynamic equation of motion for the general circulation has been derived by consequently filtering out small-scale turbulent motions and IGWs. A key assumption has been that the scales of the resolved planetary-scale flow, of the gravity waves, and of the small-scale turbulent motions are separated. We have shown that the adiabatic conversion of mean enthalpy into IGW kinetic energy, the dissipation of IGW kinetic energy, and the wave entropy flux must not be neglected. The residuum of adiabatic generation and dissipation of IGW kinetic energy, defined as the residual work W_{res}, can be eliminated via the proposed approximate kinetic energy equation for IGWs (Eq. (2.58)). By strictly evaluating Lindzen's saturation assumption we have furthermore shown that the wave entropy flux formally corresponds to a diffusion of the background state with half of the wave-induced turbulent diffusion coefficient. Thus, we have derived an upper bound of 2 for the effective Prandtl number which scales the entropy flux owing to the gravity waves themselves and the wave-induced turbulent diffusion of the mean flow.

These theoretical results have been applied in *KMCM* using a T29/L60 version extending up to about 100 km and including a Lindzen-type gravity wave parameterization completed by the appropriate thermodynamic effects as discussed above. As a particular benefit of using Lindzen's saturation theory for individual gravity waves, the frictional heating generated by the gravity waves can be calculated analytically. The resulting model estimate of the total dissipation (Figs. 24d, 30d, 31) amounts to $\sim 8\ \mathrm{Kd}^{-1}$ around 52^0 in the summer MLT. This value is too weak by about a factor of 1.7 and located at a lower altitude in comparison with the observational result of Lübken et al. (1997a) obtained for 69^0. Furthermore, the simulated winter mesospheric dissipation rates are generally somewhat too strong. Even so, the orders of magnitude and seasonal dependencies of both computational and observational estimates are well consistent, given the various uncertainties of either method.

The present model simulations reveal that the dissipation of gravity wave kinetic energy is overcompensated by adiabatic conversion of mean enthalpy into gravity wave kinetic energy. Thus the net effect of both subscale heating rates (the residual work W_{res}) is to cool the MLT (Fig. 24e). The total thermal effect owing to the direct heating

rates associated with gravity wave breakdown is heating around the breaking levels and cooling farther above (Fig. 25a). This pattern is very similar to the wave enthalpy flux convergence or the effective vertical diffusion term.

These parameterized gravity wave effects remain to be confirmed by direct numerical simulation of gravity breakdown in the MLT. Such models are supposed to simulate the adiabatic conversion term and the wave entropy flux explicitly. Hence, also the turbulent frictional heating must explicitly be accounted for, since otherwise a highly relevant term would be missing in the heat and energy budgets. We note, however, that state-of-the-art direct numerical simulations of gravity wave breaking neglect the frictional heating term (e.g., Andreasen et al., 1994; Werne and Fritts, 1999; Fritts and Werne, 2000).

The present gravity wave parameters have been chosen such that the simulated circulation of the mesosphere is consistent with other authors (e.g., Holton, 1983; Garcia and Solomon, 1985; Volodin and Schmitz, 2001). Then, also the maximum dissipation in the summer MLT is found to be of the order of 5-10 Kd^{-1}. Therefore, the acquired qualitative consistence of the observed and simulated dissipation rates is not incidental. Rather, it appears to be an unique strength of Lindzen's saturation theory that reasonable mean dissipation rates are predicted in a hydrodynamically consistent way, once the tropospheric gravity wave source is adjusted to drive a reasonable summer-to-winter-pole residual circulation in the MLT.

This conclusion is also supported by an additional model run where the effective Prandtl number has been raised from 1 to 2. As a result, the reduced cooling by vertical diffusion of entropy leads to higher temperatures, particularly in the summer MLT where the signal exceeds 30 K (Fig. 26). In addition, also the IGW-driven residual circulation is reduced, indicating a weaker efficiency of IGW breakdown. Consistent with this model response, also the maximum dissipation in the summer MLT is reduced.

Even though only perpetual January model simulations have been analysed, the present simple GCM allows to estimate possible north-south asymmetries in the middle atmosphere. The procedure simply is to compare the control simulation, where orographic and thermal forcing of planetary waves is applied, against the corresponding aquaplanet simulation. With regard to the topic of the present study it has been shown that north-south asymmetries in the summer MLT can affect turbulent parameters like the dissipation or the turbulent diffusion coefficient, though the effects are rather weak. The situation is different in the winter MLT where the model indicates a pronounced north-south asymmetry. In particular, in the boreal winter MLT, turbulent parameters are much weaker than in the austral winter MLT (Fig. 31). Of course, these findings rely on the usual assumption of a horizontally uniform and time-independent gravity wave source.

Finally, the chief limitations of the present simple GCM should be recalled. First, we have utilized crude representations of radiative and latent heating, namely temperature relaxation, prescribed tropical heat sources, and self-induced condensational heating in the middle latitudes. Second, the present gravity wave parameterization has various shortcomings. For instance, the wave breaking process is entirely based on linear theory. No nonlinear interactions between the individual gravity waves have been considered like in the study of Holton and Zu (1984) for instance. It is furthermore questionable to assume that turbulent diffusion is independent of the phase of the breaking gravity wave (Hodges, 1967; Chao and Schoeberl, 1984). As noted by Weinstock (1988), supersaturation may have important effects as well but has been neglected here. Another oversimplification may be due to using a family of individual gravity waves rather than a broad spectrum like in the theory of Hines (1997) for instance. Of course, like in any GCM with gravity wave parameterization, we have invoked the single column approximation, as well as the assumption of an instantaneous response of the wave field to changes of the mean flow. Despite these idealizations it is believed that Lindzen (1981) presented the simplest physical model that captures the essential dynamics of gravity wave saturation. In this study we have tried to stay as close as possible to this concept in order to assess the direct thermodynamic effects in the framework of a global circulation model. The proposed definitions of energy deposition, entropy flux, and turbulent dissipation may also be useful in combination with other gravity wave parameterization schemes.

Acknowledgements:

I am indebted to Prof. Gerhard Schmitz who greatly stimulated and supported this study in the course of our long-year collaboration.

Helpful discussions with Dr. Markus Rapp and Prof. Franz-Josef Lübken were important for the mesospheric part of this study. For inspiring comments I would like to thank Prof. Richard S. Lindzen and Prof. Joseph Egger. I am grateful to the following former or present colleagues at the *Leibniz-Institut für Atmosphärenphysik* (IAP) for friendship and numerous fruitful discussions: Dr. Ulrich Achatz, Dr. Jörn Bartels, Dr. Axel Gabriel, Dr. Rolf Geprägs, and Dipl.-Phys. Heiner Körnich. Many thanks also to Dr. Vladimir A. Alekseev, Dr. Uwe Berger, Dr. Norbert Grieger, Dr. Peter Hoffmann, Dr. Evgeny M. Volodin, and Dr. Christoph Zülicke. I gratefully acknowledge the support by the technical and administration staff of the IAP.

Last not least I am indebted to my family for understanding and for being a counterbalance to my work.

Appendix A

Description of KMCM

A.1 Governing equations

The present simplified GCM is the *Kühlungsborn Mechanistic general Circulation Model* (*KMCM*) coded by the author. It is based on the primitive equations defined in section 2.4. These governing equations are transformed using a terrain-following vertical hybrid coordinate η as follows. Pressure p is represented as a function of η and surface pressure p_s:

$$p(\eta; p_s) = a(\eta) + b(\eta)\, p_s\,. \tag{A1}$$

The coefficients a and b must guarantee monotonic growth of p with η, as well as

$$p(\eta = 0; p_s) = 0 \quad \text{and} \quad p(\eta = 1; p_s) = p_s\,. \tag{A2}$$

The flexibility of (A1) is used to let surfaces of constant η correspond to σ-levels near the ground and to pressure levels at high altitudes. To achieve such a behavior we define

$$a(\eta)/p_{00} := \eta(1-\eta) \quad \text{and} \quad b(\eta) := \eta^2\,. \tag{A3}$$

Here, $p_{00} := 1013$ mb corresponds to the mass of the atmosphere in case of zero orography. With the specific definitions introduced in section 2.4, chapters 3 and 4, and sections 5.2 and 6.2, the prognostic equations for horizontal vorticity ξ, horizontal divergence D, temperature T, and surface pressure p_s may be written as

$$\partial_t \xi = (\nabla \times \mathbf{f}) \cdot \mathbf{e}_z \tag{A4}$$

$$\partial_t D = \nabla \cdot \mathbf{f} - \nabla^2\left(\frac{\mathbf{v}^2}{2} + \Phi\right) \tag{A5}$$

$$\mathbf{f} := \mathbf{v} \times (\, f + \xi\,)\, \mathbf{e}_z - \dot{\eta}\, \partial_\eta \mathbf{v} - \frac{RT}{p}\, \nabla\, p + \mathbf{H} + \mathbf{Z} - \frac{g}{\partial_\eta\, p}\, \partial_\eta\, \mathbf{F} \tag{A6}$$

$$\partial_t T = -(\, \mathbf{v} \cdot \nabla + \dot{\eta}\, \partial_\eta\,)\, T + \frac{RT}{c_p\, p}\, \omega + Q + \frac{E}{c_p} + \mu_h + \mu_z + \frac{\epsilon_h + \epsilon_z}{c_p} \tag{A7}$$

$$\partial_t p_s \quad = \quad -\int_0^1 \nabla \cdot (\partial_\eta \, p \, \mathbf{v}) \, d\eta \, . \tag{A8}$$

The prognostic equations (A4)-(A8) are completed by (A1) and (A3), and expressions for geopotential Φ, vertical velocity $\dot{\eta}$, and pressure velocity ω:

$$\Phi \quad = \quad \Phi_s + \int_\eta^1 \frac{R\,T}{p} \frac{\partial p}{\partial \tilde{\eta}} \, d\tilde{\eta} \tag{A9}$$

$$\dot{\eta} \quad = \quad -\frac{1}{\partial_\eta \, p} \left(b \, \partial_t \, p_s + \int_0^\eta \nabla \cdot (\partial_{\tilde{\eta}} p \, \mathbf{v}) \, d\tilde{\eta} \right) \tag{A10}$$

$$\omega \quad = \quad b \, (\mathbf{v} \cdot \nabla) \, p_s - \int_0^\eta \nabla \cdot (\partial_{\tilde{\eta}} \, p \, \mathbf{v}) \, d\tilde{\eta} \, . \tag{A11}$$

Equation (A9) follows from vertical integration of the hydrostatic approximation

$$\partial_\eta \, \Phi = -\frac{R\,T}{p} \, \partial_\eta \, p \tag{A12}$$

with Φ_s denoting the orography (Fig. 7a). Vertical velocity, pressure velocity, and surface pressure tendency follow from integrations of the continuity equation

$$\partial_t \, (\partial_\eta \, p \,) + \nabla \cdot \, (\partial_\eta \, p \, \mathbf{v} \,) + \partial_\eta \, (\partial_\eta \, \dot{\eta} \,) = 0 \tag{A13}$$

with respect to the kinematic boundary conditions

$$\dot{\eta} = 0 \quad \text{for} \quad \eta = 0 \quad \text{and} \quad \eta = 1 \, . \tag{A14}$$

A.2 Vertical discretization

The model equations are prepared for numerical computation using an energy and angular momentum conserving finite-difference scheme introduced by Simmons and Burridge (1981) and modified by a reference state reformulation (Simmons and Chen, 1991).

First of all, the intermediate hybrid levels

$$0 = \eta_{1/2} < \eta_{3/2} < \, \ldots \, < \eta_{lev-1/2} < \eta_{lev+1/2} = 1$$

must be fixed. The corresponding intermediate pressure levels

$$0 = p_{1/2} < p_{3/2} < \, \ldots \, < p_{lev-1/2} < p_{lev+1/2} = p_s$$

are known from (A1). Full pressure levels and centered pressure differences are defined as

$$p_l := (p_{l-1/2} + p_{l+1/2})/2 \quad \text{and} \quad \Delta p_l := p_{l+1/2} - p_{l-1/2} \quad \text{for} \quad l = 1 \ldots lev \, . \tag{A15}$$

In *KMCM*, lev is arbitrary, and the distribution of levels can be adjusted by a few parameters.

The discretization method yields partial differential equations for the hybrid level representations of the prognostic variables $\xi_l(\lambda,\phi,t)$, $D_l(\lambda,\phi,t)$, $T_l(\lambda,\phi,t)$, and $p_s(\lambda,\phi,t)$, where $l = 1, 2, \ldots, lev$. The corresponding tendencies are computed by evaluating the right hand sides of (A4)-(A8) at full model levels. The hybrid level representations of diffusion, dissipation, and gravity wave tendencies are given in chapters 3,4 and in section 6.2. Evaluation of the bulk heating (5.6) at full hybrid levels is also straightforward.

A finite-difference representation of the dynamical core in an angular-momentum and energy conserving way is as follows (Simmons and Burridge, 1981):

$$\left(\frac{RT}{p}\nabla p\right)_1 = \frac{RT_1}{\Delta p_1}\nabla\,\Delta p_1 \tag{A16}$$

$$\left(\frac{RT}{p}\nabla p\right)_l = \frac{RT_l}{\Delta p_l}\left(\ln\frac{p_{l+1/2}}{p_{l-1/2}}\nabla\,p_{l-1/2} + \alpha_l\nabla\,\Delta p_l\right), \quad l = 2\ldots lev \tag{A17}$$

$$\Phi_1 = \Phi_s + \ln 2\; RT_1 + R\sum_{n=2}^{lev} T_n \ln\frac{p_{n+1/2}}{p_{n-1/2}} \tag{A18}$$

$$\Phi_l = \Phi_s + \alpha_l\, RT_l + R\sum_{n=l+1}^{lev} T_n \ln\frac{p_{n+1/2}}{p_{n-1/2}}, \quad l = 2\ldots lev \tag{A19}$$

$$\alpha_l = 1 - \frac{p_{l-1/2}}{\Delta p_l}\ln\frac{p_{l+1/2}}{p_{l-1/2}}, \quad l = 2\ldots lev \tag{A20}$$

$$\left(\frac{RT}{c_p\,p}\omega\right)_1 = -\frac{RT_1}{c_p\,\Delta p_1}\ln 2\left\{\Delta p_1\, D_1 + \mathbf{v}_1\cdot\nabla\,\Delta p_1\right\} + \frac{1}{c_p}\mathbf{v}_1\cdot\left(\frac{RT}{p}\nabla p\right)_1 \tag{A21}$$

$$\begin{aligned}\left(\frac{RT}{c_p\,p}\omega\right)_l = &-\frac{RT_l}{c_p\,\Delta p_l}\left(\ln\frac{p_{l+1/2}}{p_{l-1/2}}\sum_{n=1}^{l-1}\left\{\Delta p_n\, D_n + \mathbf{v}_l\cdot\nabla\,\Delta p_n\right\}\right.\\ &\left.+\alpha_l\left\{\Delta p_l\, D_l + \mathbf{v}_l\cdot\nabla\,\Delta p_l\right\}\right)\\ &+\frac{1}{c_p}\mathbf{v}_l\cdot\left(\frac{RT}{p}\nabla p\right)_l, \quad l = 2\ldots lev\end{aligned} \tag{A22}$$

$$\begin{aligned}\left(\dot\eta\,\partial_\eta\,\{u,v,T\}\right)_l = \frac{1}{2\,\Delta p_l}&\left((\dot\eta\partial_\eta p)_{l+1/2}\left(\{u,v,T\}_{l+1} - \{u,v,T\}_l\right)\right.\\ &\left.+(\dot\eta\partial_\eta p)_{l-1/2}\left(\{u,v,T\}_l - \{u,v,T\}_{l-1}\right)\right),\ l = 1\ldots lev\end{aligned} \tag{A23}$$

$$(\dot\eta\,\partial_\eta p)_{1/2} = (\dot\eta\,\partial_\eta p)_{lev+1/2} = 0 \tag{A24}$$

$$(\dot\eta\,\partial_\eta p)_{l+1/2} = -b_{l+1/2}\,\partial_t p_s - \sum_{n=1}^{l}\left\{\Delta p_n\, D_n + \mathbf{v}_n\cdot\nabla\,\Delta p_n\right\},\ l = 1\ldots lev-1$$

$$\partial_t p_s \;=\; -\sum_{n=1}^{lev}\Big\{\,\Delta p_n\, D_n + \mathbf{v}_n\cdot\nabla\,\Delta p_n\,\Big\}\,. \tag{A25}$$

This scheme has a specific problem. Let us assume a reference atmosphere at rest with $T = T_{ref}(p)$ and horizontally varying surface pressure $p_s = p_{sg}$ due to orography Φ_s. In this trivial example all tendencies must vanish. And this is, of course, the case for the continuous equations. However, in finite-difference form, the pressure gradient term and the geopotential gradient give rise to physically inconsistent tendencies, known as the *geostrophic wind error*. This error is defined as

$$f\,(\,v_l\,\mathbf{e}_x - u_l\,\mathbf{e}_y\,) = (\,\frac{RT}{p}\,\nabla\,p\,)_l + \nabla\,\Phi_l \tag{A26}$$

$$\text{in the case of}\quad T = T_{ref}(p)\quad\text{and}\quad \nabla\Phi_s = -\frac{R\,T_{ref}(p_{sg})}{p_{sg}}\,\nabla\,p_{sg}\,.$$

Owing to (A16)-(A20) the residuum (A26) is generally different from zero and produces significant errors above the tropopause, as already mentioned by Simmons and Burridge (1981). This problem can be avoided by expanding (A16)-(A19) with respect to a reference state. One way to perform such a modification has been proposed by Simmons and Chen (1991) and is incorporated for instance in the climate model *ECHAM* (DKRZ, 1992). A similar method is applied in *KMCM*. Differences to previous methods arise from the choice of the reference temperature and from using p_s instead of $\ln p_s$ as a prognostic variable.

Let us define

$$\tilde{T} := T - T_{ref}(p) \tag{A27}$$

and rewrite the continuous formulations of the pressure gradient term and the gradient of the geopotential

$$\frac{RT}{p}\,\nabla\,p + \nabla\,\Phi \;=\; \frac{R\tilde{T}}{p}\nabla\,p + \nabla\left(\,\tilde{\Phi}_s + \int_{\eta}^{1}\frac{R\tilde{T}}{p}\,\partial_{\eta'}\,p\,d\eta'\right) \tag{A28}$$

$$\tilde{\Phi}_s \;:=\; \Phi_s + \int_{p_{00}}^{p_s}\frac{R\,T_{ref}(p)}{p}\;dp\,. \tag{A29}$$

The mass of the atmosphere is defined by the mean surface pressure p_{ref} which, in the present model, is constant by definition. For zero orography we have $p_{ref} \equiv p_{00} = 1013$ mb. When orography is included, we can implicitly define a reference surface pressure distribution $p_{sg}(\lambda,\phi)$ corresponding to $T = T_{ref}(p)$ by the root of the rhs of (A29):

$$0 \;=\; \Phi_s(\lambda,\phi) + \int_{p_{00}}^{p_{sg}(\lambda,\phi)}\frac{R\,T_{ref}(p)}{p}dp\,. \tag{A30}$$

In *KMCM*, Eq. (A30) is solved for p_{sg}, and p_{ref} is defined as the horizontal average of p_{sg}.

Obviously, both (A28) and (A29) vanish for the reference state. This suggests to use the rhs of (A28) as a basis for finite differencing since the geostrophic wind error is zero by definition. Accordingly, (A16)-(A19) are reformulated in the following way:

$$\left(\frac{RT}{p}\nabla p\right)_1 = \frac{R\tilde{T}_1}{\Delta p_1}\nabla\,\Delta p_1 \tag{A31}$$

$$\left(\frac{RT}{p}\nabla p\right)_l = \frac{R\tilde{T}_l}{\Delta p_l}\left(\ln\frac{p_{l+1/2}}{p_{l-1/2}}\nabla\,p_{l-1/2} + \alpha_l\nabla\,\Delta p_l\right), \quad l = 2\ldots lev \tag{A32}$$

$$\Phi_1 = \tilde{\Phi}_s + \ln 2\; R\tilde{T}_1 + R\sum_{n=2}^{lev}\tilde{T}_n\ln\frac{p_{n+1/2}}{p_{n-1/2}} \tag{A33}$$

$$\Phi_l = \tilde{\Phi}_s + \alpha_l\, R\tilde{T}_l + R\sum_{n=l+1}^{lev}\tilde{T}_n\ln\frac{p_{n+1/2}}{p_{n-1/2}}\,, \quad l = 2\ldots lev\,. \tag{A34}$$

The reference temperature $T_{ref}(p)$ used in *KMCM* is defined as

$$\begin{aligned} T_{ref}(p;p_{bo},p_{tr},p_{to},T_{bo},T_{tr},T_{to}) &:= T_{bo}\,\zeta(p;\ldots) \\ \zeta(p;\ldots) &:= \zeta_0 + \frac{\zeta_1}{\varpi+p} + \frac{\zeta_2}{(\varpi+p)^2}\,. \end{aligned} \tag{A35}$$

This profile can be adjusted with respect to 6 parameters, fixing T_{ref} at the pressure levels p_{bo}, p_{tr}, and p_{to}. These levels are assumed to correspond to bottom, tropopause, and some middle atmospheric pressure level. Then, ζ must satisfy

$$\begin{aligned} \zeta(p_{bo};\ldots) &= 1 \\ \zeta(p_{tr};\ldots) &= T_{tr}/T_{bo} \\ \partial_p\zeta(p_{tr};\ldots) &= 0 \\ \zeta(p_{to};\ldots) &= T_{to}/T_{bo}\,. \end{aligned} \tag{A36}$$

The conditions (A36) allow to eliminate the coefficients ζ_0, ζ_1, ζ_2, and ϖ. The procedure is described in Becker et al. (1997, appendix) for the vertical profile of the equilibrium temperature. The default parameter setup for T_{ref} is $p_{bo} = 1013$ mb, $p_{tr} = 110$ mb, $p_{to} = 0.1$ mb, $T_{bo} = 280$ K, $T_{tr} = 210$ K and $T_{to} = 220K$. The corresponding temperature profile is shown in Fig. 32a. It may be compared to the reference profile used in *ECHAM* (DKRZ, 1992, Eq. (2.4.2.14)). Throughout the troposphere both reference states are quite similar. Above the tropopause, (A35) yields reasonable temperatures. The *ECHAM* profile (Fig. 32b) has no tropopause and tends to zero for $p \to 0$. Hence, the geostrophic error above the tropopause can hardly be eliminated. Therefore *KMCM* utilizes the more realistic profile.

Owing to (A35), Eq. (A29) becomes

$$\tilde{\Phi}_s = \Phi_s + RT_{bo}\left(\zeta_0 \ln\frac{p_s}{p_{00}} + \left(\frac{\zeta_1}{\varpi} + \frac{\zeta_2}{\varpi^2}\right)\ln\frac{p_s\,(\,\varpi + p_{00}\,)}{p_{00}\,(\,\varpi + p_s\,)} + \frac{\zeta_2}{\varpi}\left(\frac{1}{\varpi + p_s} - \frac{1}{\varpi + p_{00}}\right)\right), \tag{A37}$$

and the reference surface pressure $p_{sg}(\lambda, \phi)$ is found by numerically determining the root of the rhs of (A37).

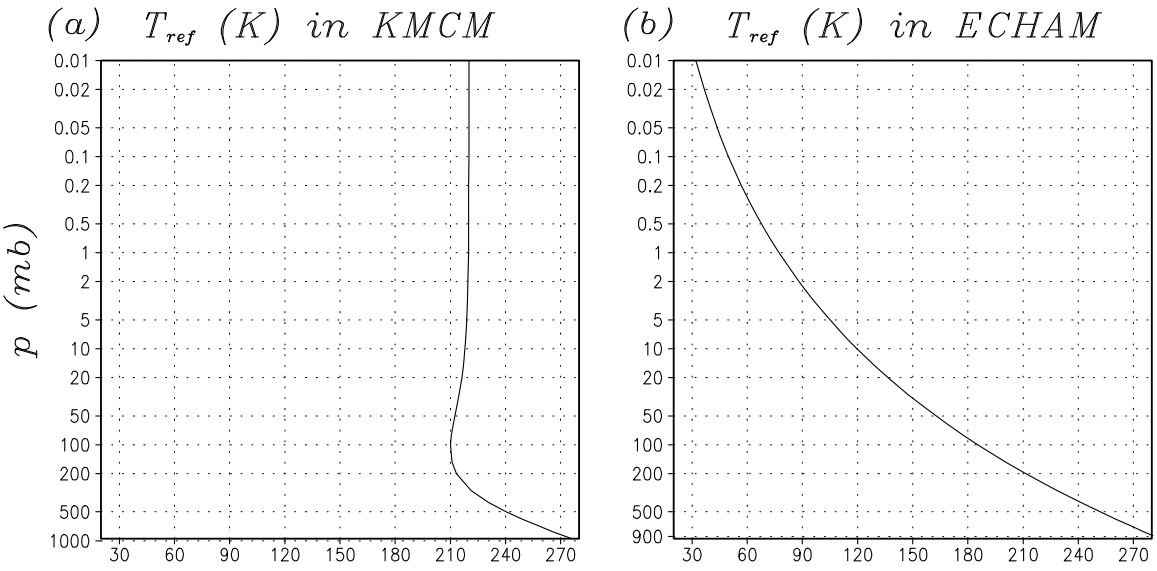

Figure 32: (a) Default reference temperature profile of *KMCM*. (b) Reference temperature used in *ECHAM*. The latter is calculated according to $T_c := T_{00}\,(p/p_{00})^{\beta}$ with $T_{00} = 288$ K and $\beta = 1/5.256$.

In section 5.2, *KMCM* is used with a T42/L24 resolution. For $p_s = p_{00}$, pressure levels in mb are from ground to top: 987, 903, 789, 684, 589, 503, 426, 357, 296, 242, 196, 155, 121, 92.3, 68.5, 49.3, 33.9, 22.1, 13.5, 7.43, 3.71, 1.86, 0.93, 0.31. In this model version, gravity wave effects are switched off. For the model runs presented in chapter 6, the vertical resolution consists of 60 hybrid layers. The corresponding pressure levels in mb are: 987, 915, 825, 743, 667, 598, 535, 478, 426, 379, 336, 297, 262, 231, 203, 177, 155, 135, 117, 93.7, 68.4, 49.9, 36.5, 26.6, 19.4, 14.2, 10.4, 7.56, 5.52, 4.03, 2.94, 2.15, 1.57, 1.14, 0.835, 0.609, 0.445, 0.325, 0 .237, 0.173, 0.126, 0.0922, 0.0673, 0.0491, 0.0359, 0.0262, 0.0191, 0.0140, 0.0102, 0.00744, 0.00543, 0.00396, 0.00289, 0.00211, 0.00154, 0.00113, 0.00082, 0.00060, 0.00047, 0.00022.

A.3 Boundary layer mixing

The parameterization of boundary layer mixing coefficients follows the local vertical diffusion scheme of Holtslag and Boville (1993). In *KMCM*, a slight modification has been introduced to the Richardson criteria in order to ensure that their derivatives are continuous. For $l = 1, \ldots, lev-1$, the diffusion coefficient is defined on half model layers as

$$k_{z\,l+\frac{1}{2}} = \left(\frac{1}{k_a\, z_{l+\frac{1}{2}}} + \frac{1}{30\ \mathrm{m}} \right)^{-2} |(\,\partial_z \mathbf{v}\,)_{l+\frac{1}{2}}|\ F(Ri_{l+\frac{1}{2}}) \tag{A38}$$

$$Ri_{l+\frac{1}{2}} = \frac{2\,g\,(\,\partial_z\,\Theta\,)_{l+\frac{1}{2}}}{(\,\Theta_l + \Theta_{l+1}\,)\,(\,\partial_z\,\mathbf{v}_{l+\frac{1}{2}}\,)^2} \tag{A39}$$

$$F(Ri) = \begin{cases} \sqrt{1-18\,Ri} & Ri < 0 \\ (1+9Ri+50Ri^2)^{-1} & Ri \geq 0\,. \end{cases} \tag{A40}$$

The diffusion tendencies are defined in section 4.1, and $k_a = 0.4$ is the van Kárman constant. The surface coefficient yields

$$C = c_N\ F_0(Ri_0)\ |\,\mathbf{v}_{lev}\,|\,, \quad c_N := \left(\frac{k_a}{\ln\left((z_{lev}+z_r)/z_r\right)} \right)^2 \tag{A41}$$

$$Ri_0 = \frac{g\,z_{lev}\,(\,\Theta_{lev}-\Theta_s\,)}{\Theta_{lev}\,\mathbf{v}_{lev}^2} \tag{A42}$$

$$F_0(Ri_0) = \begin{cases} 1 - 9\,Ri_0\,/(\,1\,+\,75\,c_N\,\sqrt{|Ri_0|(z_{lev}+z_r)/z_r}\,) & Ri_0 < 0 \\ (1+9Ri_0+50{Ri_0}^2)^{-1} & Ri_0 \geq 0\,. \end{cases} \tag{A43}$$

Here, z_r is the roughness length which has a constant value of 10^{-3} m in the present model experiments.

A.4 Spectral representation

In *KMCM* the spherical harmonics are defined as

$$Y_{n\,m}(\lambda,\phi) := \begin{cases} \sqrt{\frac{1}{\pi}}P_{n\,0}(\sin\phi) & \text{for } m = 0 \\ \sqrt{\frac{2}{\pi}}P_{n\,m}(\sin\phi)\,\cos m\lambda & \text{for } m > 0 \\ \sqrt{\frac{2}{\pi}}P_{n\,|m|}(\sin\phi)\,\sin|m|\lambda & \text{for } m < 0 \end{cases} \tag{A44}$$

$$\text{with} \qquad P_{n\,m}(x) := \sqrt{\frac{(2n+1)(n-m)!}{(n+m)!}}\,\frac{1}{n!\,2^{n+1}}\,(1-x^2)^{\,m/2}\,\frac{d^{\,(n+m)}}{d\,x^{n+m}}\,(x^2-1)^n\,. \tag{A45}$$

The total number of spherical harmonics in the case of triangular truncation at total wave number N is $(N+1)^2$. The normalization is such that

$$\int d\sigma\ Y_{n\,m}\,Y_{n'\,m'} = \int_0^{2\pi} d\lambda \int_{-1}^{1} d\sin\phi\ Y_{m\,m}\,Y_{n'\,m'} = \delta_{n\,n'}\,\delta_{m\,m'}\,. \tag{A46}$$

Vorticity, divergence, temperature, and surface pressure are expanded in series of spherical harmonics as

$$\xi_l(\lambda,\phi,t) = \sum_{m\,n} \xi_{l\,n\,m}(t)\, Y_{n\,m}(\lambda,\phi) \tag{A47}$$

$$D_l(\lambda,\phi,t) = \sum_{m\,n} D_{l\,n\,m}(t)\, Y_{n\,m}(\lambda,\phi) \tag{A48}$$

$$T(\lambda,\phi,t) = \sum_{m\,n} T_{n\,m}(t)\, Y_{n\,m}(\lambda,\phi) \tag{A49}$$

$$p_s(\lambda,\phi,t) = p_{ref} + \sum_{m\,n} p_{s\,n\,m}(t)\, Y_{n\,m}(\lambda,\phi)\,. \tag{A50}$$

The amplitudes $\xi_{l\,0\,0}$, $D_{l\,0\,0}$, and $p_{s\,0\,0}$ are zero by definition. Eq. (A50) differs from other spectral models where $\ln p_s$ instead of p_s is used as a prognostic variable (e.g., DKRZ, 1992) and hence the mass of the model atmosphere is treated as a prognostic variable.

Horizontal velocities are represented by

$$u_l = -\sum_{m\,n} \frac{a_e^2}{n(n+1)} \Big\{ D_{l\,n\,m}\, \partial_x\, Y_{n\,m} - \xi_{l\,n\,m}\, \partial_y\, Y_{n\,m} \Big\} \tag{A51}$$

$$v_l = -\sum_{m\,n} \frac{a_e^2}{n(n+1)} \Big\{ D_{l\,n\,m}\, \partial_y\, Y_{n\,m} + \xi_{l\,n\,m}\, \partial_x\, Y_{n\,m} \Big\} \tag{A52}$$

with ∂_x and ∂_y defined in Eq. (2.4). All horizontal derivatives are computed by using the analytical derivations of the spectral representations (A49)-(A52).

A set of ordinary differential equations for the spectral amplitudes is obtained by application of Galerkin's method at each full model layer. In order to simplify the resulting integrals we take advantage of the identities

$$\int d\sigma\; Y\, \frac{\partial_\lambda X}{a\cos\phi} = -\int d\sigma\; X\, \frac{\partial_\lambda Y}{a\cos\phi} \tag{A53}$$

$$\int d\sigma\; Y\, \frac{\partial_\phi(\cos\phi\, X)}{a\cos\phi} = -\int d\sigma\; X\, \frac{\partial_\phi\, Y}{a} \tag{A54}$$

$$\int d\sigma\; Y\, \nabla^2 X = \int d\sigma\; X\, \nabla^2 Y\,, \tag{A55}$$

which are valid for arbitrary spherical functions X and Y. Our final model equations can be written as:

$$\dot\xi_{l\,n\,m} = \int d\sigma \left(\mathbf{f}_l \times \nabla Y_{n\,m} \right) \cdot \mathbf{e}_z\,,\; l = 1 \ldots lev \tag{A56}$$

$$\dot D_{l\,n\,m} = -\int d\sigma \left(\mathbf{f}_l \cdot \nabla Y_{n\,m} + \left(\frac{\mathbf{v}^2}{2} + \Phi_l \right) \nabla^2 Y_{n\,m} \right),\; l = 1 \ldots lev \tag{A57}$$

$$\dot T_{l\,n\,m} = \int d\sigma \Big(-\vec v_l \cdot \nabla T_l - (\dot\eta \partial_\eta T)_l + \left(\frac{R\,T}{c_p p}\omega\right)_l + Q_l + \frac{E_l}{c_p} + \mu_{z\,l} + u_{h\,l} + \frac{\epsilon_{z\,l} + \epsilon_{h\,l}}{c_p} \Big)\, Y_{n\,m}\,,\; l = 1 \ldots lev \tag{A58}$$

$$\dot p_{s\,n\,m} = \int d\sigma\; \partial_t p_s\, Y_{n\,m}\,. \tag{A59}$$

The integrals on the rhs of (A56)-(A59) are computed by standard methods, i.e. by Gaussian quadrature with respect to $\sin\phi$ and discrete Fourier transform in longitudinal direction. Traditionally, the distribution of grid points is adapted such that the integrals are exact if the integrants are polynomials of third order in Y_{nm}. This assumption is equivalent to the condition that the tendency equations are of second order in the prognostic variables.

In each model layer l, the horizontally averaged kinetic energy per unit mass can be written as

$$(4\pi)^{-1} \int d\sigma \, \frac{1}{2}\mathbf{v}_l^2 = \frac{a_e^2}{8\,\pi} \sum_{nm} \frac{1}{n(n+1)} \left(\xi_{l\,m\,n}^2 + D_{l\,m\,n}^2 \right).$$

Accordingly, the kinetic energy per unit mass for total wave number n and for a particular model layer l yields

$$K(n) := \frac{a_e^2}{8\,\pi\,n(n+1)} \sum_{m=-n}^{n} \left(\xi_{l\,m\,n}^2 + D_{l\,m\,n}^2 \right). \tag{A60}$$

A.5 Time integration

For each spectral mode $n\,m$ the final model equations can formally be written as

$$\dot{\mathbf{y}}_{n\,m} = \mathbf{T}_{n\,m} \tag{A61}$$

$$\mathbf{y}_{n\,m}^T := \left(\xi_{1\,n\,m}, \ldots, \xi_{lev\,n\,m},\, D_{1\,n\,m}, \ldots, D_{lev\,n\,m},\, T_{1\,n\,m}, \ldots, T_{lev\,n\,m},\, p_{s\,n\,m} \right). \tag{A62}$$

For $n > 0$ the tendency vector $\mathbf{T}_{n\,m}$ can be expanded as

$$\mathbf{T}_{n\,m} = \mathsf{A}_n\,\mathbf{y}_{n\,m} + \mathbf{T}'_{n\,m} \tag{A63}$$

$$\text{with} \qquad \mathsf{A}_n := \begin{pmatrix} 0 & 0 & 0 \\ 0 & 0 & n(n+1)\,\mathsf{a}_1 \\ 0 & \mathsf{a}_2 & 0 \end{pmatrix}. \tag{A64}$$

Here, $\mathbf{T}'_{n\,m}$ represents all spectral tendencies owing to Coriolis force, nonlinearities, diffusion, gravity waves, and diabatic heating. The Matrix A_n describes the buoyancy oscillations of a horizontally uniform reference state, i.e. the internal gravity waves in a corresponding linearized model version without Coriolis force and without all so-called physical parameterizations. These gravity modes separate in spectral space and degenerate with respect to the zonal wave number m. $\mathsf{A_n}$ is zero up to the coupling between $(D_{1,n\,m}, \ldots, D_{lev\,n\,m})$ and $(T_{1\,n\,m}, \ldots, T_{lev\,n\,m}, p_{s\,n\,m})$. The matrixes a_1 and a_2 depend on the reference state $T_{ref}(p)$ and on the distribution of model layers only (see Simmons and Burridge, 1981, appendix). In *KMCM*, we use the reference state shown in Fig. 32a. In *ECHAM*, an isothermal reference state is employed.

Following Hoskins and Simmons (1975), time stepping is performed using the semi-implicit leapfrog scheme. This scheme must be completed by a time filter (Asselin 1972) in order to damp the computational modes. This so-called semi-implicit method gains its efficiency from 'stretching' the oscillatory terms. This is achieved by application of the implicit leapfrog scheme to the linear terms and the explicit scheme to the remainder. Dropping the wave number indices $n\,m$, introducing the time index i, and denoting the time step by Δt, we get

$$\frac{\mathbf{y}_{i+1} - \mathbf{y}_{i-1}}{2\,\Delta t} = \mathsf{A}\,\frac{\mathbf{y}_{i+1} + \mathbf{y}_{i-1}}{2} + \mathbf{T}'_i\,. \tag{A65}$$

Solving (A65) for $\mathbf{y}_{i+1}$ and introducing the time filter yields

$$\mathbf{y}_{i+1} = (\mathsf{E} - \Delta t\,\mathsf{A})^{-1}\,(\mathsf{E} + \Delta t\,\mathbf{A})\,\tilde{\mathbf{y}}_{i-1} + 2\,\Delta t\,(\mathsf{E} - \Delta t\,\mathsf{A})^{-1}\,\mathbf{T}'_i \tag{A66}$$

$$\tilde{\mathbf{y}}_i = \mathbf{y}_i + \delta\,(\,\tilde{\mathbf{y}}_{i-1} - 2\,\mathbf{y}_i + \mathbf{y}_{i+1}\,)\,. \tag{A67}$$

Here, the unit matrix is abbreviated as E , and δ is a filter parameter which is usually set equal to 0.1. The leapfrog scheme requires two foregoing time steps to perform the next. In *KMCM*, the first time step is computed from the initial condition $\tilde{\mathbf{y}}_0$ by performing one Eulerian time step followed by five semi-implicit time steps using $\Delta t/5$.

Application of the explicit leapfrog scheme to diffusion tendencies can cause numerical instabilities that require short time steps in order to be controlled by the time filter. On the other hand, numerical stability of diffusion tendencies would be guaranteed by using an implicit leapfrog time step for these terms. *KMCM* compromises between numerical efficiency and a comprehensible source code by applying an Eulerian step for time integration of all tendencies owing to diffusion, dissipation, and the IGW parameterization. In other words, in (A66), $\mathbf{T}'_i$ contains diffusion, dissipation, and IGW tendencies from time $i-1$. The particular time steps used in the T42/L24 and T29/L60 model versions are 15 and 7.30 minutes. Alternatively to semi-implicit time stepping, the model can be integrated by explicit standard schemes like the Runge-Kutta or the Bulirsch-Stoer method for instance. However, these schemes require shorter time steps and are less efficient.

Appendix B

Derivation of friction and dissipation forms

This appendix provides some mathematical guidance to derive the friction and dissipation forms (3.7)-(3.10). Using the notation introduced in chapters 2 and 3, it is readily shown that

$$\begin{aligned} \nabla \circ \mathbf{v} &= (\,\mathbf{e}_x\,\partial_x + \mathbf{e}_y\,\partial_y\,) \circ (\,u\,\mathbf{e}_x + v\,\mathbf{e}_y\,) \\ &= \mathbf{e}_x \circ \mathbf{e}_x\,(\,D - \partial_y v\,) + \mathbf{e}_x \circ \mathbf{e}_y\,(\,\xi + \partial_y u\,) - \mathbf{e}_x \circ \mathbf{e}_z\; u/r \\ &\quad + \mathbf{e}_y \circ \mathbf{e}_x\,\partial_y u + \mathbf{e}_y \circ \mathbf{e}_y\,\partial_y v - \mathbf{e}_y \circ \mathbf{e}_z\,v/r\,. \end{aligned} \tag{B1}$$

The transposed tensor yields

$$\begin{aligned} \{\,\nabla \circ \mathbf{v}\,\}^T &= \mathbf{e}_x \circ \mathbf{e}_x\,(D - \partial_y v) + \mathbf{e}_x \circ \mathbf{e}_y\,\partial_y u \\ &\quad + \mathbf{e}_y \circ \mathbf{e}_x\,(\xi + \partial_y u) + \mathbf{e}_y \circ \mathbf{e}_y\,\partial_y v \\ &\quad - \mathbf{e}_z \circ \mathbf{e}_x\,u/r - \mathbf{e}_z \circ \mathbf{e}_y\,v/r\,. \end{aligned} \tag{B2}$$

Combination of (B1) and (B2) gives rise to the components of the symmetric tensor (3.3). The divergence of (B1) is:

$$\nabla_3\,\{\,\nabla \circ \mathbf{v}\,\} = (\nabla + \mathbf{e}_z\,\partial_z)\,\{\,\nabla \circ \mathbf{v}\,\} = (\nabla \cdot \nabla + \mathbf{e}_z \partial_z \cdot \nabla)\,\mathbf{v} = \nabla^2\,\mathbf{v}\,. \tag{B3}$$

We write the divergence of (B2) as

$$\begin{aligned} \nabla_3\,\{\,\nabla \circ \mathbf{v}\,\}^T &= (\mathbf{e}_x\partial_x + \mathbf{e}_y\partial_y + \mathbf{e}_z\partial_z)\;\{\;\mathbf{e}_x \circ \mathbf{e}_x\,(D - \partial_y v) + \mathbf{e}_x \circ \mathbf{e}_y\,\partial_y u \\ &\quad + \mathbf{e}_y \circ \mathbf{e}_x\,(\xi + \partial_y u) + \mathbf{e}_y \circ \mathbf{e}_y\,\partial_y v - \mathbf{e}_z \circ \mathbf{e}_x\,u/r - \mathbf{e}_z \circ \mathbf{e}_y\,v/r\,\}\,. \end{aligned}$$

To further evaluate this expression, we have to take the derivatives (3.2) as well as $\partial_x\partial_y = \partial_y\partial_x - \frac{\mathrm{tg}\,\phi}{r}\partial_x$ into account. After several steps we arrive at

$$\nabla_3\,\{\,\nabla \circ \mathbf{v}\,\}^T = \nabla\,D - \frac{1}{r}\,(\,\partial_z\mathbf{v} + D\,\mathbf{e}_z\,)\,. \tag{B4}$$

Adding (B3) and (B4) gives

$$\nabla_3 \left(\{\nabla \circ \mathbf{v}\} + \{\nabla \circ \mathbf{v}\}^T \right) = \nabla^2 \mathbf{v} + \nabla D - \frac{1}{r} \left(\partial_z \mathbf{v} + D \, \mathbf{e}_z \right) \tag{B5}$$

It is easyly shown that

$$\nabla_3 \left\{ \mathbf{e}_z / r \circ \mathbf{v} \; + \; \mathbf{v} \circ \mathbf{e}_z / r \right\} \; = \; 2 \, \frac{\mathbf{v}}{r^2} \; + \; \frac{D}{r} \, \mathbf{e}_z \; + \; \frac{\partial_z \mathbf{v}}{r} \, . \tag{B6}$$

Then, combination of (B3)-(B6) yields

$$\nabla_3 \left\{ (\nabla + \mathbf{e}_z / r) \circ \mathbf{v} \right\} \; + \; \nabla_3 \left\{ (\nabla + \mathbf{e}_z / r) \circ \mathbf{v} \right\}^T = \; \nabla^2 \, \mathbf{v} + \nabla \, D + 2 \, \mathbf{v} / r^2 \, . \tag{B7}$$

Since the tensor (3.5) contains no $\mathbf{e}_z \circ \mathbf{e}_x$ or $\mathbf{e}_z \circ \mathbf{e}_y$ components, the friction force (3.7) follows immediately from (B7) with regard to the scale approximations (2.44),(2.55).

The dissipation associated with vertical diffusion is

$$\epsilon_z = \frac{1}{\rho} \left(\Sigma_z \, \nabla_3 \right) \cdot \mathbf{v} = \; K_z \left\{ \mathbf{e}_z \left(\partial_z \mathbf{v} \cdot \nabla \right) \; + \; \partial_z \mathbf{v} \, \partial_z \right\} \cdot \mathbf{v} \tag{B8}$$

which yields (3.10) according to (2.41),(2.42). The dissipation associated with the horizontal diffusion tensor (3.5) is

$$\begin{aligned} \epsilon_h \;\; &= \;\; \frac{1}{\rho} \left(\Sigma_h \, \nabla_3 \right) \cdot \mathbf{v} \\ &= \;\; K_h \left\{ \; 2 \left(D - \partial_y v \right) \mathbf{e}_x \, \partial_x \; + \; \left(\xi + 2 \, \partial_y u \right) \mathbf{e}_x \, \partial_y \right. \\ &\qquad \left. + \left(\xi + 2 \, \partial_y u \right) \mathbf{e}_y \, \partial_x \; + \; 2 \, \partial_y v \, \mathbf{e}_y \, \partial_y \; \right\} \cdot \mathbf{v} \, . \end{aligned} \tag{B9}$$

Using the derivatives (3.2), the final formula (3.9) is obtained after a few steps.

Partial list of symbols

a_e	earth radius (= 6378.2 km)
AE	available potential energy associated with deviations from the zonal-mean flow
AZ	available potential energy of the zonal-mean flow
c	horizontal phase speed of an internal gravity wave (IGW)
c_p	specific heat capacity at constant pressure (= 1004 $\mathrm{m^2 s^{-2} K^{-1}}$)
C	surface coefficient
D	horizontal divergence
$\mathcal{D}$	vertical diffusion coefficient corresponding to an individual IGW
e	internal energy per unit mass
$\mathbf{e}_x$, $\mathbf{e}_y$, $\mathbf{e}_z$	unit vectors in zonal, meridional, and vertical direction
E	energy deposition by gravity wave-mean flow interaction
f	Coriolis parameter
$\mathbf{F}$	vertical flux of horizontal momentum generated by IGWs
F_p	vertical flux of pressure generated by IGWs
F_s	vertical flux of entropy generated by IGWs
g	gravity acceleration (= 9.81 $\mathrm{ms^{-2}}$)
h	enthalpy per unit mass
H	scale height
$\mathbf{H}$	horizontal momentum diffusion
I	idem factor
$\mathbf{J}$	sensible heat flux owing to turbulent motions
k	horizontal wave number of an individual IGW
k_e	kinetic energy per unit mass of the subscale motion
KE	kinetic energy associated with deviations from the zonal-mean flow
KZ	kinetic energy of the zonal-mean flow
$K(n)$	horizontally averaged kinetic energy per unit mass for total wavenumber n
K_h, K_z	horizontal and vertical diffusion coefficients

$K_{z\,igw}$	vertical diffusion coefficient generated by a family of IGWs
L_r	relative angular momentum of the atmosphere
L_0	Ω-angular momentum of the atmosphere
N	Brunt-Väisälä frequency
p	pressure
p_{00}	sea level reference pressure (= 1013 mb)
p_{ref}	global mean surface pressure (= model constant for given orography)
P	molecular stress tensor
$\mathbf{q}$	molecular heat flux
Q	diabatic heating due to radiation and condensation
Q_c	prescribed cumulus heating
Q_m	heating function used for self-induced condensational heating
$u,\ v,\ w$	zonal, meridional, and vertical velocity components
$r = a_e + z$	distance from the center of the earth
R	gas constant (= 287.04 $\mathrm{m^2 s^{-2} K^{-1}}$)
s	entropy per unit mass
T	temperature
T_s	surface temperature
T_E	equilibrium temperature
T_{ref}	reference temperature
TP	total potential energy of the atmosphere
TK	total kinetic energy of the atmosphere
$\tilde{u}$	parameter that specifies the initial amplitude of an individual IGW
$\mathbf{v}_3$	three-dimensional velocity field
$\mathbf{v}$	horizontal velocity field
W_{res}	residual work associated with gravity wave-mean flow interaction
z	height above sea level
z_0	level of gravity wave initialization
$z_b,\ z_c$	breaking level and critical level of an individual IGW
z_s	topographic height above sea level
$\mathbf{Z}$	vertical momentum diffusion
ϵ	frictional heating (dissipation)
ϵ_{igw}	frictional heating owing to IGWs
$\epsilon_m = \epsilon_h + \epsilon_z$	frictional heating owing to horizontal and vertical momentum diffusion of the planetary-scale flow
η	hybrid coordinate

∂_t	partial time derivative
∂_x, ∂_y, ∂_z	partial derivatives in zonal, meridional, and vertical direction
λ, ϕ	longitude and latitude
$\lambda_c = \lambda_r + i\,\lambda_i$	complex vertical wavenumber of an individual IGW
μ_h	horizontal diffusion of temperature
μ_z	vertical diffusion of potential temperature
∇_3	three-dimensional gradient operator
∇	horizontal gradient operator
ω	pressure velocity
$\mathbf{\Omega}$	angular velocity vector of the earth
$\Phi = g\,z$	geopotential
$\Phi_s = g\,z_s$	orography
ρ	density
ρ_{00}	sea level reference density
$\mathbf{\Sigma}$	Reynolds stress tensor
$\mathbf{\Sigma}_h$	stress tensor associated with horizontal momentum diffusion
$\mathbf{\Sigma}_z$	stress tensor associated with vertical momentum diffusion
τ	relaxation time
Θ	potential temperature
Θ_s	surface potential temperature
ξ	relative horizontal vorticity

References

Akmaev, R. A., 2001. Simulation of large-scale dynamics in the mesosphere and lower thermosphere with the Doppler-spread parameterization of gravity waves. 1. Implementation and zonal mean climatologies. *J. Geophys. Res.*, **106**, 1193-1204.

Alekseev, V. A., E. M. Volodin, and V. Ya. Galin, 1996. On the role of dissipation in the formation of atmospheric circulation. *Izvestiya, Atmospheric and Oceanic Physics*, **32**, 708-714.

Andreasen, Ø, C. E. Wasberg, D. C. Fritts, and J. R. Isler, 1994. Gravity wave breaking in two and three dimensions: 1. Model description and comparison of two-dimensional evolutions. *J. Geophys. Res.*, **99**, 8095-8108.

Andrews, D. G. and M. E. McIntyre, 1976. Planetary waves in horizontal and vertical shear: the generalized Eliassen-Palm relation and the mean zonal acceleration. *J. Atmos. Sci.*, **33**, 2031-2048.

Andrews, D. G., J. R. Holton and C. B. Leovy, 1987. Middle atmosphere dynamics. *Academic Press, San Diego*, 489 pp.

Asselin, R., 1972. Frequency filter for time integrations. *Mon. Wea. Rev.*, **100**, 487-490.

Barnes, J. R. and R. E. Young, 1992. Nonlinear baroclinic instability on the sphere: Multiple life cycles with surface drag and thermal damping. *J. Atmos. Sci.*, **49**, 861-878.

Becker, E., 2001. Symmetric stress tensor formulation of horizontal momentum diffusion in global models of atmospheric circulation. *J. Atmos. Sci.*, **58**, 269-282.

Becker, E., 2003. Frictional heating in global climate models. *Mon. Wea. Rev.*, **131**, 508-520.

Becker, E., G. Schmitz, and R. Geprägs, 1997. The feedback of midlatitude waves onto the Hadley cell in a simple general circulation model. *Tellus*, **49A**, 182-199.

Becker, E. and G. Schmitz, 1999. The role of orographically and thermally forced stationary waves in the causation of the residual circulation. *Tellus*, **51A**, 903-913.

Becker, E. and G. Schmitz, 2001. Interaction between extratropical stationary waves and the zonal mean circulation. *J. Atmos. Sci.*, **58**, 462-480.

Becker, E. and G. Schmitz, 2002. Energy deposition and turbulent dissipation owing to gravity waves in the mesosphere. *J. Atmos. Sci.*, **59**, 54-68.

Becker, E. and G. Schmitz, 2003. Climatological effects of orography and land-sea heating contrasts on the gravity-wave driven circulation of the mesosphere. *J. Atmos. Sci.*, **60**, 103-118.

Berger, U. and U. von Zahn, 1999. The two-level structure of the mesopause: A model study. *J. Geophys. Res.*, **104**, 22083-22093.

Bister, M. and K. A. Emanuel, 1998. Dissipative heating and hurricane intensity. *Meteorol. Atmos. Phys.*, **65**, 233-240.

Chandra, S., 1980. Energetics and thermal structure of the middle atmosphere. *Planet. Space Sci.*, **28**, 585-593.

Chao, W. C. and M. R. Schoeberl, 1984. On the linear approximation of gravity wave saturation in the mesosphere. *J. Atmos. Sci.*, **41**, 1893-1898.

Dowdy, A., R. A. Vincent, K. Igarashi, Y. Murayama, and D. J. Murphy. A comparison of mean winds and gravity wave activity in the northern and southern polar MLT. *Geophys. Res. Lett.*, **28**, No. 8, 1475-1478.

DKRZ (Deutsches Klimarechenzentrum), 1992. The ECHAM3 atmospheric general circulation model. *Technical Report No.* **6**, DKRZ, Hamburg.

Dunkerton, T. J., 1991. Nonlinear propagation of zonal winds in an atmosphere with Newtonian cooling and equatorial wavedriving. *J. Atmos. Sci.*, **48**, 236-263.

Fiedler, B. H., 2000. Dissipative heating in climate models. *Q. J. R. Met. Soc.*, **126**, 925-939.

Fritts, D. C. and T. E. VanZandt, 1993. Spectral estimates of gravity wave energy and momentum fluxes. Part I: energy dissipation, acceleration, and constraints. *J. Atmos. Sci.*, **50**, 3685-3694.

Fritts, D. C. and Z. Luo, 1995. Dynamical and radiative forcing of the summer mesopause circulation and thermal structure. 1. Mean solstice conditions. *J. Geophys. Res.*, **100**, 3119-3128.

Fritts, D. C. and J. A. Werne, 2000. Turbulence dynamics and mixing due to gravity waves in the lower and middle atmosphere. *Atmospheric science across the stratopause, AGU Monograph*, **123**, 143-159.

Garcia, R. R. and S. Solomon, 1985. The effect of breaking gravity waves on the dynamics and chemical composition of the mesosphere and lower thermosphere. *J. Geophys. Res.*, **90**, 3850-3868.

Gille, J. C. and L. V. Lyjak, 1986. Radiative heating and cooling rates in the middle atmosphere. *J. Atmos. Sci.*, **43**, 2215-2229.

Haltiner, G. J. and R. T. Williams, 1980. Numerical prediction and dynamic meteorology. *John Wiley & Sons*, 477 pp.

Hamilton, K., 1996. Comprehensive meteorological modelling of the middle atmosphere: a tutorial review. *J. Atmos. Terr. Phys.*, **58**, 1591-1627.

Hines, C. O., 1997. Doppler-spread parameterization of gravity-wave momentum deposition in the middle atmosphere. Part 1: Basic formulation. *J. Atmos. Sol.-Terr. Phys.*, **59**, 371-386.

Hines, C. O., 1999. Correction to "Doppler-spread parameterization of gravity-wave momentum deposition in the middle atmosphere. Part 1: Basic formulation." *J. Atmos. Sol.-Terr. Phys.* **61**, 941.

Hines, C. O. and C. A. Reddy, 1967. On the propagation of atmospheric gravity waves through regions of wind shear. *J. Geophys. Res.*, **72**, 1015-1034.

Hocking, W. K., 1999. The dynamical parameters of turbulence theory as they apply to middle atmosphere studies. *Earth Planets Space*, **51**, 525-541.

Hodges, R. R., Jr., 1967. Generation of turbulence in the upper atmosphere by internal gravity waves. *J. Geophys. Res.* **72**, 3455-3458.

Holton, J. R., 1982. The role of gravity wave induced drag and diffusion in the momentum budget of the mesosphere. *J. Atmos. Sci.*, **39**, 791-799.

Holton, J. R., 1983. The influence of gravity wave breaking on the general circulation of the middle atmosphere. *J. Atmos. Sci.*, **40**, 2497-2507.

Holton, J. R., 1992. An introduction to dynamic meteorology. *Academic Press, San Diego*, 511 pp.

Holton, J. R. and X. Zhu, 1984. A further study of gravity wave induced drag and diffusion in the mesosphere. *J. Atmos. Sci.*, **41**, 2653-2662.

Holton, J. R., P. H. Haynes, M. E. McIntyre, A. R. Douglass, R. B. Rood, and L. Pfister, 1995. Stratosphere-troposphere exchange. *Rev. Geophys.*, **33**, 403-439.

Holtslag, A. A. M. and B. A. Boville, 1993. Local versus nonlocal boundary-layer diffusion in a global climate model. *J. Climate*, **6**, 1825-1842.

Hoskins, B. J. and A. J. Simmons, 1975: A multi-layer spectral model and the semi-implicit method. *Q. J. Roy. Met. Soc.*, **101**, 637-655.

Hou, A. Y., 1993. The influence of tropical heating displacements on the extratropical climate. *J. Atmos. Sci.*, **50**, 3553-3570.

Huaman, M. M. and B. B. Balsley, 1999. Differences in near-mesopause summer winds, temperature, and water vapor at northern and southern latitudes as possible causal factors for inter-hemispheric PMSE differences. *Geophys. Res. Lett.*, **26**, 1529-1532.

IPCC (Intergovernmental Panel on Climate Change), 1994. Climate change 1994: Radiative forcing of climate change and an evaluation of the IPCC IS92 emission scenarios. Edited by J. T. Houghton, L. G. Meira Filho, J. Bruce, Hoesung Lee, B. A. Callander, E. Haites, N. Harris, and K. Maskell. *Cambridge University Press*, 339 pp.

James, I. N., 1994. Introduction to circulating atmospheres. *Cambridge University Press*, 422 pp.

Kiehl, J. T., J. J. Hack, G. B. Bonan, B. A. Boville, B. P. Briegleb, D. L. Williamson, and P. J. Rasch, 1996. Description of the NCAR community climate model (CCM3). *NCAR Tech. Note* NCAR/TN-420+STR. NCAR, Boulder CO 80307, USA.

Körnich, H., G. Schmitz, and E. Becker, 2003. Dependence of the annular mode in the troposphere and stratosphere on orography and land-sea heating contrasts. *Geophys. Res. Lett.*, **30(5)**, 1265, doi:10.1029/2002GL016327.

Koshyk, J. N. and K. Hamilton, 2001. The horizontal kinetic energy spectrum and spectral budget simulated by a high-resolution troposphere-stratosphere-mesosphere GCM. *J. Atmos. Sci.*, **58**, 329-348.

Laursen, L. and E. Eliasen, 1989. On the effects of the damping mechanisms in an atmospheric general circulation model. *Tellus*, **41A**, 385-400.

Lindzen, R. S., 1973. Wave-mean flow interaction in the upper atmosphere. *Bound. Lay. Met.*, **4**, 327-343.

Lindzen, R. S., 1981. Turbulence and stress owing to gravity wave and tidal breakdown. *J. Geophys. Res.*, **86**, 9707-9714.

Lindzen, R. S., 1984. Gravity waves in the mesosphere. *Dynamics of the middle atmosphere*, edited by J. R. Holton and T. Matsuno. *TERRAPUB, Tokyo*, 3-18.

Lindzen, R. S. 1990. Dynamics in atmospheric physics. *Cambridge University Press*, 310 pp.

Lorenz, E. N. 1955. Available potential energy and the maintenance of the general circulation. *Tellus*, **7**, 157-167.

Lorenz, E. N., 1967. The nature and theory of the general circulation of the atmosphere. *WMO Monograph*, **218**, 161 pp.

Lübken, F.-J., 1992. On the extraction of turbulent parameters from atmospheric density fluctuations. *J. Geophys. Res.*, **97**, 20385-20395.

Lübken, F.-J., 1997a. Seasonal variation of turbulent energy dissipation rates at high latitudes as determined by in situ measurements of neutral density fluctuations. *J. Geophys. Res.*, **102**, 13441-13456.

Lübken, F.-J., 1997b. Experimental constraints on gravity wave parameterization from in situ measurements of temperature and turbulence. *Gravity wave processes*, edited by Kevin Hamilton. *Springer Berlin-Heidelberg*, 69-84.

Lübken, F.-J., W. Hillert, G. Lehmacher, and U. von Zahn, 1993. Experiments revealing small impact of turbulence on the energy budget of the mesosphere and lower thermosphere. *J. Geophys. Res.*, **98**, 20369-20384.

Lübken, F.-J., M. J. Jarvis, and G. O. L. Jones, 1999. First in situ temperature measurements at the Antarctic summer mesopause. *Geophys. Res. Lett.*, **26**, 3581-3584.

Mak, M., 1994. Cyclogenesis in a conditionally unstable moist baroclinic atmosphere. *Tellus*, **46A**, 14-33.

Matsuno, T., 1982. A quasi one-dimensional model of the middle atmosphere circulation interacting with internal gravity waves. *J. Met. Soc. Japan*, **60**, 215-226.

McFarlane, N. A., 1987. The effect of orographically excited gravity wave drag on the general circulation of the lower stratosphere and troposphere. *J. Atmos. Sci.*, **44**, 1755-1800.

McIntyre, M. E., 1989. On dynamics and transport near the polar mesopause in summer. *J. Geophys. Res.*, **94**, 14617-14628.

Mitchell, J. F. B., 1991. The equilibrium response to doubling atmospheric CO_2. *Greenhouse-gas-induced climate change: A critical appraisal of simulations and observations*, edited by M. E. Schlesinger. *Elsevier, Amsterdam*, 49-61.

Nastrom, G. D. and K. S. Gage, 1985. A climatology of atmospheric wavenumber spectra of wind and temperature observed by commercial aircraft. *J. Atmos. Sci.*, **42**, 950-960.

Oort, A. H., 1964. On estimates of the atmospheric energy cycle. *Mon. Wea. Rev.*, **92**, 483-493.

Panchev, S., 1971. Random functions and turbulence. *International Series of Monographs in Natural Philosophy*, **32**. *Pergamon Press*, 444 pp.

Pauluis, O. and I. M. Held, 2002. Entropy budget of an atmosphere in radiative-convective equilibrium. Part I: Maximum work and frictional dissipation. *J. Atmos. Sci.*, **59**, 125-139.

Pedlosky, J., 1987. Geophysical Fluid Dynamics. *Springer-Verlag, New York*. 710 pp.

Phillips, N. A., 1966. The equations of motion for a shallow rotating atmosphere and the "traditional approximation". *J. Atmos. Sci.*, **23**, 626-628.

Phillips, N. A. 1973. Principles of large scale numerical weather prediction. *Dynamic meteorology*, edited by P. Morel. *Reidel Publishing Company*, 1-96.

Pichler, H., 1986. Dynamik der Atmosphäre. *B.I.-Wissenschaftsverlag, Zürich*, 459 pp.

Prandtl, L., K. Oswatitsch, and K. Wieghardt, 1990. Führer durch die Strömungslehre. *Vieweg Verlag.* 648 pp.

Randel, W. J., 1992. Global atmospheric circulation statistics, 1000-1 mb. *NCAR Technical Note*, NCAR/TN-366+STR, 256 pp.

Rennó, N. O. and A. P. Ingersoll, 1996. Natural convection as a heat engine: a theory for CAPE. *J. Atmos. Sci.*, **53**, 572-585.

Roeckner, E. and Coauthors, 1992. Simulation of the present-day climate with the ECHAM model: Impact of model physics and resolution. *Report No.* **93**, *Max-Planck-Institut für Meteorologie*, Hamburg.

Roeckner, E. and Coauthors, 1996. The atmospheric general circulation model ECHAM-4: Model description and simulation of present-day climate. *Report No.* **218**, *Max-Planck-Institut für Meteorologie*, Hamburg.

Rosenlof, K. H. and J. R. Holton, 1993. Estimates of the stratospheric residual circulation using the downward control principle. *J. Geophys. Res.*, **98**, 10465-10479.

Salmon, R., 1998. Geophysical fluid dynamics. *Oxford University Press*, 378 pp.

Sausen, R., R. Voss, and M. Ponater, 1993. Orographic forcing in ECHAM. *Beitr. Phys. Atmosph.*, **66**, 239-252.

Serrin, J., 1959. Mathematical principles of classical fluid mechanics. *Encyclopedia of physics*, edited by S. Flügge and C. Truesdell. *Springer-Verlag*, 125-263.

Shine, K. P., 1987. The middle atmosphere in the absence of dynamical heat fluxes. *Q. J. R. Met. Soc.*, **113**, 603-633.

Simmons, A. J. and B. J. Hoskins, 1978: The life cycles of some nonlinear baroclinic waves. *J. Atmos. Sci.*, **35**, 414-432.

Simmons, A. J. and D. M. Burridge, 1981. An energy and angular-momentum conserving vertical finite-difference scheme and hybrid vertical coordinates. *Mon. Wea. Rev.*, **109**, 758-766.

Simmons, A. J. and J. Chen, 1991. The calculation of geopotential and the pressure gradient in the ECMWF atmospheric model: Influence on the simulation of the polar atmosphere and on temperature analyses. *Q. J. R. Met. Soc*, **117**, 29-58.

Smagorinsky, J., 1963. General circulation experiments with the primitive equations. 1. The basic experiment. *Mon. Wea. Rev.* **91**, 99-164.

Smagorinsky, J. 1993. Some historical remarks on the use of nonlinear viscosities. *Large eddy simulation of complex engineering and geophysical flows*, edited by B. Galperin and St. A. Orszag. *Cambridge University Press*, 3-36.

Szabó, I., 1977. Geschichte der mechanischen Prinzipien. *Birkhäuser Verlag*, 571 pp.

Thomas, G. E., 1996. Global change in the mesosphere-lower thermosphere region: has it already arrived? *J. Atmos. Terr. Phys.*, **58**, 1629-1656.

Vallis, G. K., G. J. Shutts, and M. E. B. Gray, 1997. Balanced mesoscale motion and stratified turbulence forced by convection. *Q. J. R. Met. Soc.*,**123**, 1621-1652.

van Mieghem, J., 1973. Atmospheric Energetics. *Clarendon Press, Oxford*, 306 pp.

Volodin, E. M. and G. Schmitz, 2001. A troposphere-stratosphere-mesosphere general circulation model with parameterization of gravity waves: climatology and sensitivity studies. *Tellus*, **53A**, 300-316.

Weinstock, J., 1988. Superadiabatic excess and gravity wave saturation. *J. Atmos. Sci.*, **45**, 3519-3520.

Werne, J. and D. C. Fritts, 1999. Stratified shear turbulence: Evolution and statistics. *Geophys. Res. Lett.*, **26**, 439-442.

Yulaeva, E., J. R. Holton, and J. M. Wallace, 1994. On the cause of the annual cycle in tropical lower-stratospheric temperatures. *J. Atmos. Sci.*, **51**, 169-174.